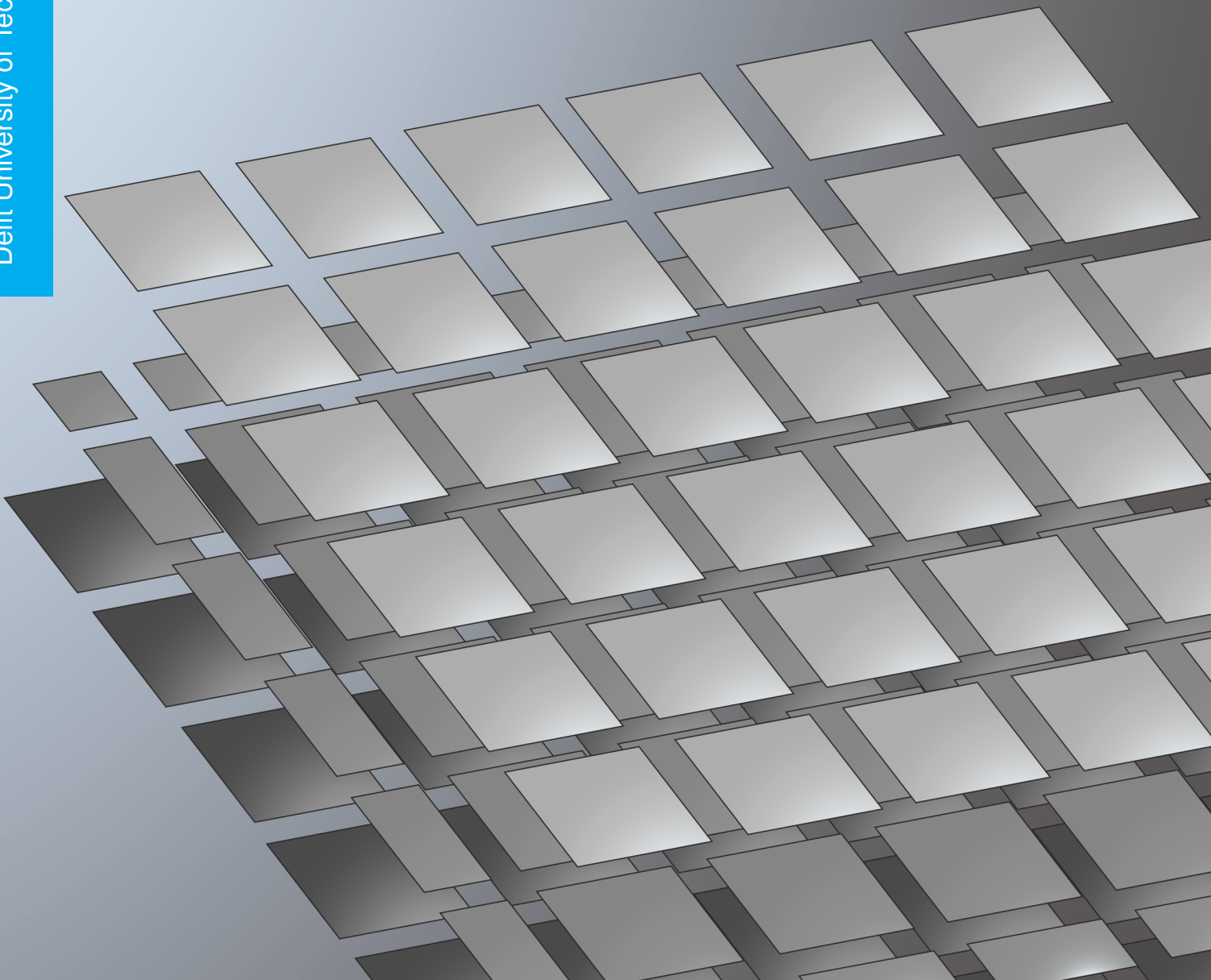


Master thesis - Electrical Engineering

Analytical Study of Artificial Dielectrics Composed of Non-Aligned Layers

Cantika Felita 4489985

Delft University of Technology



Analytical Study of Artificial Dielectrics Composed of Non-Aligned Layers (August 21, 2017)

Copyright © 2017 Cantika Felita

All rights reserved.



Preface

This thesis is submitted in partial fulfillment of the requirements for the degree of Master of Science in Electrical Engineering at Delft University of Technology.

Cantika Felita
Delft, August 2017

Acknowledgments

This thesis would not have been done without the support of a number of wonderful groups and individuals, my thanks and appreciation to all of them for being a part of this journey. My pursuit of an advanced degree is possible in the first place because of the financial support from LPDP (Indonesia Endowment Fund for Education), thus I am grateful for the chance and I hope I can bring more positive things in the future.

I would like to express my gratitude towards Prof. dr. Andrea Neto for the opportunity of doing my master thesis at the Terahertz Sensing group. This work is a result of a patient and extensive guidance of dr. Daniele Cavallo, to whom I owe my knowledge on this topic. Thank you for introducing me to this topic (which I have grown attached to), and for always giving valuable and significant insights that make the completion of this thesis possible. I wish the Terahertz Sensing group and its members the best for their future endeavors.

A sincere thanks also goes to my amusing friends, Ash, Andi, and Raunak, for all the things that we have done together since the introduction program; my life here will be not be as colorful without our witty jokes. I also would like to thank my dear friends Alina and Matei which have introduced me to numerous fun and amazing people like themselves. My friendship with you all, which has kept me sane during my study, is one of the most valuable thing that I have.

I would also give the Verduyssen family my deepest gratitude. Lea, thank you for opening the door of your house to me; your warm smile always make me happy. Tim, thank you for bringing home 11.000 km closer. I am grateful for your support and love; and I am excited on what the future brings us.

Finally, I would like to dedicate this achievement to my parents. Thank you for always believe in my choices. I cannot wish anything better than the trust that you have given me. Thank you for always be proud of having me as your daughter, and assure me that nobody is entitled to state otherwise.

Analytical Study of Artificial Dielectrics Composed of Non-Aligned Layers

This thesis is submitted in partial fulfillment of the requirements for the degree
of

MASTER OF SCIENCE

in

ELECTRICAL ENGINEERING

by

Cantika Felita
born in Jambi, Indonesia

The work presented in this thesis was performed at:

Tera-Hertz Sensing Group
Department of Microelectronics
Faculty of Electrical Engineering, Mathematics and Computer Science
Delft University of Technology



DELFT UNIVERSITY OF TECHNOLOGY
DEPARTMENT OF ELECTRICAL ENGINEERING

The undersigned hereby certify that they have read and recommend to the Faculty of Electrical Engineering, Mathematics and Computer Science for acceptance a thesis entitled “ **Analytical Study of Artificial Dielectrics Composed of Non-Aligned Layers** ” by **Cantika Felita** in partial fulfillment of the requirements for the degree of **Master of Science**.

Dated:

Chairman:

prof. dr. Andrea Neto

Committee Members:

dr. Daniele Cavallo

dr. ir. Rob Remis

Contents

Preface	i
Acknowledgments	vi
1 Introduction	1
1.1 Integrated Antennas for High Frequency Applications	1
1.2 Challenges and the State of Art Solution of Integrated Antennas	2
1.3 Artificial Dielectric Layers: Enabling Technology for High Frequency Application	4
1.4 Artificial Dielectrics with Non-Aligned Layers	5
1.5 Objectives of the Thesis	8
1.6 Outline of the Thesis	8
2 Analysis of a Single Layer	11
2.1 Single Layer of Periodic Lossless Square Patches	11
2.1.1 Problem Definition and Equivalence Principle for Lossless Case	11
2.1.2 Solutions and Equivalent Layer Reactance for Lossless Case	13
2.2 Single Layer of Periodic Square Patches with Finite Conductivity	17
2.2.1 Problem Definition and Equivalence Principle for Lossy Case	18
2.2.2 Solutions and the Equivalent Reactance for Lossy Case	20
3 Analysis of Shifted ADLs	25
3.1 Formulation and Approximation of Current Distribution for Shifted ADLs	25
3.1.1 Problem Definitions and Equivalence Principle for Shifted ADLs	26
3.1.2 Approximation on the Magnetic Current Distribution	28
3.2 Solution of the Integral Equation and Equivalent Circuit	30
3.2.1 Equivalent Transmission-Line Model	32
3.2.2 Convergence of the Floquet Sums	34
3.3 Problem Definition and Formulation for ADLs with Finite Conductivity	34
3.3.1 Green's Function Representation for the Problem	35
3.4 Solution and the Equivalent Reactance of ADLs with Finite Conductivity	37
4 Effective Parameters and Tolerance Study of ADL	43
4.1 Attaining Effective Permittivity and Permeability	43
4.2 Dependence of the Effective Parameters on the Geometry of the Structure	46
4.3 Refractive Index of ADLs	46
4.4 Representation of Losses in Effective Parameters	49
4.5 GUI based on Analytical Solutions for ADL Design	52

5	Conclusions and Future Work	55
5.1	Summary and Conclusions	55
5.2	Future Work	56
5.3	Publications	56
	Bibliography	59
A	Solutions of the Admittance Matrix	63
A.1	Spectral Domain Expression of the Admittances	63
A.2	Reduction of the Number of Unknowns	64
A.3	Simplified Admittance Matrix	64
B	Closed Form Solutions for Infinite and Semi-Infinite Sums	67
C	Solutions for Current in ADL with Layer Composed of Lossy Patches	69
	List of Figures	75

Chapter 1

Introduction

1.1 Integrated Antennas for High Frequency Applications

An increasing popularity of planar printed antennas is not without reason. Planar antennas offer flexibility in their design, take less space than three-dimensional antennas, are inexpensive to fabricate, and can be easily integrated [1]. Hence they are largely used in a great variety of applications, including wireless communication, radars, space-based systems, etc.

In the past, at microwave frequencies, the traditional approach of antenna engineers was to design the antennas separately from the electronics. Standardized connectors or wirebonds were then used to interface the antenna with the electronic front ends. However, when the operating frequency of these systems increases, reaching the millimeter and sub-millimeter waves, the separation of antenna and electronic circuits is no longer possible. The recent demand for compact low-cost transceivers in short-range communication and sensor applications is urging the necessity to integrate the antennas with the electronics. Automotive radars and ultrafast wireless communication are two applications with huge market potentials that require high-level of integration. Thus, the recent trend is to place the antennas as close as possible to the radio front-end, possibly on the same semiconductor chip or the same printed circuit board where the electronic components are, to facilitate the interconnection.

Radars in cars ought to have high resolution and to operate over long ranges as shown in Fig. 1.1. This allows the car sensor to detect objects of various sizes and to promptly perform the required action. The radars also have to be compact in size so they can be embedded in the car without difficulty and have low production cost. Such requirements can be achieved only by moving to higher frequency. Most of the currently developed short- and long-range automotive radars already operate in the frequency band 76-77 GHz [2].

Another area that can largely benefit from higher frequency is wireless communication [3]. Figure 1.2 shows the projection of speed that will be needed over the years, with some of the standards already existing for indoor wireless systems [4]. The required data rate increases about ten times every five years, because of the growing number of users and the larger amount of data to be transferred. It is evident that moving towards a higher frequency regime is the sole option to cope with the increasing data rate requirements of wireless links.

Despite the need for integrated antennas for high-speed wireless communication and automotive radars, integrated antennas have never showed good performance because of their intrinsic low efficiency. These antennas are limited by problems such as high surface-wave loss, narrow bandwidth, low front-to-back radiation ratio.

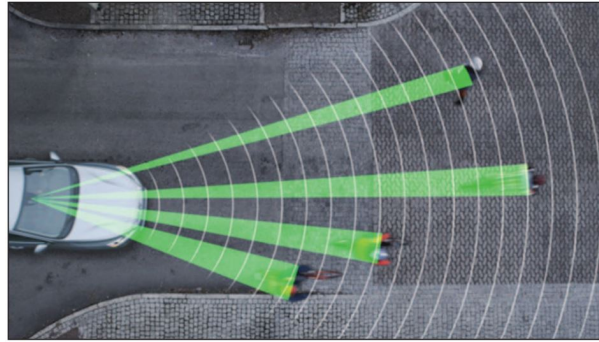


Figure 1.1: Illustration of a car equipped with long-range and high-resolution radars in action. With the help of the radars, the car is able to distinguish cyclists on its way and perform braking when it is needed [2].

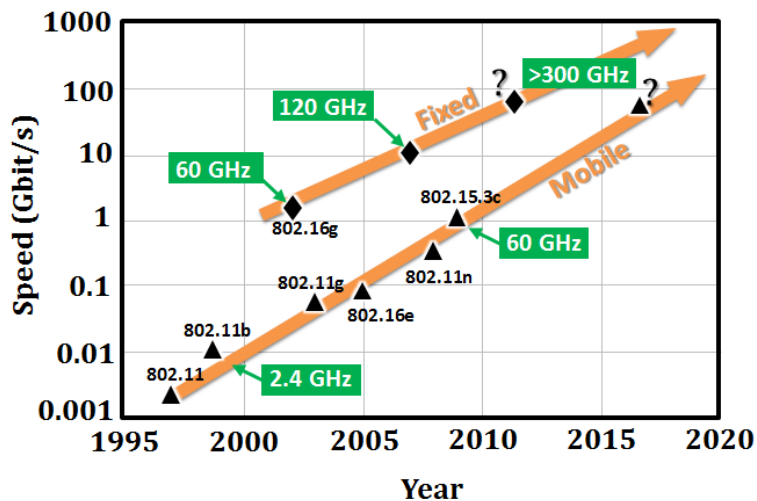


Figure 1.2: Projection of speed over year both for the fixed and mobile communications. Several points mark the standards and the corresponding operating frequency [4].

1.2 Challenges and the State of Art Solution of Integrated Antennas

High-frequency planar antennas often exhibit poor performance and low radiation efficiency. A planar antenna in free-space, for example a resonant slot antenna depicted in Fig. 1.3(a) or a dipole shown in Fig. 1.3(b), tends to have low front-to-back ratio because it radiates the same power in the upper and in the lower half spaces.

If a ground plane is introduced, as in Fig. 1.3(c), for the slot a large portion of the power is still lost into parallel plate waveguide modes between the slot plane and the backing reflector. For the dipole, the distance from the ground plane can limit the matching bandwidth. These negative effects are more prominent when the distance h between the antenna and the metal plane is very small in terms of the wavelength. This is the case for antennas integrated on chip, which are characterized by very small h parameters, as illustrated in Fig. 1.4.

The illustration shown in Fig. 1.4 presents a typical layer stack of a chip, which consists of a thin layer of silicon dioxide (SiO_2), about $10 \mu\text{m}$ thick, on which the antenna is realized (e.g., a slot antenna). A conducting metal plane separates the SiO_2 slab from a thick silicon (Si) layer. The metal plane has the

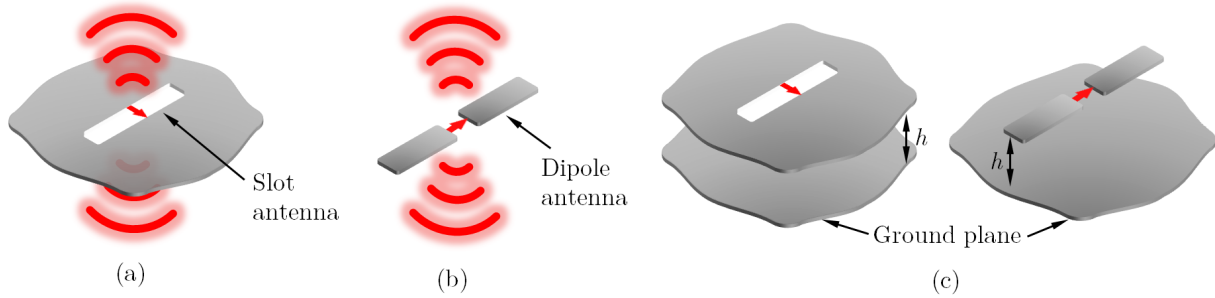


Figure 1.3: (a) A slot antenna in free space, (b) a dipole antenna in free space, and (c) the antennas in the presence of a metal ground plane.

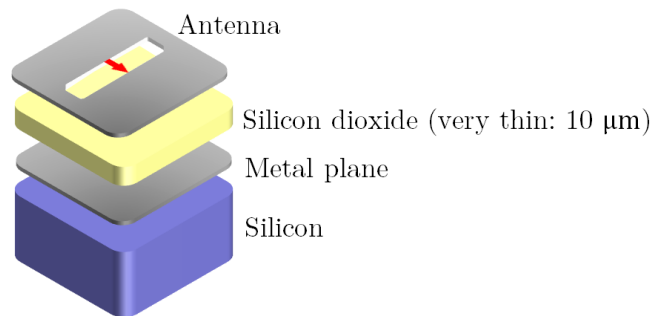


Figure 1.4: A slot antenna on chip.

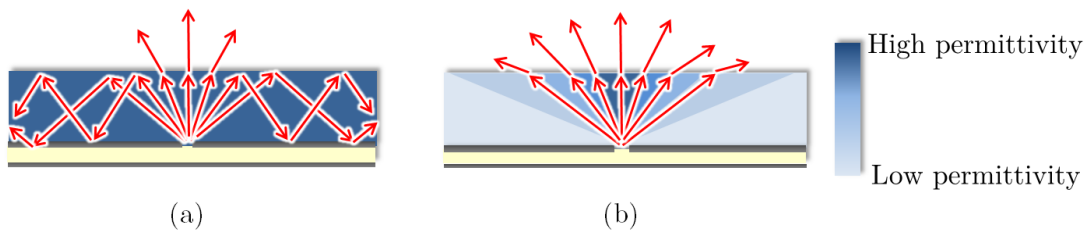


Figure 1.5: A slot antenna on chip in the presence of (a) high permittivity homogeneous superstrate and (b) ideal anisotropic superstrate.

purpose of shielding the antenna from the underlying silicon, since this latter is characterized by very high losses [5]. Because of the proximity of the antenna to the metal plane, in the case of slot radiators, most of the power remains confined within the SiO_2 layer instead of being radiated outside the chip. This translates in a poor efficiency.

The state of the art solution to these problems is to include a superstrate on the top of the planar antenna (shown in Fig. 1.5(a)), as proposed in [6]. This solution enhances the radiation efficiency and at the same time broaden the matching bandwidth. The presence of a dielectric above the antenna, with permittivity higher than the one of the material below, results in a higher front to back ratio, since most of the power is radiated in the direction of the electrically denser material.

However, the Snell's law of refraction prompts the rays that impinge at the dielectric-air interface at an angle larger than the critical angle to undergo total reflection. These modes guided within the dielectric superstrate are referred to as surface waves, and result in reduced efficiency and deteriorated far-field patterns [7].

The surface-wave problem, which is the main limit to the efficiency in practical integrated antennas, could be solved with an ideal superstrate such as the one shown in Fig. 1.5 (b). This ideal substrate has

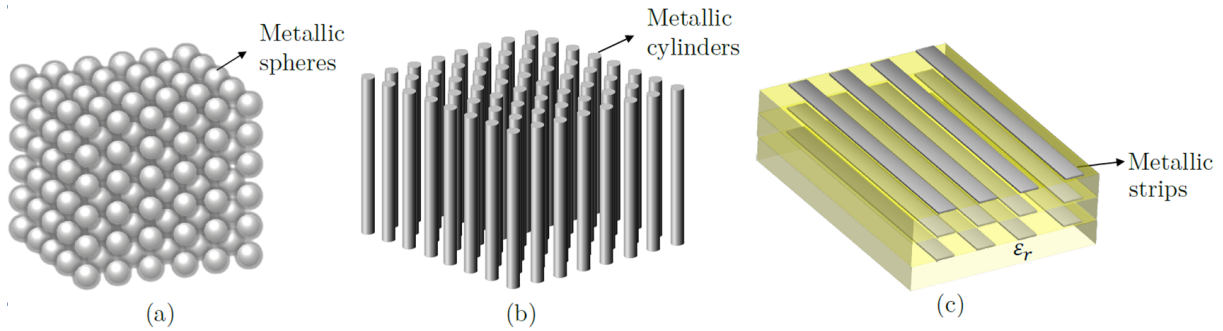


Figure 1.6: Artificial dielectrics made of (a) metallic spheres, (b) cylinders, (c) strips.

refractive index that varies with the angle of incidence, realizing an anisotropy material. Specifically, to avoid the excitation of surface waves, the refraction index should decrease as the angle of incidence increases. The high refraction index for normal incidence will yield the desired enhancement of front-to-back ratio, while the progressively decreasing permittivity for grazing angles will avoid the occurrence of critical angle, thus all power is radiated to free space.

Although such an ideal material is not existing in nature, it can be realized artificially by means of artificial dielectrics.

1.3 Artificial Dielectric Layers: Enabling Technology for High Frequency Application

Artificial dielectrics (ADs) were introduced in [8] as a light-weight alternative to real dielectric materials, for realizing microwave lenses [9]. After their introduction, ADs have been extensively studied and used for decades for radar development. An AD consists of a large-scale model of an actual dielectric, obtained by embedding conducting structures in a host material according to a regular pattern. Some physical realizations of ADs involve the insertion of metallic spheres, cylinder and strips inside a dielectric in a periodic arrangement, as shown is Fig. 1.6. In all these scenarios, the electric field scattered by the metallic inclusions, when added to the incident field, creates an effective equivalent delay [10]. At the frequencies for which the periodicity of the pattern is much smaller than the wavelength, the structure can be assigned equivalent parameters that describe an homogeneous dielectric. The effective electric parameters can be engineered by varying the size of the metal obstacles and their spatial density.

In the case of spherically symmetric obstacles, as shown in Fig. 1.6(a), the equivalent medium is isotropic, since the effect of the impressed field on the structure is independent of the polarization and the angle of incidence. However, other types of artificial dielectrics, such as the ones in Fig. 1.6(b) and (c), have anisotropic properties: both the polarization and the angle of incidence of the external electric field significantly impact on the equivalent properties of the structure.

This thesis relates to a specific type of AD, which are realized as a cascade of planar layers made of printed metal patches, as depicted in Fig. 1.7. Such structures are also referred to as artificial dielectric layers (ADLs).

The main property of ADLs, that can be exploited to enhance the efficiency of integrated antennas, is the anisotropy. The effective refractive index realized with ADLs is a function of the angle of incidence, i.e. it varies for plane-wave illumination with different incoming angles. The refraction index is also a function of the polarization, i.e. it differs for transverse electric (TE) and transverse magnetic (TM) incidence. More specifically, the typical behavior of the effective refractive index as a function of the

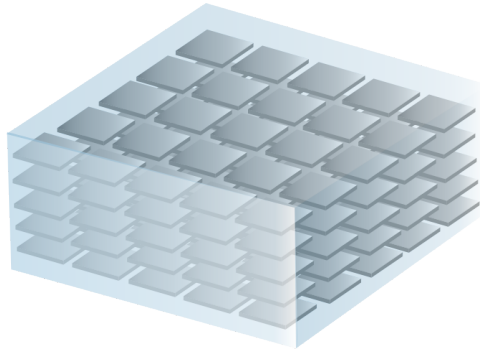


Figure 1.7: Artificial dielectric composed of cascades of metal patches layers embedded in host medium.

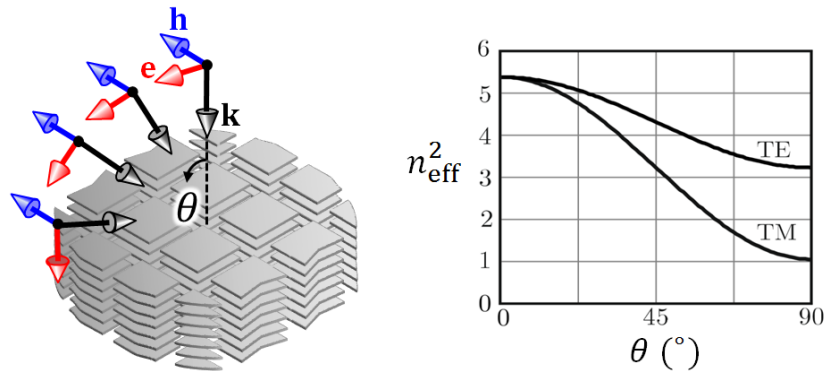


Figure 1.8: Effective refractive index of ADL as a function of the angle of incidence and the polarization.

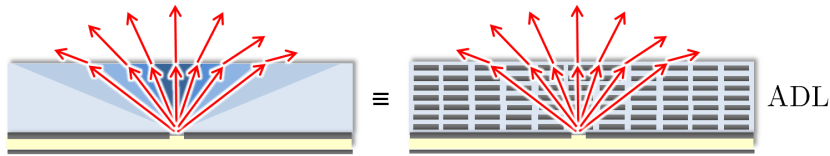


Figure 1.9: A slot antenna on chip (a) with presence of an ideal substrate on the top, (b) with ADL that mimics the ideal substrate on the top.

incidence angle is shown in Fig. 1.8. It is evident that the highest effective refractive index is obtained for normal incidence, whereas the lowest is obtained for grazing incidence. Therefore, ADLs effectively implement the ideal superstrate, as illustrated in Fig. 1.9. Due to the decreasing value as a function of the angle, surface waves are not supported, resulting in very high efficiency.

The effective refraction index can be engineered by varying the geometrical parameters of the structure, such as the inter-layer distance, the patch size and the periodicity of the patches. The benefits of using ADLs to improve the radiation performance of integrated antennas were demonstrated both in the microwave [11] and terahertz [12] frequency range. ADLs were also as a superstrate of a phased array antenna to achieve wideband wide-scanning performance in [13]. While all the ADL designs mentioned were based on aligned layers, this thesis focuses on the analysis of ADLs with non-aligned layers.

1.4 Artificial Dielectrics with Non-Aligned Layers

ADL has been studied extensively in [14] and [15]. [14] introduces a novel analytical method to describe the scattering from a single layer of rectangular patches under a generic plane-wave incidence. In [15],

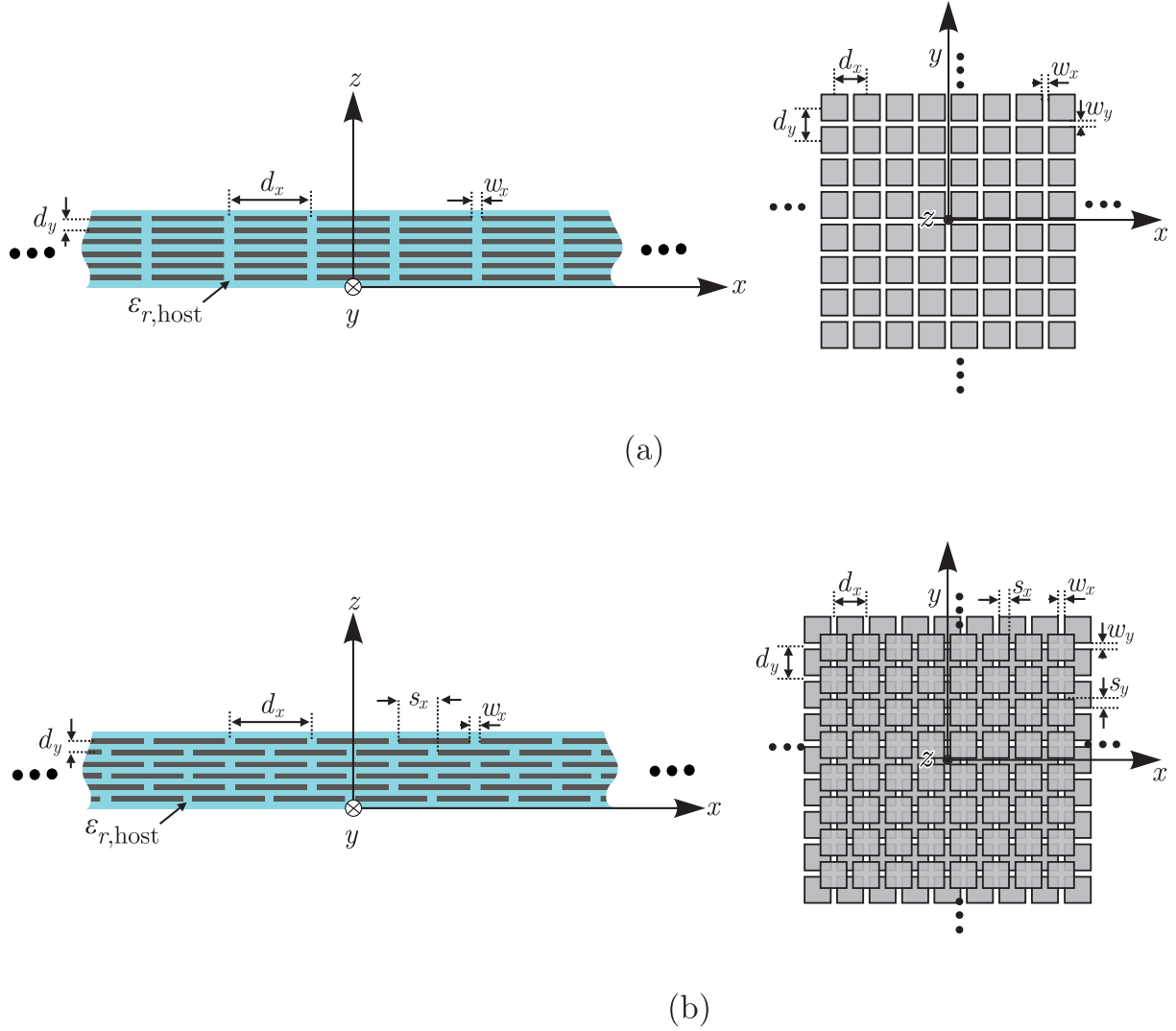


Figure 1.10: Side and top view of an ADL with (a) aligned layers (b) non-aligned (shifted) layers.

the analytical method is generalized for the characterization of ADLs of finite height, under arbitrary field illumination, leading to closed-form expressions. A rigorous equivalent circuit was given in [15], that can be used to calculate the scattering properties and the spectral Green's Function (GF) of the ADL. This analytical method is valid for aligned layers of sub-wavelength patches shown in Fig. 1.10(a). The layers on the ADL slab shown in Fig. 1.10(a) are numbered consecutively from 1 to N .

Illustrated in Fig. 1.10(b), is an ADL composed of non-aligned layers. It is achieved by shifting the odd layers with respect to the even layers (or vice versa) by s_x and s_y along x and y axis, respectively, and keeping the same inter-layer distance. The layers are shifted equally along x and y axis, thus $s_x = s_y$. The analytical solutions in [15] does not account for these shifts, therefore it is only valid when there is no shift introduced between the layers, i.e. $s_x = s_y = 0$. The purpose of this thesis is to modify the formalism in [15] to include the shifts into the analytical solution. The alternate lateral displacement between layers turns out to be a fundamental parameter to engineer the desired effective electromagnetic properties of the equivalent homogeneous material realized with the ADLs.

Formulating more general analytical solution for ADL, taking the non-alignment of the layers into consideration, is relevant due to the fact that this non-alignment can significantly increases the effective permittivity of the structure. Figure 1.11 shows, as a function of the shift, the enhancement factor defined as the ratio between the square of effective refractive indexes with and without shift. It can be noted that

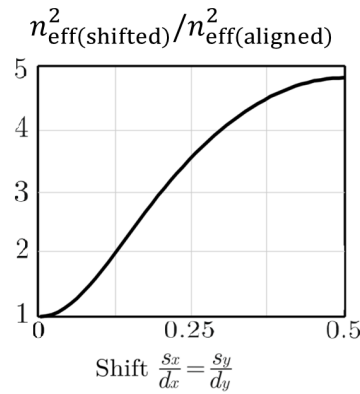


Figure 1.11: Enhancement factor, defined as the ratio between the square of effective refractive indexes with and without shift, versus shift. The ADL consists of 5 layer with $d_x = d_y = 0.0785\lambda_0$, $w_x = w_y = 0.01\lambda_0$, with λ_0 is wavelength at calculation frequency.

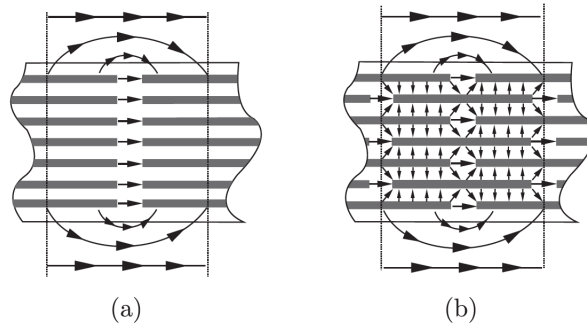


Figure 1.12: Electric field distribution for a plane wave propagating through the ADL slab for (a) aligned and (b) non-aligned layers. In the first case, the electric field is mainly concentrated in the gaps between coplanar patches. In the second case the field is also strong in the vertical gaps between contiguous layers, resulting in a higher capacitive loading.

the effective refractive index increases as a function of the normalized shift ($\frac{s_x}{d_x} = \frac{s_y}{d_y}$) and is maximum when the shifts are equal to half period of the ADL. In the specific example considered, the square of the refractive index is almost five times higher than the one obtained for aligned layers.

The main advantage of introducing the shift between layers is the improved design flexibility. In fact, to tailor the equivalent dielectric constant in ADL slabs with aligned layers, one can vary geometrical parameters such as the inter-layer distance and the gap width between patches. However, these parameters cannot be freely changed, as they are typically limited by the technological constraints of the manufacturing process. On the contrary, the shift between layers represents an additional important degree of freedom that can be used for the design. For example, the introduction of the shift can

- greatly extend the ranges of permittivity values that can be synthesized, given a specific fabrication technology;
- reduce the number of metal layers with respect to the aligned case, while realizing the same effective permittivity;
- decrease the height of the ADL slabs when used as an antenna superstrate, without penalty of the antenna performance.

The reason for the enhancement of the permittivity can be explained by observing the electric field distribution within two ADL structures, with and without shift, under plane wave illumination. When

a plane wave is impinging on the ADL structure, the electric field within the periodic unit cell can be represented with the vector field lines in Fig. 1.12. In the aligned case, the field is mainly concentrated in the gap between adjacent coplanar patches (Fig. 1.12 (a)). On the contrary, the field in the shifted case is also distributed within the areas between parallel contiguous layers (Fig. 1.12 (b)). This introduces an additional capacitance compared to the aligned setup.

Another interpretation of the increased capacitance can be described in terms of effective equivalent delay. The structure in Fig. 1.12 (b) provides higher delay, since waves are traveling for longer distances as now they have to go around the patches to find the way out of the structure. It is clear that, when fixing a specific inter-layer distance d_z , the traveling path increases with larger transverse periods (d_x, d_y).

1.5 Objectives of the Thesis

The main goal of this study is to describe the ADL with an accurate analytical model, taking the non-alignment between the layers into account. Thus, the formulas derived in this thesis are more general than the ones available [15]. An analytical and accurate model will tremendously speed up the process of designing an ADL, as we would not have to rely on the time consuming simulations with commercial solver. It will also lead to the possibility of sweeping parameters to understand the behavior of ADL and gain physical insight.

To build an equivalent circuit of ADLs, the equivalent reactance of each layer is derived in closed form, taking into account for reactive coupling between layers, the shift between odd and even layers and the finiteness of the ADL height. This equivalent transmission line model can be used to characterize the scattering (reflection and transmission) due to a plane wave impinging on the ADL.

Another important goal is to analytically characterize the losses introduced by the finite conductivity of the metal patches in ADLs. The assessment of the losses in ADL was never included before in the analytical formulas. Losses in ADLs are typically very small because of the sub-wavelength dimension of the patches, that yield very low current intensity on each patch. On the other hand, including the finite conductivity in the model allows to quantify these losses (although small) and provide an effective dissipation factor ($\tan(\delta)$) for these structure.

It is also the objective of this thesis to study more in-depth the effective parameter retrieval of ADLs. To aid the design of artificial dielectric slabs, the effective permittivity and permeability tensors are retrieved from the scattering parameters of the plane wave. Diamagnetic properties of ADLs are observed and explained with a physical interpretation. A parametric analysis of the equivalent electrical properties as a function of the geometrical parameters is also performed and can be used to provide guidelines for the design of ADLs.

All the analytical formulas have been implemented in a Matlab code equipped with a graphical user interface (GUI). This GUI is a design tool for ADLs, as it provides the effective parameters, once the geometrical parameters are defined (analysis), and it also retrieves the geometrical parameters, given a set of target effective properties (synthesis).

1.6 Outline of the Thesis

This thesis contains 5 chapters, arranged as follow:

- Chapter 1 focuses on the introduction and the background pertaining to the topic of this thesis. The objectives of the work are stated and the relevance of the thesis is motivated.
- Chapter 2 describes the steps of the formulation followed to derive the solution for the plane-wave

scattering for a single ADL layer. After setting up the integral equation, the unknown magnetic current is expanded in a set of four basis functions. The solution of the resulting system of linear equations is described and leads to a closed-form expression of the equivalent impedance of the single layer. Both the case of perfectly conducting patches and finite conductivity are considered.

- Chapter 3 reports the generalization of the procedure used for the single layer to the cascade of multiple layers, accounting for the shift. An approximation on the current is introduced to be able to achieve a closed-form for the equivalent layer impedance. The solutions for the infinite cascade, as well as for the semi-infinite one, are derived, with and without Ohmic losses.
 - Chapter 4 deals with the homogenization of ADLs, retrieving the effective parameters of the ADL. It also gives parametric analysis to highlight the dependence of the ADL properties as a function of the geometrical parameters. This chapter also includes the general description of the functions realized by the developed GUI.
 - Chapter 5 concludes with a review of the most significant results presented in this thesis and an outlook on possible future developments.
-

Chapter 2

Analysis of a Single Layer of Periodic Sub-Wavelength Patches

2.1 Single Layer of Periodic Lossless Square Patches

Artificial dielectric layers (ADLs) are composed by a cascade of multiple layers of periodic sub-wavelength patches. However, to describe the formulation used for the analysis of ADLs in a simpler way, it is convenient to consider first the case of a single layer of patches. The characterization of the scattering from a isolated layer will be useful to explain the main steps adopted for the modeling. Similar steps will be subsequently used for the case of the multiple layers, but starting from a different integral equation that takes into account the periodic sequence of layers.

Scattering from a single layer of sub-wavelength periodic square patches has been extensively reported in the literature [16–21]. In those works, several analytical methods were given that provide the equivalent reactance of the structure under plane-wave incidence. However, all the mentioned references proposed solutions that are no longer valid for multiple layer configurations, as they neglect the inter-layer coupling. An equivalent closed-form expression for the equivalent sheet reactance was recently proposed in [14]. The advantage of this formula is that it can be easily generalized to the multiple layer case, and it accounts for the higher-order coupling between adjacent layers.

In this section, a method similar to the one reported in [14] will be presented, as it will be the base for the remainder of the thesis. An expansion of the unknown magnetic current distribution was proposed in [14], using ad-hoc entire-domain basis functions. However, unlike [14], a more general expansion of the magnetic current will be used here, where four basis functions are adopted instead of three. This will allow to address the case of multiple layers in a more rigorous way. The analytical scattering parameters resulting from the formulation are also verified with simulations that are performed in CST [22].

2.1.1 Problem Definition and Equivalence Principle for Lossless Case

The formulation starts with the original problem, which is a single layer of periodic square patches along the xy plane, illustrated in Fig. 2.1. Alternatively, one can consider it as a combination of two orthogonal periodic arrays of infinitely long slots. The slot along x and y , whose widths are equal and denoted as w_x and w_y respectively, are electrically narrow ($w_x = w_y \ll \lambda$). The periodicity of the patches are indicated by d_x along x and d_y along y . The structure is illuminated by a generic plane wave. The patches are made of perfectly conducting material (PEC).

A side view of the original problem is illustrated in Fig. 2.2(a). The incident plane wave impinging on the layer consists of electric and magnetic fields, \mathbf{e}_i and \mathbf{h}_i respectively. Following the equivalence

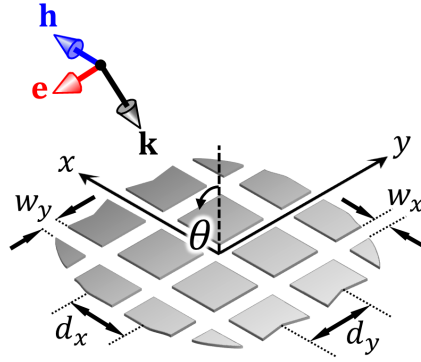


Figure 2.1: Single layer of infinitely periodic patches along xy plane with its geometrical parameters.

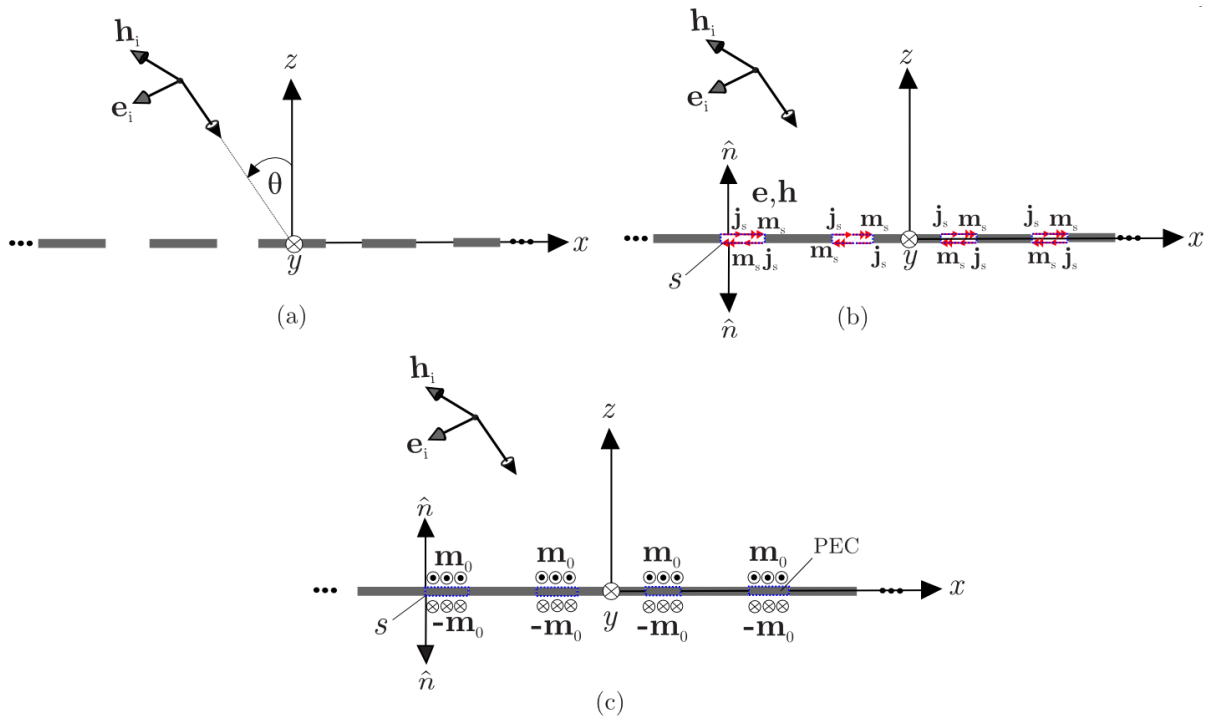


Figure 2.2: (a) Original problem which consists of a single layer of periodic square patches illuminated with generic plane wave illumination. (b) Applying equivalence theorem onto the gaps. (c) Filling the enclosed surface with perfect electrical conductor (PEC).

theorem, the gaps are enclosed with a set of infinitely thin closed surfaces S , illustrated in Fig. 2.2(b). $\hat{\mathbf{n}}$ is the outward normal unit vector to the surfaces, \mathbf{e} and \mathbf{h} denote the total fields, equal to sum of the incident and the scattered fields. Equivalent electric and magnetic current densities, \mathbf{j}_s and \mathbf{m}_s , are distributed on the surfaces and are related to the fields by $\mathbf{j}_s = \hat{\mathbf{n}} \times \mathbf{h}$ and $\mathbf{m}_s = \mathbf{e} \times \hat{\mathbf{n}}$.

Furthermore, using one of the alternative formulations of the equivalence principle [23], the volumes enclosed by S are filled with PEC, as shown in Fig. 2.2(c). With this choice, the electric current density does not contribute to the total field because it cancels out with the image current. Thus the equivalent problem only consists of an unknown magnetic current density located in correspondence of the gaps in the original problem.

The superscripts ‘+’ and ‘-’ are used to indicate the current, the field or the position above and below the layer plane. The magnetic current density \mathbf{m}_0^+ , located in the z^+ , is related to the electric field in the gaps by $\mathbf{m}_0^+ = \mathbf{e}^+ \times \hat{\mathbf{z}}$. On the other hand, the magnetic current density in the z^- side, \mathbf{m}_0^- , satisfies

$\mathbf{m}_0^- = \mathbf{e}^- \times -\hat{\mathbf{z}}$. Due to the continuity of the electric field in the gaps, \mathbf{e}^+ is equal with \mathbf{e}^- . This results in the magnetic current densities in z^+ and z^- side being equal and opposite, i.e. $\mathbf{m}_0^+ = -\mathbf{m}_0^- = \mathbf{m}_0$.

By imposing the continuity of the tangential magnetic field in the gaps, it can be written that the total field at z^+ is equal to the total field at z^- , i.e. $\mathbf{h}^+ = \mathbf{h}^-$. The field in the upper side is equal to the sum of the scattered field, the incident field and the field reflected by the metal plane. Contrarily, the field in the lower space is only equal to the scattered field. Thus, it can be written that

$$\mathbf{h}_i^+(1 + \Gamma) + \mathbf{h}_s^+ = \mathbf{h}_s^- \quad (2.1)$$

where \mathbf{h}_s^+ and \mathbf{h}_s^- are the tangential magnetic fields radiated by the magnetic current density on each side of the layer. Γ is the reflection coefficient of the magnetic field at the metal plane and it is equal to 1 for PEC. The scattered magnetic field and the magnetic current density, for $z = 0$, are related by the convolution integrals

$$\mathbf{h}_s^\pm(\boldsymbol{\rho}) = \mathbf{m}_0^\pm(\boldsymbol{\rho}) * \mathbf{g}_{\text{PEC}}(\boldsymbol{\rho}) = \pm \int_{-\infty}^{\infty} \int_{-\infty}^{\infty} \mathbf{g}(\boldsymbol{\rho} - \boldsymbol{\rho}') \mathbf{m}_0(\boldsymbol{\rho}') d\boldsymbol{\rho}' \quad (2.2)$$

where $\boldsymbol{\rho} = x\hat{\mathbf{x}} + y\hat{\mathbf{y}}$ and \mathbf{g}_{PEC} is the Green's function that relates the elementary magnetic source located on a PEC infinite plane to the magnetic field. Therefore, by substituting (2.2) into equation (2.1),

$$\int_{-\infty}^{\infty} \int_{-\infty}^{\infty} \mathbf{g}_{\text{PEC}}(\boldsymbol{\rho} - \boldsymbol{\rho}') 2\mathbf{m}_0(\boldsymbol{\rho}') d\boldsymbol{\rho}' = -2\mathbf{h}_i(\boldsymbol{\rho}). \quad (2.3)$$

By applying the image theorem, the magnetic current density that is radiating above the PEC surface is equal to twice the same magnetic current density radiating in the free space ($\mathbf{g}_{\text{PEC}} = 2\mathbf{g}_{\text{FS}}$). Thus, the integral equation (2.3) can be compactly written as

$$\mathbf{m}_0(\boldsymbol{\rho}) * \mathbf{g}(\boldsymbol{\rho}) = -2\mathbf{h}_i(\boldsymbol{\rho}) \quad (2.4)$$

with \mathbf{g} is equal to 4 times of free-space Green's function ($\mathbf{g} = 4\mathbf{g}_{\text{FS}}$).

The tangential component of the incident magnetic field associated with an arbitrary plane wave is in general a superposition of transverse electric (TE) and transverse magnetic (TM) modes that are given by

$$\begin{aligned} \mathbf{h}_{\text{TE}}(\boldsymbol{\rho}, z) &= \frac{1}{\sqrt{d_x d_y}} \hat{\mathbf{k}}_\rho e^{-j\mathbf{k}_\rho \cdot \boldsymbol{\rho}} e^{jk_{z0}z} \\ \mathbf{h}_{\text{TM}}(\boldsymbol{\rho}, z) &= \frac{1}{\sqrt{d_x d_y}} \hat{\boldsymbol{\alpha}} e^{-j\mathbf{k}_\rho \cdot \boldsymbol{\rho}} e^{jk_{z0}z}. \end{aligned} \quad (2.5)$$

Indicating with θ and ϕ the elevation and azimuth angles of incidence, respectively, the propagation constant along x , y , and z are given by $k_{x0} = k_0 \sin\theta \cos\phi$, $k_{y0} = k_0 \sin\theta \sin\phi$, and $k_{z0} = k_0 \cos\theta$, where k_0 is the free-space wavenumber. The vector \mathbf{k}_ρ in the exponential is equal to $k_{x0}\hat{\mathbf{x}} + k_{y0}\hat{\mathbf{y}}$, and the unit vectors of the TE and TM components are defined as

$$\begin{aligned} \hat{\mathbf{k}}_\rho &= \cos\phi\hat{\mathbf{x}} + \sin\phi\hat{\mathbf{y}} \\ \hat{\boldsymbol{\alpha}} &= -\sin\phi\hat{\mathbf{x}} + \cos\phi\hat{\mathbf{y}}. \end{aligned} \quad (2.6)$$

2.1.2 Solutions and Equivalent Layer Reactance for Lossless Case

The integral equation (2.4) is written in terms of the unknown magnetic current distribution on the layer. To solve the equation, a procedure similar to the one in [14] is used. This method involves expanding the magnetic current into four basis functions defined over the entire unit cell (entire-domain):

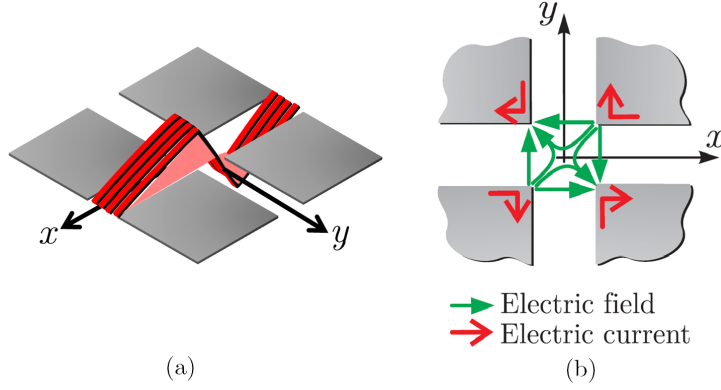


Figure 2.3: (a) Illustration of the uniform transverse distribution with anti-symmetric longitudinality, \mathbf{f}_3 (\mathbf{f}_4 is along y). (b) Illustration of the distribution at junction.

$$\mathbf{m}_0(\boldsymbol{\rho}) = \sum_{p=1}^4 a_p \mathbf{f}_p(\boldsymbol{\rho}) \quad (2.7)$$

where a_p are unknown coefficients, and the basis functions are defined as in [14]:

$$\begin{aligned} \mathbf{f}_1(\boldsymbol{\rho}) &= e^{-jk_{x0}x} \frac{1}{w_y} \Pi_{[-w_y/2, w_y/2]}(y) \hat{\mathbf{x}}, & \mathbf{f}_3(\boldsymbol{\rho}) &= b_{d,x}(x) \frac{1}{w_y} \Pi_{[-w_y/2, w_y/2]}(y) \hat{\mathbf{x}} \\ \mathbf{f}_2(\boldsymbol{\rho}) &= e^{-jk_{y0}y} \frac{1}{w_x} \Pi_{[-w_x/2, w_x/2]}(x) \hat{\mathbf{y}}, & \mathbf{f}_4(\boldsymbol{\rho}) &= b_{d,y}(y) \frac{1}{w_x} \Pi_{[-w_x/2, w_x/2]}(x) \hat{\mathbf{y}}. \end{aligned} \quad (2.8)$$

The longitudinal part of the functions \mathbf{f}_1 and \mathbf{f}_2 describes a phase progression, with wavenumbers k_{x0} and k_{y0} along x and y , respectively. These basis functions represent the linear phase variation of the magnetic current induced in the slots by the incident plane wave. The transverse distribution on the slots is assumed to be constant, hence defined by the function $\Pi_{[a,b]}(\xi) = 1$ for $\xi \in [a, b]$ and 0 elsewhere. The functions \mathbf{f}_1 and \mathbf{f}_2 do not account for the interaction between the currents in the two orthogonal slots occurring at the junction (crossing region between the x - and y -oriented slots). To account for the effects of the junction, two additional basis functions \mathbf{f}_3 and \mathbf{f}_4 are considered, representing anti-symmetric profiles illustrated in Fig. 2.3(a). These currents are equal to zero at the edges of the unit cell and in the center, and they are consistent with the electric field and electric current distributions that occurs in the crossing (Fig. 2.3(b)). The mathematical expression of the longitudinal distribution is given by

$$\begin{aligned} b_{d,x}(x) &= - \left(e^{jk_0x} + \Gamma_x e^{-jk_0x} \right) \Pi_{[-d_x/2, -w_x/2]}(x) + \left(e^{-jk_0x} + \Gamma_x e^{jk_0x} \right) \Pi_{[w_x/2, d_x/2]}(x) \\ &\quad + C_x x \Pi_{[-w_x/2, w_x/2]}(x). \end{aligned} \quad (2.9)$$

where $C_x = (2/w_x)(e^{-jk_0w_x/2} + \Gamma_x e^{jk_0w_x/2})$ and $\Gamma_x = -e^{-jk_0d_x}$ is the reflection coefficient at the edges of the unit cell. The function $b_{d,y}(y)$ follows the same formula, by replacing x with y .

By substituting the expansion (2.7) in the integral equation (2.4) and applying Galerkin projection, a linear system of equations can be defined:

$$\begin{aligned} a_1 Y_{11} + a_2 Y_{12} + a_3 Y_{13} + a_4 Y_{14} &= i_1 \\ a_1 Y_{21} + a_2 Y_{22} + a_3 Y_{23} + a_4 Y_{24} &= i_2 \\ a_1 Y_{31} + a_2 Y_{32} + a_3 Y_{33} + a_4 Y_{34} &= i_3 \\ a_1 Y_{41} + a_2 Y_{42} + a_3 Y_{43} + a_4 Y_{44} &= i_4. \end{aligned} \quad (2.10)$$

where $Y_{qp} = \langle \mathbf{g} * \mathbf{m}_p, \mathbf{m}_q \rangle$, and $i_q = \langle -2\mathbf{h}_i, \mathbf{m}_q \rangle$; p and q are the indexes indicating the basis and the test functions. A projection operator is also introduced, which is defined as

$$\langle f_p, f_q \rangle = \int_{-\infty}^{\infty} \int_{-\infty}^{\infty} f_p(x, y) f_q^*(x, y) dx dy \quad (2.11)$$

with f_p , and f_q are generic functions of the variables x, y .

From the linear system of equations described in (2.10), an admittance matrix $\bar{\bar{\mathbf{Y}}}$ and a vector of known terms $\bar{\mathbf{i}}$ can be defined, which satisfy

$$\bar{\bar{\mathbf{Y}}} \bar{\mathbf{a}} = \bar{\mathbf{i}} \quad (2.12)$$

where $\bar{\mathbf{a}} = (a_1 a_2 a_3 a_4)^T$ is the vector of unknown coefficients and $\bar{\mathbf{i}} = (i_1 i_2 i_3 i_4)^T$ is the vector of the projection of the incident magnetic field onto the testing functions. This equations can be solved for generic plane-wave incidence by inverting the admittance matrix (2.12) in order to find the unknowns.

A number of considerations can be made to allow the derivation of the solution in a closed form and provide physical insight. For sub-wavelength array periods, the projections of the plane wave onto the anti-symmetric profile functions can be neglected, since the positive and negative parts of these odd functions result in equal and opposite contributions and cancel out [14]. This is equivalent to assuming that $i_3 \approx i_4 \approx 0$ and $Y_{13} \approx Y_{31} \approx Y_{24} \approx Y_{42} \approx 0$. Such approximation allow to simplify the problem in a system of only two linear equations and to define a reduced admittance matrix $\bar{\bar{\mathbf{Y}}}_r$, with 2×2 elements, as described in Appendix A (Sec. A.2).

For deriving an equivalent model that describes the scattering of a plane wave impinging on the layer, it is convenient to evaluate the admittance and the forcing terms in the spectral domain. All terms of the admittance matrix can be written in closed form as shown in Appendix A. The reduced matrix can be multiplied by rotation matrices as explained in Sec. A.3, to highlight the relation with the TE and TM component of the plane wave. This defines the matrix $\bar{\bar{\mathbf{Y}}}_{\text{TETM}}$ is written as sum of three contributions

$$\bar{\bar{\mathbf{Y}}}_{\text{TETM}} = \bar{\bar{\mathbf{Y}}}_{\text{TL}} + \bar{\bar{\mathbf{Y}}}_{\text{layer}} + \bar{\bar{\mathbf{Y}}}_{\text{cou}} \quad (2.13)$$

where

$$\bar{\bar{\mathbf{Y}}}_{\text{TL}} = \begin{bmatrix} \frac{2}{Z_{0\text{TE}}} & 0 \\ 0 & \frac{2}{Z_{0\text{TM}}} \end{bmatrix} \quad (2.14)$$

$$\bar{\bar{\mathbf{Y}}}_{\text{layer}} = \begin{bmatrix} jB_s \left(1 - \frac{\sin^2 \theta}{2}\right) & 0 \\ 0 & jB_s \end{bmatrix} \quad (2.15)$$

$$\bar{\bar{\mathbf{Y}}}_{\text{cou}} = \begin{bmatrix} Y_c \frac{\sin^2 \theta \cos^2(2\phi)}{2} & -Y_c \frac{\sin^2 \theta \sin(2\phi) \cos(2\phi)}{2} \\ -Y_c \frac{\sin^2 \theta \sin(2\phi) \cos(2\phi)}{2} & Y_c \frac{\sin^2 \theta \sin^2(2\phi)}{2} \end{bmatrix}. \quad (2.16)$$

The wave impedances of the TE and TM modes are introduced as $Z_{0\text{TE}}$ and $Z_{0\text{TM}}$. The slot self-susceptance is denoted by B_s and a coupling admittance term Y_c is introduced to describe the coupling between TE and TM modes. In fact, it can be noted that the only off-diagonal terms are proportional to Y_c . It is demonstrated in [14] that the term Y_c asymptotically goes to zero for electrically small cell sizes, up to about a quarter wavelength ($\bar{\bar{\mathbf{Y}}}_{\text{cou}} \approx \mathbf{0}$). Thus, the entire matrix becomes diagonal, which means that an array of electrically small patches does not couple TE and TM modes of an incident plane wave.

The admittance matrix $\bar{\bar{\mathbf{Y}}}_{\text{TETM}}$ can be represented with the equivalent transmission line models shown in Fig. 2.4. The term $\bar{\bar{\mathbf{Y}}}_{\text{TL}}$ can be described as two transmission lines associated with the propagation

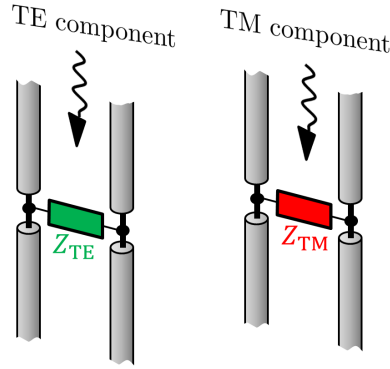


Figure 2.4: Equivalent circuit representation of the layer reactance of a single layer of patches.

of the incident, reflected and transmitted TE and TM waves. The characteristic impedances are given by $Z_{0\text{TE}} = \zeta_0 k_0 / k_{z0}$ and $Z_{0\text{TM}} = \zeta_0 k_{z0} / k_0$ where ζ_0 is the free-space impedance (or, more in general, the impedance of the medium hosting the layer).

The term $\bar{\bar{Y}}_{\text{layer}}$ refers to the equivalent reactance of the layer and is related to the susceptance B_s defined as the following sum of higher order Floquet modes [14]:

$$B_s \approx \frac{2k_0}{\zeta_0} \sum_{m_y \neq 0} \frac{|\text{sinc}(k_{ym} \frac{w_y}{2})|^2}{|k_{ym}|} \quad (2.17)$$

where $k_{ym} = k_{y0} - 2\pi m_y / d_y$ is the Floquet wavenumber with index m_y . In the described analysis, a square structure is considered, therefore $d_x = d_y = d$ and $w_x = w_y = w$. Also, the wavenumbers $k_{ym} \approx -2\pi m_y / d_y$ by noting that, for higher order modes, $k_{y0} \ll 2\pi m_y / d_y$. Equation (2.17) then becomes

$$B_s \approx \frac{k_0 d}{\zeta_0 \pi} \sum_{m \neq 0} \frac{|\text{sinc}(\pi m \frac{w}{d})|^2}{|m|}. \quad (2.18)$$

Equation (2.18) shows that the susceptance of the layer depends on the ratio between the slot width and the periodicity of the patches. It is also evident that this structure is azimuthal independent (scatters the same way for any ϕ), as all the quantities involved in the equivalent transmission line models do not depend on ϕ . The impedance (reactance) of the layer in Fig. 2.4 is related to the susceptance as:

$$Z_{\text{TE}} = -\frac{j}{B_s} \frac{1}{1 - \sin^2 \theta}, \quad Z_{\text{TM}} = -\frac{j}{B_s}. \quad (2.19)$$

To assess these formulas for TE and TM incidence, CST [22] simulations are made and the simulated scattering parameters are compared to the analytical results. Figure 2.5 shows the comparison between amplitude and phase of the reflection and transmission coefficient of different plane wave incidence on a single layer of square patches. The geometrical parameters of the layer of patches are $d_x = d_y = 0.0785\lambda_0$, $w_x = w_y = 0.01\lambda_0$, with λ_0 being the wavelength at calculation frequency. It can be seen that a good agreement between analytical solution and CST simulation is present for all cases.

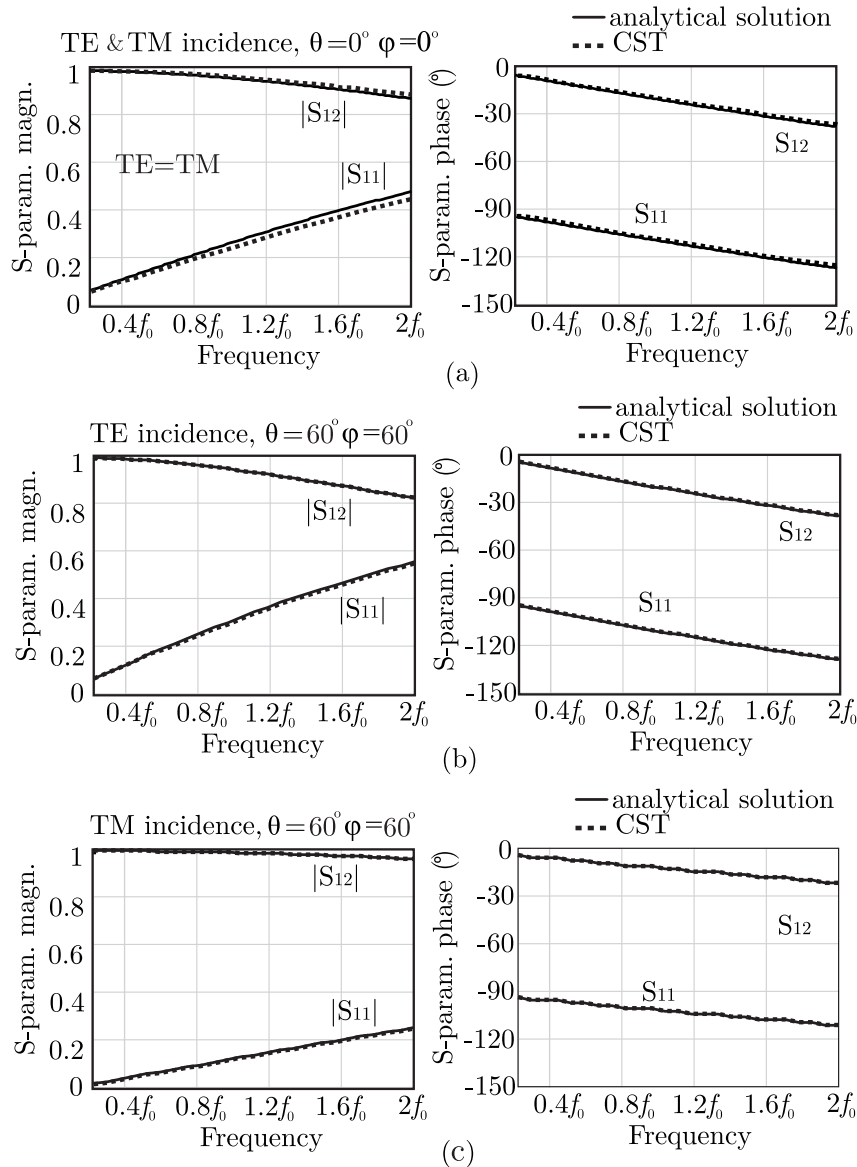


Figure 2.5: Amplitude and phase of the reflection and transmission coefficients of a plane wave incident on a single layer of square patches, comparing analytical solution presented in this part with CST simulation: (a) TE and TM, broadside incidence; (b) TE incidence $\theta = 60^\circ$, $\phi = 60^\circ$; (b) TM incidence $\theta = 60^\circ$, $\phi = 60^\circ$. The geometrical parameters are $d_x = d_y = 0.0785\lambda_0$, $w_x = w_y = 0.01\lambda_0$, with λ_0 being the wavelength at 5 GHz.

2.2 Single Layer of Periodic Square Patches with Finite Conductivity

In the previous section, a single layer of periodic patches is studied and the patches are modeled as PEC. It allows to use the image theorem and results in an equivalent problem where the currents are radiating in free-space.

However, realistically, the metal patches will possess a certain conductivity σ . For example, in [24] an ADL is realized with layers of metal patches made of pure aluminum which has conductivity $\sigma = 2.6 \times 10^7 \text{S/m}$. Another design presented in [25] uses gold with $\sigma = 4.09 \times 10^7 \text{S/m}$. It is known that losses in artificial dielectric are very low, because of the non-resonant nature of the sub-wavelength

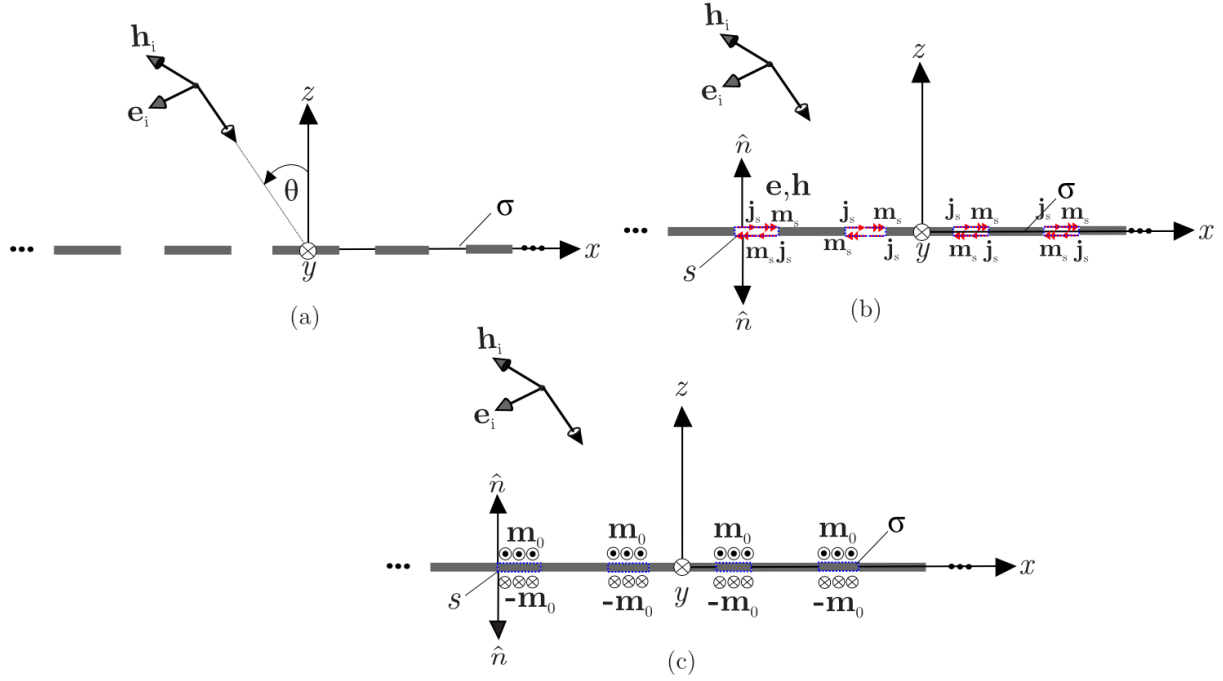


Figure 2.6: (a) Original problem which consists of a single layer of periodic square patches illuminated with generic plane wave illumination. (b) Applying equivalence theorem onto the gaps. (c) Filling the enclosed surface with the same material as the patches.

patches, that support very low current intensity. However, it is useful to include the finite conductivity of the metal already in the analytical formulas, to quantify how low these losses are.

A rigorous method for analyzing a radial line slot array was presented in [26]. The analysis includes an approach to formulate the problem in terms of effective magnetic current. The effective magnetic currents take into account also for the equivalent electric currents which cannot be any longer neglected as for the lossless case. This approach gives an advantage of reducing the number of the unknowns. This method is also used in this thesis because it leads to the possibility of formulating the problem in the similar way as the lossless case.

2.2.1 Problem Definition and Equivalence Principle for Lossy Case

The problem definition is similar to the one of the previous section, which is a layer of periodic square patches along xy plane, illuminated by a generic plane wave (see Fig. 2.6(a)). Due to finite conductivity σ , the metal can be characterized by the conductivity σ , which relates to the surface impedance Z_s that is given by

$$Z_s = (1 + j) \sqrt{\frac{k_0 \zeta_0}{2\sigma}} \quad (2.20)$$

where k_0 and ζ_0 are the free-space wave number and impedance, respectively.

The metal surface is modeled using the Leontovich boundary condition [27,28]: $\mathbf{e} \times \hat{\mathbf{n}} = Z_s \hat{\mathbf{n}} \times [\mathbf{h} \times \hat{\mathbf{n}}]$, where $\hat{\mathbf{n}}$ is the outward normal unit vector of the surface. Following the equivalence theorem, the gaps are enclosed with infinitely thin closed surfaces S , illustrated in Fig. 2.6(b). The fields \mathbf{e} and \mathbf{h} denote the total fields, equal to the sum of incident and scattered. The surface electric and magnetic current density, \mathbf{j}_s and \mathbf{m}_s , are related to these fields by $\mathbf{j}_s = \hat{\mathbf{n}} \times \mathbf{h}$ and $\mathbf{m}_s = \mathbf{e} \times \hat{\mathbf{n}}$.

The field inside the surface is zero, thus the volume that is enclosed by S can be filled with any type of

material leading to different formulations of the equivalence principle. Typically, in method of moments formulations for apertures, the volumes are filled with a PEC, which is also done in the previous section. This choice makes the equivalent electric current densities to cancel out with their images, hence their contribution is vanished, and only unknown magnetic current densities are left to be solved.

However, filling this enclosed surface with PEC for this case will cause an inhomogeneity across the plates where the magnetic currents are located, so that the spectral Green's function of layered medium cannot be used. Thus, it is convenient to fill the volume enclosed by the surface S with material which possesses the same finite conductivity as the metal patches, as shown in Fig. 2.6(c).

Consequently, both electric and magnetic equivalent surface current densities \mathbf{j}_s and \mathbf{m}_s are present. An effective magnetic current density \mathbf{m}_e , that account for both \mathbf{j}_s and \mathbf{m}_s , can be defined as in [26]:

$$\mathbf{m}_e = \mathbf{m}_s + \mathbf{m}_j = \mathbf{m}_s + Z_s \hat{\mathbf{n}} \times \mathbf{j}_s. \quad (2.21)$$

The effective magnetic current density on the z^+ and z^- , denoted by \mathbf{m}_e^+ and \mathbf{m}_e^- respectively, can be written as

$$\begin{aligned} \mathbf{m}_e^+ &= \mathbf{m}_s^+ + \mathbf{m}_j^+ = \mathbf{e}^+ \times \hat{\mathbf{z}} + Z_s \hat{\mathbf{z}} \times (\hat{\mathbf{z}} \times \mathbf{h}^+) \\ \mathbf{m}_e^- &= \mathbf{m}_s^- + \mathbf{m}_j^- = \mathbf{e}^- \times (-\hat{\mathbf{z}}) + Z_s (-\hat{\mathbf{z}}) \times (-\hat{\mathbf{z}} \times \mathbf{h}^-) = -\mathbf{m}_s^+ + \mathbf{m}_j^+. \end{aligned} \quad (2.22)$$

The superscripts '+' and '-' are used to indicate the current, the field or the position above and below the layer plane. Thus, by imposing the continuity of the tangential magnetic field in the gaps, it can be written that

$$\mathbf{h}_i(z^+)(1 + \Gamma) + \mathbf{h}_s(z^+) = \mathbf{h}_s(z^-) + \mathbf{h}_{\text{transm}}(z^-) \quad (2.23)$$

where Γ is the reflection coefficient of the magnetic field at the metal, and $\mathbf{h}_{\text{transm}}(z^-)$ is the magnetic field that transmitted to the z^- space. For a realistic conductive losses, an approximation that $\mathbf{h}_{\text{transm}}(z^-) \approx 0$ is a made. The $\mathbf{h}_s(z^+)$ and $\mathbf{h}_s(z^-)$ are the magnetic fields scattered by the effective magnetic current density in z^+ and z^- space. These scattered magnetic field and the magnetic current density, for $z = 0$, are related by the convolution integral which can be written as

$$\begin{aligned} (\mathbf{m}_s^+(\boldsymbol{\rho}) + \mathbf{m}_j^+(\boldsymbol{\rho}) + \mathbf{m}_s^+(\boldsymbol{\rho}) - \mathbf{m}_j^+(\boldsymbol{\rho})) * \mathbf{g}_{Z_s}(\boldsymbol{\rho}) &= -\mathbf{h}_i(\boldsymbol{\rho})(1 + \Gamma) \\ 2\mathbf{m}_s^+(\boldsymbol{\rho}) * \mathbf{g}_{Z_s}(\boldsymbol{\rho}) &= -\mathbf{h}_i(\boldsymbol{\rho})(1 + \Gamma) \end{aligned} \quad (2.24)$$

where $\boldsymbol{\rho} = x\hat{\mathbf{x}} + y\hat{\mathbf{y}}$ and \mathbf{g}_{Z_s} is the Green's function that relates the elementary magnetic source located on the infinite lossy plane to the magnetic field. One can note that the magnetic currents \mathbf{m}_j do not contribute to the magnetic field integral equation. Therefore, contrarily to the case presented in [26], the integral equation can be written only in terms of magnetic current densities. This is because, unlike [26], the Green's functions for the currents above and below the layer are the same in the problem under analysis.

Thus, by using a notation similar to the lossless case ($\mathbf{m}_s = \mathbf{m}_0$), the problem becomes the one in Fig. 2.6(c) and the integral equation at that point $z = 0$ is given by

$$\int_{-\infty-\infty}^{\infty} \int_{-\infty}^{\infty} 2\mathbf{m}_0(\boldsymbol{\rho}') \mathbf{g}_{Z_s}(\boldsymbol{\rho} - \boldsymbol{\rho}', n_z d_z, z=0) d\boldsymbol{\rho}' = -(1 + \Gamma)\mathbf{h}_i. \quad (2.25)$$

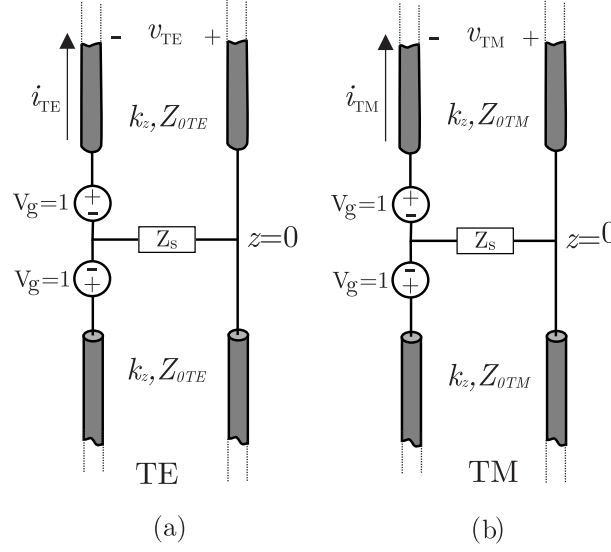


Figure 2.7: Equivalent z -transmission lines for the problem showing (a) TE and (b) TM modes for a magnetic source.

2.2.2 Solutions and the Equivalent Reactance for Lossy Case

Equation (2.25) can be solved by an appropriate expansion of the magnetic current in four basis functions (like the lossless case) and Galerkin projection. The term of the admittance matrix are calculated in the spectral domain. For this reason the spectral Green's function should be derived.

Due of the finite conductivity of the layer, image theorem cannot be employed. Thus, the Green's function in this integral equation is no longer the one of free space. The general expression of the dyadic spectral Green's function, relating magnetic field h to an elementary magnetic current m , is given by

$$\overline{\overline{G}}^{hm}(k_x, k_y, z) = \begin{pmatrix} G_{xx}^{hm} & G_{xy}^{hm} \\ G_{yx}^{hm} & G_{yy}^{hm} \end{pmatrix} = \begin{pmatrix} -\frac{i_{TE}(z)k_x^2 + i_{TE}(z)k_y^2}{k_p^2} & \frac{(i_{TM}(z) - i_{TE}(z))k_x^2 k_y^2}{k_p^2} \\ \frac{(i_{TM}(z) - i_{TE}(z))k_x^2 k_y^2}{k_p^2} & -\frac{i_{TM}(z)k_x^2 + i_{TE}(z)k_y^2}{k_p^2} \end{pmatrix}. \quad (2.26)$$

The entries of (2.26) are written in terms of the current i and voltage v on the equivalent transmission lines (TE and TM) along z , shown in Fig. 2.7. The subscripts 'TE' and 'TM' denotes the modes, and the characteristic impedance of the transmission lines are $Z_{0TE} = \zeta_0 k_0 / k_z$ and $Z_{0TM} = \zeta_0 k_z / k_0$ where k_z is $\sqrt{k_0^2 - k_x^2 - k_y^2}$. The magnetic current sources are replaced by voltage generators.

In the integral equation the Green's function at $z = 0$ is employed. Solving Fig. 2.7(a), to find current at $z = 0$ (similar to one that is detailed in Appendix C) will give

$$i_{TE}(z=0) = \frac{2}{Z_{0TE} + 2Z_s}, \quad i_{TM}(z=0) = \frac{2}{Z_{0TM} + 2Z_s}. \quad (2.27)$$

which leads to the Green's function for this specific case of metal layer with finite conductivity. After the Green's function is obtained, the rest of the steps are identical to the lossless case. A new term is included, i.e. the surface impedance of the metal patches. The impedance of the layer is given by:

$$Z_{\text{layer,TE}} = Z_{TE} + Z_s, \quad Z_{\text{layer,TM}} = Z_{TM} + Z_s \quad (2.28)$$

where

$$Z_{TE} = \frac{1}{Y_{s,TE}}, \quad Z_{TM} = \frac{1}{Y_{s,TM}}. \quad (2.29)$$

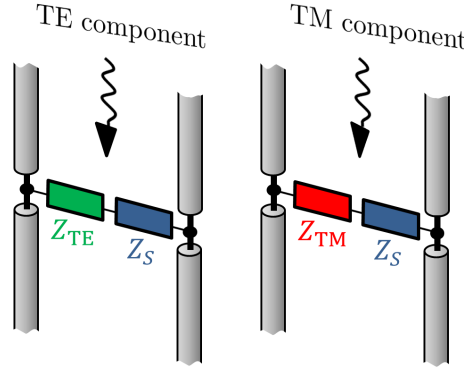


Figure 2.8: Equivalent circuit representation of the single layer of patches with finite conductivity.

The equivalent admittances of the layer, $Y_{s,TE}$ and $Y_{s,TM}$, are different terms than the ones in the lossless case, in the sense that they are not any longer a pure susceptance. These admittances, assuming that the patches are square, are given by

$$\begin{aligned}
 Y_{s,TE} &\approx -2j \sum_{m_y \neq 0} \left| \text{sinc}\left(k_{ym} \frac{w_y}{2}\right) \right|^2 \left(\frac{k_{x0}^2}{2k_{\rho m}^2} \left(\zeta_0 \frac{k_0}{k_{zm}} + 2Z_s \right)^{-1} + \left(\frac{k_{ym}^2}{k_{\rho m}^2} \left(\zeta_0 \frac{k_{zm}}{k_0} + 2Z_s \right)^{-1} \right) \right) \\
 Y_{s,TM} &\approx -2j \sum_{m_x \neq 0} \left| \text{sinc}\left(k_{xm} \frac{w_x}{2}\right) \right|^2 \left(\frac{k_{y0}^2}{k_{\rho m}^2} \left(\zeta_0 \frac{k_0}{k_{zm}} + 2Z_s \right)^{-1} + \left(\frac{k_{xm}^2}{k_{\rho m}^2} \left(\zeta_0 \frac{k_{zm}}{k_0} + 2Z_s \right)^{-1} \right) \right)
 \end{aligned} \quad (2.30)$$

where m_x and m_y are the indexes of the Floquet modes, $k_{xm} = k_{x0} - 2\pi m_x/d_x$ and $k_{ym} = k_{y0} - 2\pi m_y/d_y$ are the Floquet wavenumbers, which determine $k_{zm} = \sqrt{k_0^2 - k_{xm}^2 - k_{ym}^2}$ and $k_{\rho m} = \sqrt{k_{xm}^2 + k_{ym}^2}$; $k_{x0} = k_0 \sin\theta \cos\phi$ and $k_{y0} = k_0 \sin\theta \sin\phi$ are the propagation constant of the incident plane wave along x and y , respectively. Equation given in (2.29) and (2.30) will also be valid for the lossless case, as it gives the same formula found in the previous section when $Z_s = 0$.

Figure 2.8 shows the equivalent circuit representation of the impedance, including the Z_s contribution. It can be deduced that the finite conductivity introduces an impedance term (Z_s) that is in series with the layer impedance. It is also important to note that the term Z_s is not the only contribution to the resistance but also the impedance Z_{TE} and Z_{TM} have a comparable resistive component.

To quantify the effect of the finite conductivity, the losses are defined as

$$\text{Loss}(dB) = 10 \log_{10} \frac{1}{|S_{11}|^2 + |S_{12}|^2} \quad (2.31)$$

where S_{11} and S_{12} are reflection and transmission coefficient, respectively. To validate the analytical solutions, full-wave HFSS simulations are made. Since the losses of the structure with realistic conductivity values are negligible, an unrealistically low conductivity of $\sigma = 1000$ S/m is taken for the validation. The single layer of patches geometrical parameters are $d_x = d_y = 0.095\lambda_0$, $w_x = w_y = 0.01\lambda_0$, with λ_0 being the wavelength at 300 GHz. The incident plane wave are coming from oblique angles ($\theta = 40^\circ$ $\phi = 0^\circ$, and $\theta = 60^\circ$ $\phi = 0^\circ$).

Figure 2.10 and 2.9 compare the analytical solution with the result from simulations the scattering parameters and for the loss, respectively. It can be seen from the scattering parameters that the analytical solution reported in this section is showing an excellent agreement with the commercial solver.

It is also evident that the loss calculated for TE incidence is generally larger than the value observed for TM incidence. This phenomenon likely happens due to the occurrence of electric current loops that are supported by the patches when the structure is illuminated by TE incidence. Figure 2.11(a) shows the electric field distribution on the single layer for TE incidence, and the correspondent electric current

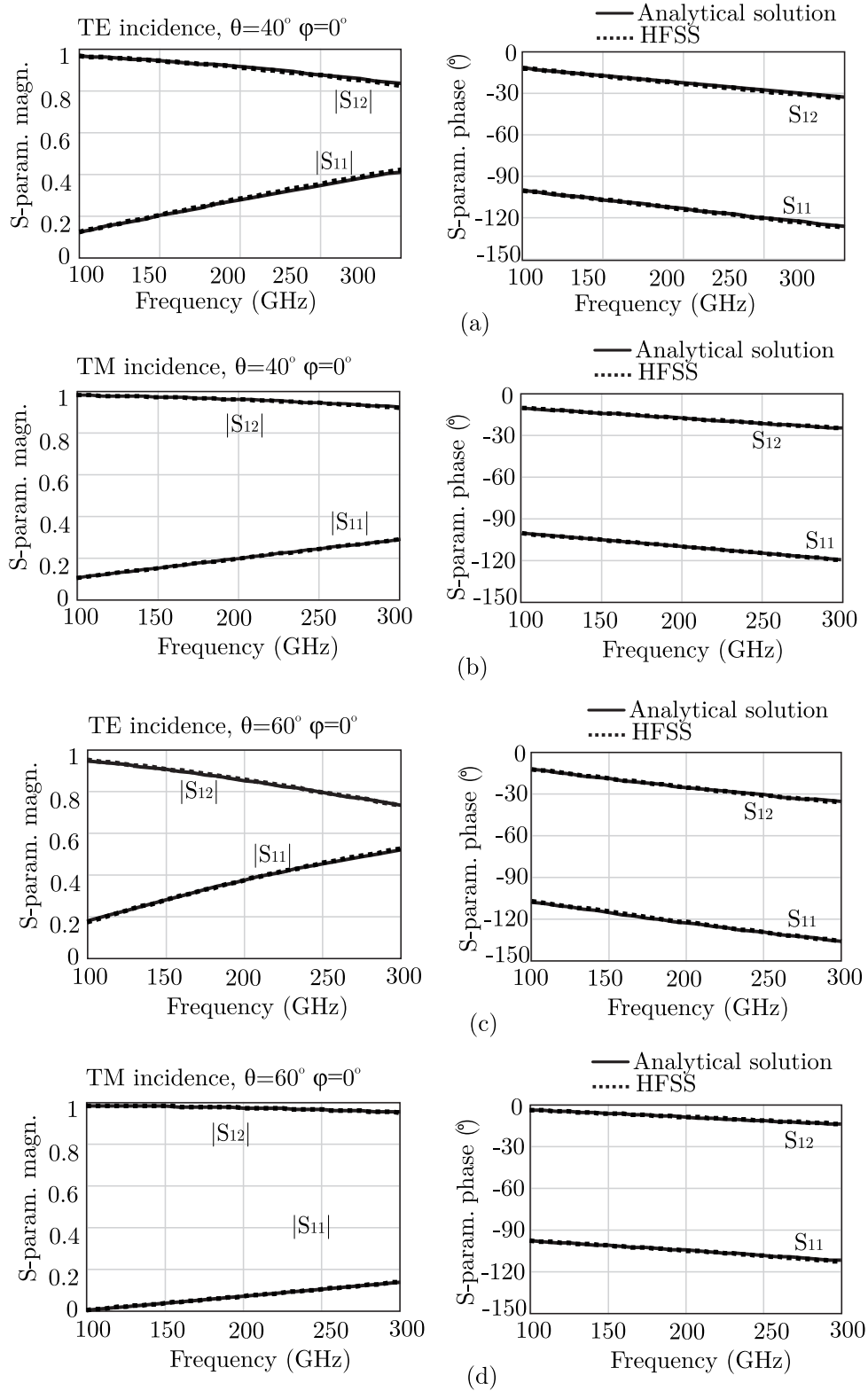


Figure 2.9: Comparison between analytical solution and HFSS simulation of amplitude and phase of the reflection and transmission coefficients of a plane wave incident on a single layer of patches with finite conductivity ($\sigma = 1000 S/m$): (a) TE, $\theta = 40^\circ$, $\phi = 0^\circ$; (b) TM, $\theta = 40^\circ$, $\phi = 0^\circ$; (c) TE, $\theta = 60^\circ$, $\phi = 0^\circ$; (d) TM, $\theta = 60^\circ$, $\phi = 0^\circ$. The geometrical parameters are $d_x = d_y = 0.095\lambda_0$, $w_x = w_y = 0.01\lambda_0$, with λ_0 being the wavelength at 300 GHz.

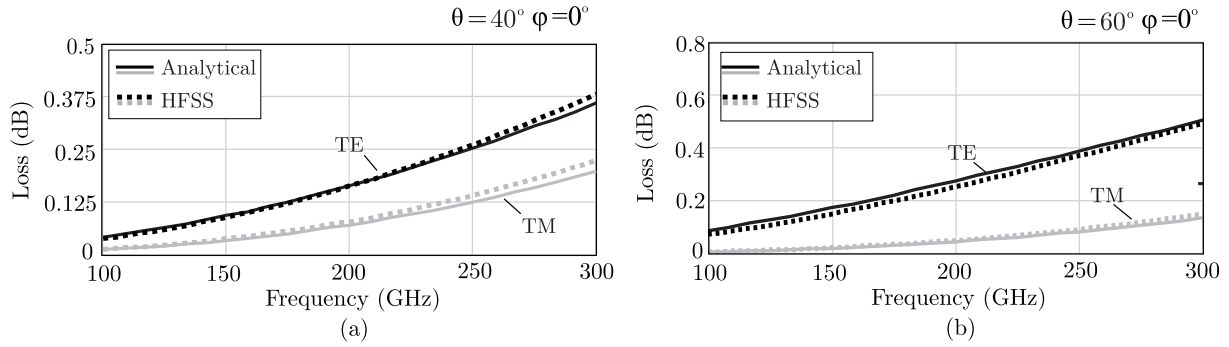


Figure 2.10: Comparing loss (in dB) calculated based on analytical solution and HFSS simulation. The plane wave incident on a single layer of patches with finite conductivity ($\sigma = 1000$ S/m) with angle of incidence: (a) $\theta = 40^\circ$, $\phi = 0^\circ$; (b) $\theta = 60^\circ$, $\phi = 0^\circ$. The geometrical parameters of layer of patches are $d_x = d_y = 0.095\lambda_0$, $w_x = w_y = 0.01\lambda_0$, with λ_0 being the wavelength at 300 GHz.

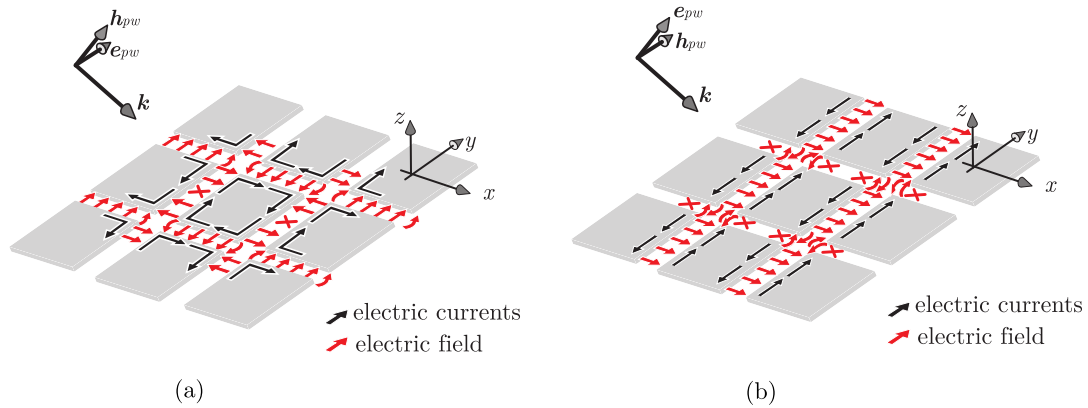


Figure 2.11: Illustration on single layer of periodic patches illuminated by (a) TE incidence (b) TM incidence. It is evident that the electric fields that are propagating in the slot generate electric current loops in the patches in TE incidence, while in TM incidence the patches does not support such current loop.

on the patches forming a loop. A TM incidence is instead not supporting such current loops, but only excites uniform and singly polarized currents on the patches, as shown in Fig. 2.11(b). The current loops are associated with a long electrical length, and therefore with higher current intensity (closer to the resonance), which can explain the increased Ohmic losses.

Chapter 3

Analysis of ADLs Composed of Non-Aligned Layers

3.1 Formulation and Approximation of Current Distribution for Shifted ADLs

Artificial dielectric layers (ADLs), as described in chapter 1 and chapter 2, are cascades of layers of periodic patches. This is done so that an ADL realizes an equivalent dielectric slab, which has been demonstrated in [11] not to introduce surface waves when used as an antenna superstrate. In realistic designs [11, 13, 24, 29, 30], the layers are closely spaced, causing the interlayer interaction to become dominant and significantly changes the reactance that the layer would have in isolation [15]. Due to the interaction between layers that is not negligible, it is important to extend the formulation of the single layer to account for this interaction and to arrive to a rigorous analytical method for real ADL designs.

An analysis of artificial dielectrics (ADs) consisting of spheres is modeled in [31], which results in an isotropic material. This thesis focuses on the ADs composed of a layer of patches, known as ADL. While [10] already reported a theory for planar ADs, it is rigorous only for an infinite strips structure. In order to characterize a realistic ADL, a three-dimensional analysis of AD slabs with finite height has to be considered. An analysis of the cascade of multiple layers was presented in [32–34]. These analytical methods were accounting only for the fundamental Floquet wave, consequently neglecting the higher-order coupling between adjacent layers. Accordingly, these techniques fail to accurately model the cascade of layers when the distance between adjacent layers is small compared to the unit cell period. In practical AD designs [35], such a distance can be in the order of one hundredth of the wavelength. To rigorously account for the reactive coupling between parallel adjacent layers, some methods such as generalized admittance matrix and multimode equivalent networks [36, 37] can be used. The drawback of such methods is that they lead to rather complex equivalent networks.

The work presented in [15] gives a novel approach to characterize ADLs with finite height analytically. It expands the closed-form formulation developed for a single layer of patches by including the higher-order interaction between adjacent layers. It also treated infinite and semi-infinite cascades of layers. This analysis though, is valid only when the layers are aligned.

It is explained in chapter 1 that introducing a shift between alternate layers is relevant for ADLs design as the shift significantly increases the effective permittivity of the slab with respect to the aligned case, thus, introducing another important degree of freedom in ADLs design. The closed-form expressions for the equivalent reactance of the layers have to be generalized from aligned to non-aligned cases to also account for the shift between alternating layers.

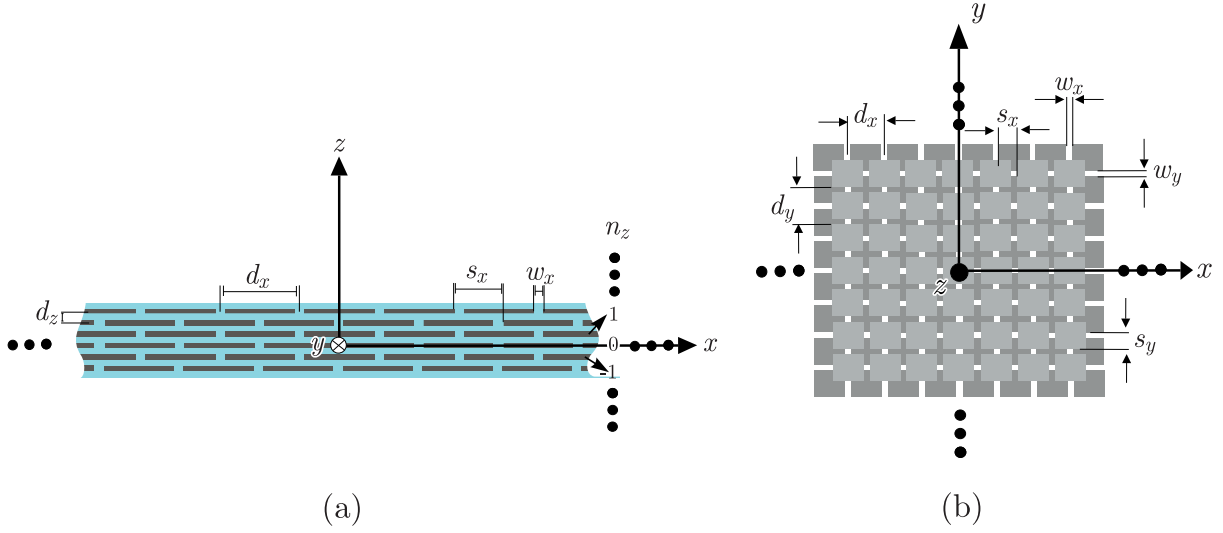


Figure 3.1: Definition of the geometrical parameters characteristic of the shifted ADLs: (a) cross section and (b) top view.

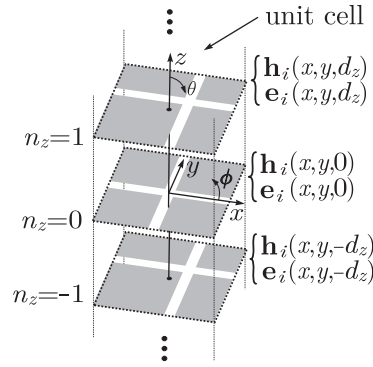


Figure 3.2: Aperture fields on three layers of an infinite cascade of ADLs.

To start the formulation, the problem is defined, including the shift between alternate layer into consideration and then the equivalence principle is applied to obtain the integral equation formulation. In this thesis, the periodic cell is redefined as a combination of two layers, instead of one as in [15], because of the shift between the alternate layers.

3.1.1 Problem Definitions and Equivalence Principle for Shifted ADLs

Consider an ADL composed by an infinite number of layers spaced along z by distance d_z and numbered with consecutive integer indexes n_z , as shown in Fig. 3.1(a). The analysis is started with assuming the patches to have perfect conductivity.

The odd layers ($n_z = [\dots -3, -1, 1, 3, \dots]$) are shifted with respect to the even layers ($n_z = [\dots, -2, 0, 2, \dots]$) by s_x and s_y along x and y , respectively, as depicted in Fig. 3.1(b). The plane wave is assumed to travel in the negative z -direction within the ADL medium, with electric and magnetic field indicated by $\mathbf{e}_i(x, y, z)$ and $\mathbf{h}_i(x, y, z)$, respectively (shown in Fig. 3.2).

By applying the equivalence theorem as in previous chapter for single layer, three surfaces S_1 , S_0 and S_{-1} as shown in Fig. 3.3(a) can be defined, denoting with '1' and '2' the two regions above and below the layer located at $z = 0$. The volume bounded by the surfaces can be filled with a perfect electric conductor (PEC), as shown in Fig. 3.3(b), according to the Schelkunoff's version of the equivalence principle [23],

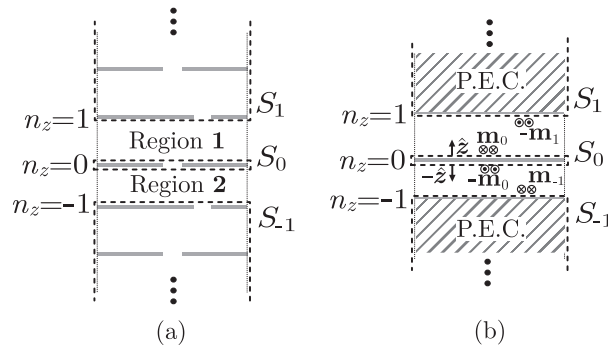


Figure 3.3: (a) original problem and (b) equivalent problem with unknown magnetic current distributions.

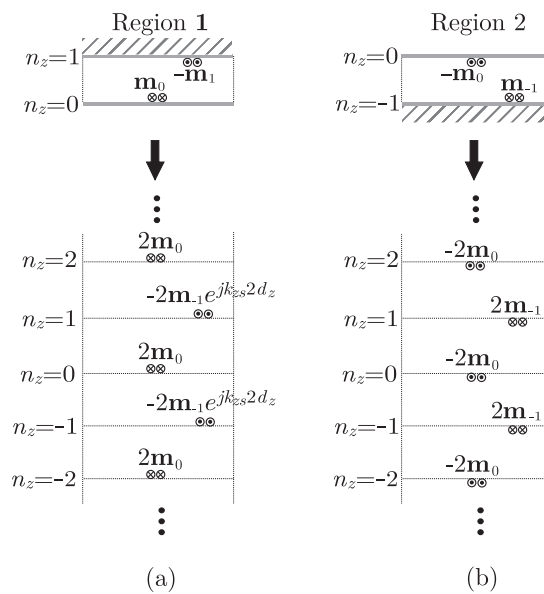


Figure 3.4: Application of image theorem for (a) Region 1 and (b) Region 2, defined in Fig. 3.4.

so that only equivalent surface magnetic currents $\mathbf{m}_{n_z}(x, y)$ are present in the regions corresponding with the gaps between patches in the initial problem.

The equivalent magnetic currents are related to the aperture electric field as

$$\mathbf{m}(x, y, z = n_z d_z \pm \varepsilon) = \mp \hat{\mathbf{z}} \times \mathbf{e}_i(x, y, z = n_z d_z \pm \varepsilon) = \pm \mathbf{m}_{n_z}(x, y) \quad (3.1)$$

with ε being a vanishingly small distance. It is evident from (3.1) that the two magnetic current distributions above and below the layer $n_z = 0$ are equal and opposite, since the normal unit vector changes sign and the tangential electric field is continuous in the gap.

Due to the periodicity along z , we can impose Floquet boundary conditions, i.e. the magnetic currents on the layers at $n_z = 1$ and $n_z = -1$ are related by a phase shift

$$\mathbf{m}_1(x, y) = \mathbf{m}_{-1}(x, y) e^{jk_{zs}2d_z} \quad (3.2)$$

where k_{zs} is an unknown equivalent wavenumber describing the propagation along z .

By applying the image theorem, we can replace the problem in Fig. 3.3(b) with an infinite sum of current contributions for the Region 1 and the Region 2, as depicted in Fig. 3.4. Hence, the boundary conditions for the transverse magnetic field at the layer at $z = 0$ lead to the following integral equation:

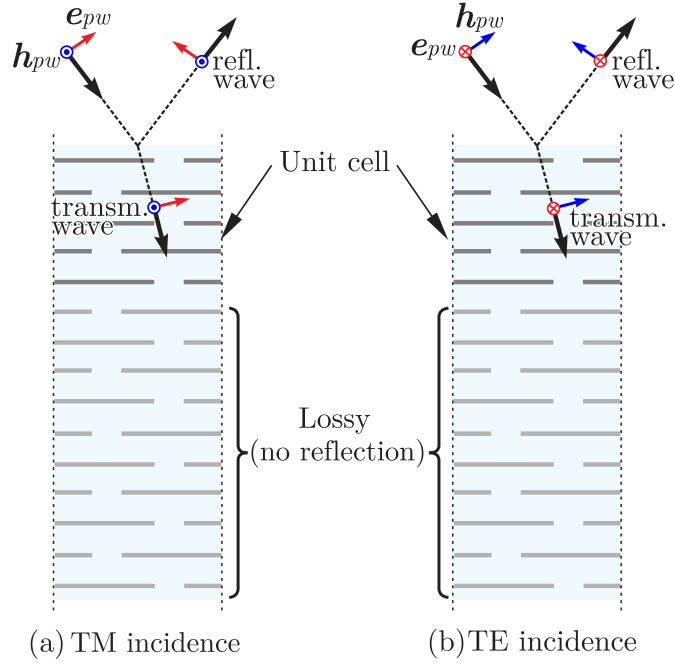


Figure 3.5: Description of the CST models used to simulate a semi-infinite cascade of layers. A lossy ADL with the same geometrical parameters is implemented so that the transmitted wave experiences low reflection.

$$\begin{aligned} & \sum_{n_z, \text{even}} \int_{-\infty}^{\infty} \int_{-\infty}^{\infty} 4\mathbf{m}_0(\boldsymbol{\rho}') \mathbf{g}(\boldsymbol{\rho} - \boldsymbol{\rho}', n_z d_z, z=0) d\boldsymbol{\rho}' = \\ & \sum_{n_z, \text{odd}} \int_{-\infty}^{\infty} \int_{-\infty}^{\infty} 2(e^{jk_{zs} 2d_z} + 1) \mathbf{m}_{-1}(\boldsymbol{\rho}') \mathbf{g}(\boldsymbol{\rho} - \boldsymbol{\rho}', n_z d_z, z=0) d\boldsymbol{\rho}' \end{aligned} \quad (3.3)$$

where $\boldsymbol{\rho} = x\hat{\mathbf{x}} + y\hat{\mathbf{y}}$ and $\boldsymbol{\rho}' = x'\hat{\mathbf{x}} + y'\hat{\mathbf{y}}$ are the observation and the source points, respectively. The function \mathbf{g} represents the free-space dyadic Green's function which relates the magnetic field to a magnetic source.

3.1.2 Approximation on the Magnetic Current Distribution

Unlike the case of aligned layers that has been studied in [15], the periodic cell is now a combination of two layers rather than one, thus the magnetic current \mathbf{m}_0 cannot be related to \mathbf{m}_{-1} using Floquet boundary conditions. However, to simplify the formulation and enable a closed-form solution for the equivalent layer reactance, an assumption is made, stating that the magnetic currents on the two layers are approximately equal in amplitude and differ only from a spatial displacement and a phase term:

$$\mathbf{m}_{-1}(\boldsymbol{\rho}') \approx \mathbf{m}_0(\boldsymbol{\rho}' - \mathbf{s}) e^{-j\mathbf{k}_{ps} \cdot \mathbf{s}} e^{-jk_{zs} d_z} \quad (3.4)$$

where $\mathbf{s} = s_x\hat{\mathbf{x}} + s_y\hat{\mathbf{y}}$ is the vector indicating the shift and $\mathbf{k}_{ps} = k_{xs}\hat{\mathbf{x}} + k_{ys}\hat{\mathbf{y}}$ is an unknown wave vector describing the transverse propagation between adjacent layers.

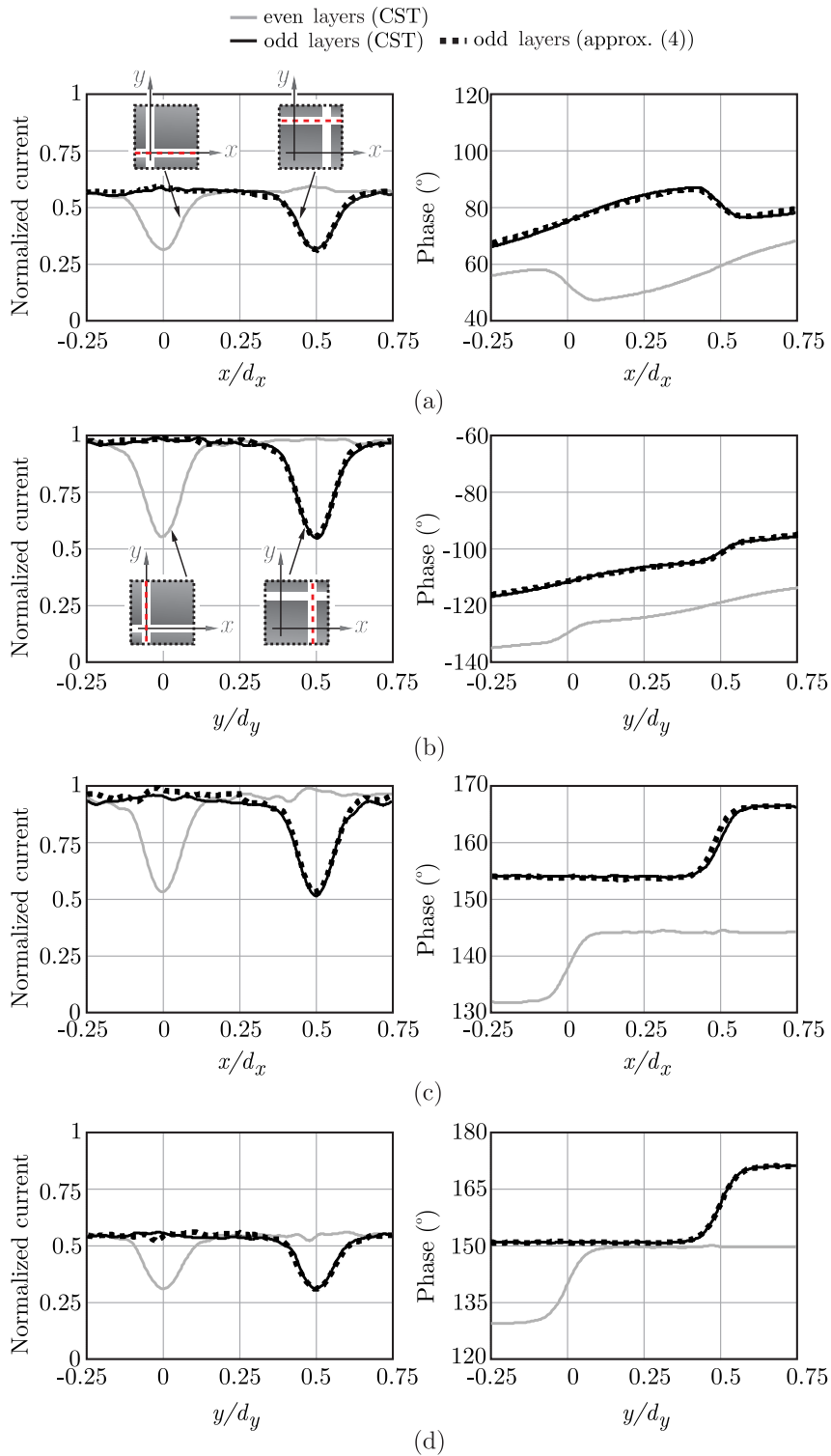


Figure 3.6: Normalized magnetic current distribution on the two orthogonal slot axes (red dashed line in the inset), comparing CST with our approximation in (3.4): TE incidence along (a) x -axis and (b) y -axis slots, and TM incidence along (c) x -axis slot and (d) y -axis slot. The dimensions of the ADLS are $d_x = d_y = 0.0785\lambda_0$, $w_x = w_y = 0.01\lambda_0$, $d_z = 0.012\lambda_0$, $s_x = s_y = 0.5d_x$, with λ_0 being the wavelength at the calculation frequency. All figures refer to plane-wave incidence at $\theta = 60^\circ$ and $\phi = 60^\circ$.

The approximation in (3.4) is equivalent to implying that the the field propagation from one layer to the next is dominated by a lossless guided phenomenon. To assess the error given by this assumption, a

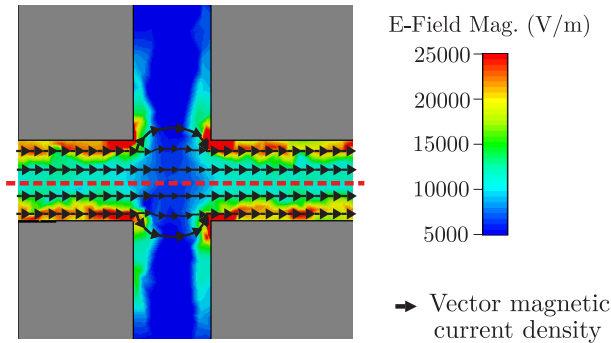


Figure 3.7: Vector magnetic current density and electric field magnitude in correspondence of the junction, obtained with CST. The electric-field magnitude (proportional to the magnetic current) drops in the junction due to the widening of the magnetic current.

simulation using CST [22] is performed. The simulation is as as described in figure 3.5: a semi-infinite cascade of layers is replicated by considering a lossy section of ADLs that implements a low-reflection boundary condition for the transmitted wave.

Figure 3.6 shows the normalized magnitude and the phase of the magnetic current on the two orthogonal slots (gaps between patches) on different layers. The magnetic current is observed in the slots' axes, indicated by the dashed red lines in the inset of figure 3.6(a) and 3.6(b). The geometrical parameters are set as $d_x = d_y = 0.0785\lambda_0$, $w_x = w_y = 0.01\lambda_0$, $d_z = 0.012\lambda_0$, $s_x = s_y = 0.5d_x$, with λ_0 being the wavelength at calculation frequency. Transverse electric (TE) and transverse magnetic (TM) plane-wave illuminations from $\theta = 60^\circ$ and $\phi = 60^\circ$ are considered. For all considered cases, it can be observed from Fig. 3.6 that the approximation (3.4) reproduces well the real current distribution on the odd layers.

The value of k_{zs} to be used in (3.4) was derived from the simulated phase shift between the currents on two consecutive odd layers ($\Delta\phi$), which according to (3.2) is equal to $(2k_{zs}d_z)$. The propagation constants $k_x s$ and $k_y s$ in (3.4) are instead selected as the one of the incident plane wave in the ADL host medium, i.e. $k_0 \sin\theta \cos\phi$ and $k_0 \sin\theta \sin\phi$, respectively.

The amplitude drops of the magnetic current that can be observed in figure 3.6 in correspondence of the junctions are due to the fact that we are plotting the current only on the slot axis, while the transverse distribution widens in the junction. This effect can be observed in figure 3.7, where the vector magnetic current and the magnitude of the electric field simulated with CST are presented.

Under the approximation in (3.4), and assuming that the distance d_z between layers is electrically small so that $e^{\pm jk_{zs}d_z} \approx 1 \pm jk_{zs}d_z$, the integral equation in (3.3) becomes, after a few algebraic steps

$$\begin{aligned} \sum_{n_z \text{ even}} \int_{-\infty}^{\infty} \int_{-\infty}^{\infty} 4\mathbf{m}_0(\boldsymbol{\rho}') \mathbf{g}(\boldsymbol{\rho} - \boldsymbol{\rho}', n_z d_z, z=0) d\boldsymbol{\rho}' = \\ \sum_{n_z \text{ odd}} \int_{-\infty}^{\infty} \int_{-\infty}^{\infty} 4\mathbf{m}_0(\boldsymbol{\rho}' - \mathbf{s}) e^{-jk_{ps} \cdot \mathbf{s}} \mathbf{g}(\boldsymbol{\rho} - \boldsymbol{\rho}', n_z d_z, z=0) d\boldsymbol{\rho}'. \end{aligned} \quad (3.5)$$

3.2 Solution of the Integral Equation and Equivalent Circuit

The approximated integral equation in (3.5) is written only in terms of the unknown magnetic current distribution on the layer $n_z = 0$. This condition allows to solve the equation with a procedure similar to the one described in [14, 15] that has been elaborated in the previous section.

The current is expanded with four entire-domain basis functions, similar to the one that is described in single layer problem (equation (2.7) and (2.8)). It must be noted that while the choice of doing expansion with four entire-domain basis functions in single layer is done just to ensure the consistency of the method used throughout this thesis, this is mandatory for multilayer case (even when the layers are aligned) due to the presence of z -components of the electric fields that is propagating between adjacent layers that is present in this structure.

For deriving an equivalent model that describes the scattering of a plane wave impinging on the ADL structure, the admittance and the forcing terms are again evaluated in the spectral domain, as described in Appendix A.

To enable analytical solutions, we consider low-frequency regime, for which the ADL period is small compared to the wavelength, and we assume that the geometrical parameters are the same along x and y ($s_x = s_y = s$, $d_x = d_y = d$, $w_x = w_y = w$). The latter assumption refers to geometries with azimuthal invariance (scattering of a plane wave is independent of ϕ), in which TE and TM modes are decoupled, derived from single layer problem. More general geometries can be still analyzed with the formalism, but they result in more complex equivalent networks that couple TE and TM modes.

Under the condition $s_x = s_y$, it can be demonstrated Appendix A that the system of linear equations is reduced to the following simpler problem

$$\overline{\overline{\mathbf{Y}}}_{\text{TETM}} \overline{\mathbf{a}}_{\text{TETM}} = 0 \quad (3.6)$$

where

$$\overline{\mathbf{a}}_{\text{TETM}} = \begin{pmatrix} a_1 \cos\phi + a_2 \sin\phi \\ -a_1 \sin\phi + a_2 \cos\phi \end{pmatrix} \quad (3.7)$$

$$\overline{\mathbf{i}}_{\text{TETM}} = \begin{pmatrix} i_1 \cos\phi + i_2 \sin\phi \\ -i_1 \sin\phi + i_2 \cos\phi \end{pmatrix} \quad (3.8)$$

and the admittance matrix $\overline{\overline{\mathbf{Y}}}_{\text{TETM}}$ is a 2×2 diagonal matrix that can be split in two contributions, as shown in equation (A.18) in Appendix A. One contribution represents the propagation of the plane wave (fundamental Floquet wave), whereas the second term is the equivalent admittance of one layer of the ADL and can be approximated as

$$\overline{\overline{\mathbf{Y}}}_{\text{ADL}} \approx \begin{bmatrix} jB_\infty(1 - \frac{\sin^2\theta}{2}) & 0 \\ 0 & jB_\infty \end{bmatrix} \quad (3.9)$$

The equivalent layer susceptance in the presence of the shift is given by:

$$B_\infty \approx \frac{jk_0 d}{\zeta_0 \pi} \sum_{m \neq 0} \frac{|\text{sinc}(\pi m \frac{w}{d})|^2}{|m|} \cdot \left(-\cot(-j2\pi|m|\frac{d_z}{d}) + e^{j2\pi m \frac{s}{d}} \csc(-j2\pi|m|\frac{d_z}{d}) \right) \quad (3.10)$$

where m are the indexes of the Floquet modes. The analytical expression in (3.10) accounts for the higher-order coupling between layers and thus remains valid even for inter-layer distances much smaller than the wavelength. It can be noted that the formula remains valid also for the aligned case $s_x = s_y = 0$ and thus is general.

While (3.10) is derived for an infinite number of layer, also the semi-infinite case is relevant to describe the effect of truncation in a finite cascade of layers. It is shown in the [38] that while the result only with infinite cascade of ADL shows the fair agreement, accounting the effect of truncation in height of ADL improves the result further. The semi-infinite elements are describes as the first and the last layer on the ADL slab. The susceptance of the first layer in a semi-infinite cascade is given by

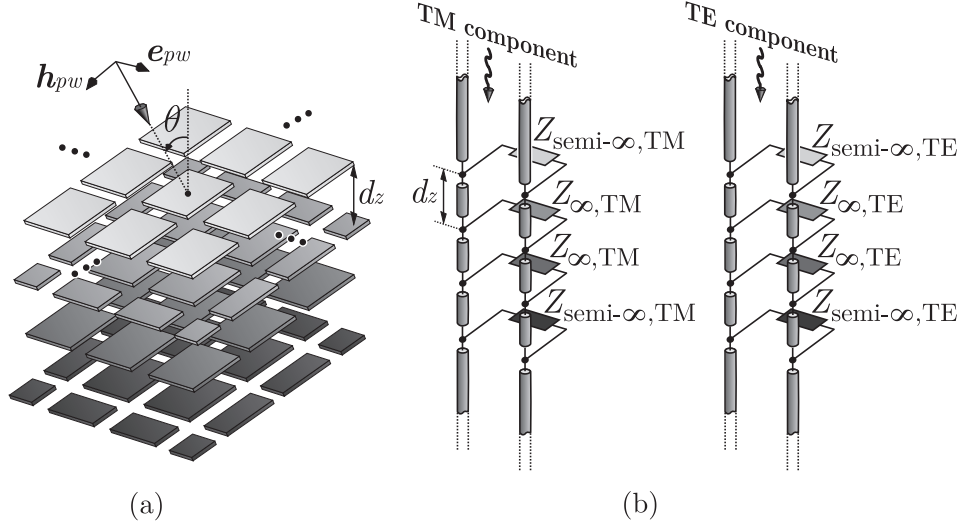


Figure 3.8: (a) Plane wave impinging on a cascade of four ADLs with alternate shifts and (b) equivalent circuits for TE and TM components.

$$B_{\text{semi-}\infty} \approx \frac{jk_0 d}{2\zeta_0 \pi} \sum_{m \neq 0} \frac{|\text{sinc}(\pi m \frac{w}{d})|^2}{|m|} \cdot \left(-j - \cot(-j2\pi|m|\frac{d_z}{d}) + e^{j2\pi m \frac{s}{d}} \csc(-j2\pi|m|\frac{d_z}{d}) \right) \quad (3.11)$$

Comparing these susceptance terms for ADL to the one in single layer (equation (2.18)), it can be deduced that the terms are related. The susceptance in ADL can be split into the reactance of single layer term, B_s , and the inter-layer reactive coupling term. The later term is related to the closed-form solutions for the infinite and semi-infinite sums of the layers in Appendix B. Thus, equation (3.10) and (3.11) can be written compactly as

$$B_{\infty} \approx B_s \cdot S_{\infty}, \quad B_{\text{semi-}\infty} \approx B_s \cdot S_{\text{semi-}\infty} \quad (3.12)$$

where the inter-layer reactive coupling terms are given by

$$S_{\infty} = -\cot(-j2\pi|m|\frac{d_z}{d}) + e^{j2\pi m \frac{s}{d}} \csc(-j2\pi|m|\frac{d_z}{d}) \quad (3.13)$$

$$S_{\text{semi-}\infty} = \frac{1}{2} \left(-j - \cot(-j2\pi|m|\frac{d_z}{d}) + e^{j2\pi m \frac{s}{d}} \csc(-j2\pi|m|\frac{d_z}{d}) \right). \quad (3.14)$$

3.2.1 Equivalent Transmission-Line Model

From equation (3.6), one can express the reactance of a layer embedded in a periodic multi-layer environment as follows:

$$\begin{aligned} Z_{\infty, \text{TM}} &= \frac{-j}{B_{\infty}}, & Z_{\infty, \text{TE}} &= \frac{-j}{B_{\infty}(1 - \frac{\sin^2 \theta}{2})} \\ Z_{\text{semi-}\infty, \text{TM}} &= \frac{-j}{B_{\text{semi-}\infty}}, & Z_{\text{semi-}\infty, \text{TE}} &= \frac{-j}{B_{\text{semi-}\infty}(1 - \frac{\sin^2 \theta}{2})}. \end{aligned} \quad (3.15)$$

These values of the equivalent reactance can be incorporated in an equivalent circuit that describes the propagation of a generic plane wave in the ADL medium illustrated in Fig. 3.8(a). The equivalent

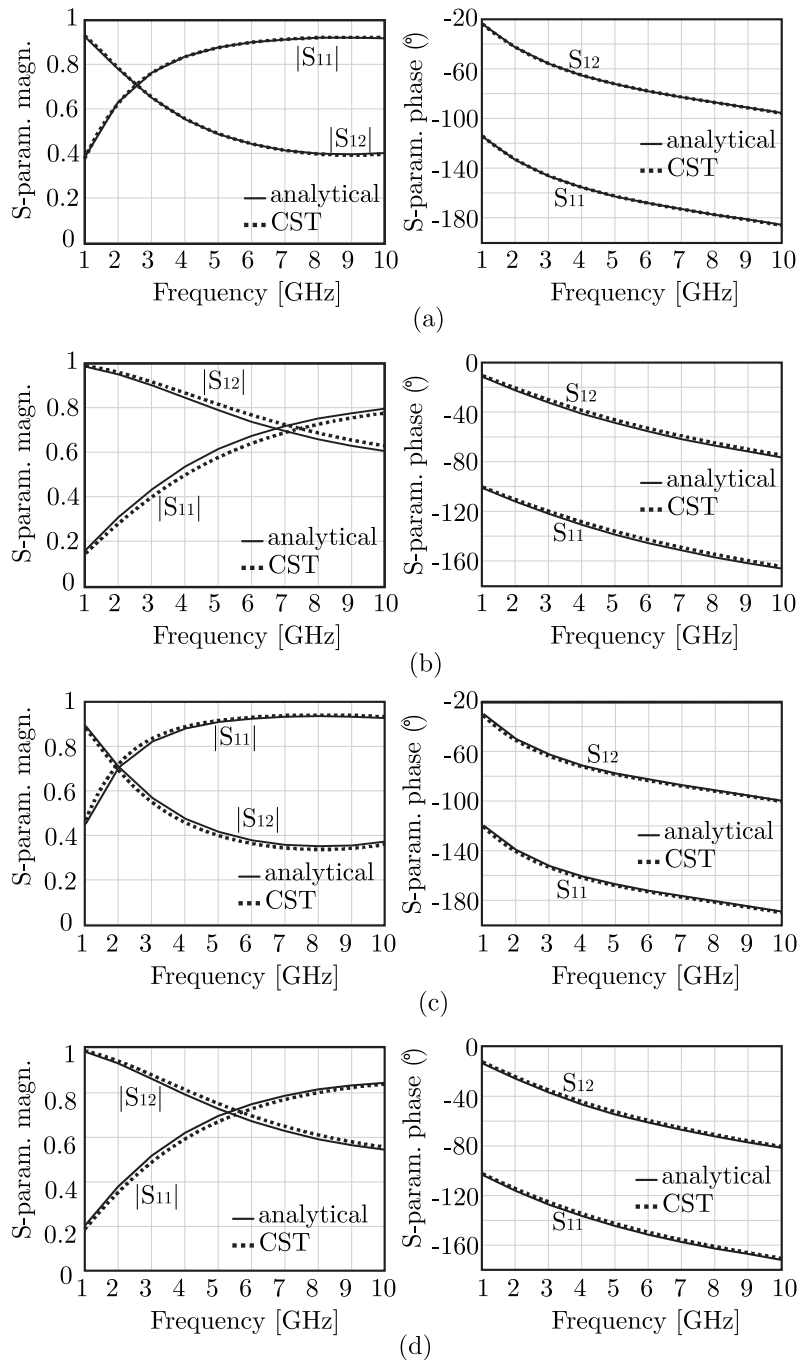


Figure 3.9: Amplitude and phase of the reflection and transmission coefficients of a plane wave incident on a cascade of 5 layers: (a) TE, $\theta = 60^\circ$, $s_{x,y} = 0.25d_{x,y}$; (b) TM, $\theta = 60^\circ$, $s_{x,y} = 0.25d_{x,y}$; (c) TE, $\theta = 60^\circ$, $s_{x,y} = 0.5d_{x,y}$; (d) TM, $\theta = 60^\circ$, $s_{x,y} = 0.5d_{x,y}$. The geometrical parameters are $d_x = d_y = 0.0785\lambda_0$, $w_x = w_y = 0.01\lambda_0$, $d_z = 0.012\lambda_0$, with λ_0 being the wavelength at 5 GHz.

transmission lines are shown in Fig. 3.8(b) for the TE and TM components. The infinite solution is used to represent the inner layers, whereas the semi-infinite formula is employed to characterize the edge layers, to account for the truncation.

To validate the formulas and assess the accuracy of the approximations, we show in Fig. 3.9 the reflection and transmission coefficients for TE and TM plane-wave incidence (at $\theta = 60^\circ$) and for different shifts. CST [22] simulations are also reported for the same structures and show good agreement with our method.

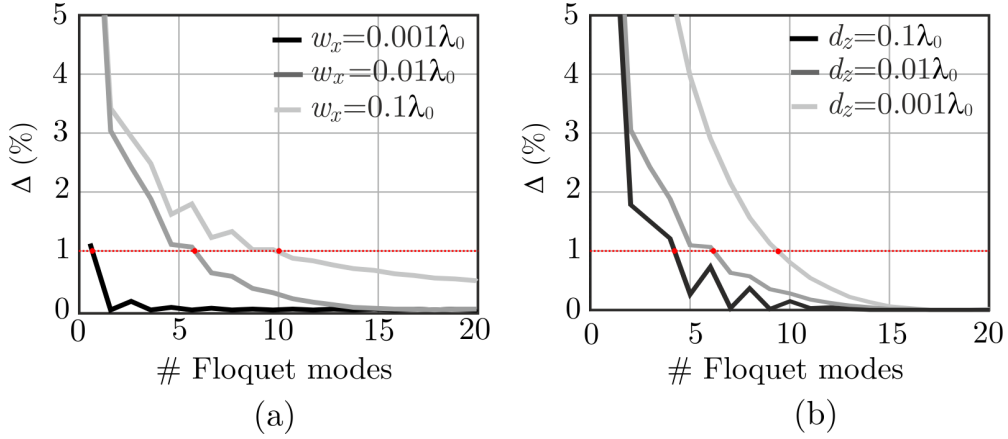


Figure 3.10: Convergence characteristics, defined as in (3.16), of the susceptance B_∞ as a function of the number of Floquet modes: (a) $d_z = 0.01\lambda_0$ and three values of $w_x = w_y$ are considered; (b) $w_x, w_y = 0.01\lambda_0$ and three values of d_z are considered. The other parameters are $d_x = d_y = 0.2\lambda_0$ and $s_x = s_y = 0.45d_x$.

3.2.2 Convergence of the Floquet Sums

The sums in equation (3.10) and (3.11) contain an infinite number of terms. In practice, these sums are truncated to a finite number of Floquet modes $m \in [-M, -M+1, \dots, -1, 1, 2, \dots, M]$. To assess the convergence properties a relative difference between partial sums is defined as follows:

$$\Delta = \frac{|B_\infty(M) - B_\infty(M-1)|}{|B_\infty(M)|} \quad (3.16)$$

where $B_\infty(M)$ represents the expression in (3.10) with the Floquet sum truncated from $-M$ to M modes. This convergence parameter of the susceptance B_∞ is shown in Fig. 3.10, for different geometrical parameters, as a function of the number of Floquet modes. It can be noted that the convergence is slower for small w_x , while smaller d_z lead actually to faster convergence. Despite the differences, all cases show rapid convergence for realistic design parameters, resulting in $\Delta < 1\%$ with only 10 modes or less.

3.3 Problem Definition and Formulation for ADLs with Finite Conductivity

Following the same propositions that are described in chapter 2 about the losses introduced by the finite conductivity of the patches, the analysis of the finite cascade of layer is also extended to the lossy metal case. This allows to quantify analytically the losses even at the early stages the design process.

To start the formulation, an ADL composed of an infinite number of layers is considered as illustrated in Fig. 3.11(a) where the patches have a finite conductivity. Three surfaces denoted with S_{-1} , S_0 , and S_1 , are defined as in the Fig. 3.11, and, following an alternative formulation of the equivalence theorem, are filled with metal with the same conductivity. This ensures the homogeneity of the metal plates across their surfaces. As shown in the lossy single layer section in chapter 2, the original problem can be represented as magnetic current, $\mathbf{m}_{n_z}(x, y)$, with subscripts that describes the position of layer, radiating in the presence of infinite metal planes with finite conductivity σ . These metal layers exist on the top and below the current density, creating structure similar to parallel plane waveguide (PPW) structures.

Imposing the Floquet boundary condition due to the periodicity along z and the approximation of the magnetic current distribution, relating the currents on the odd and even layers, the integral equation for

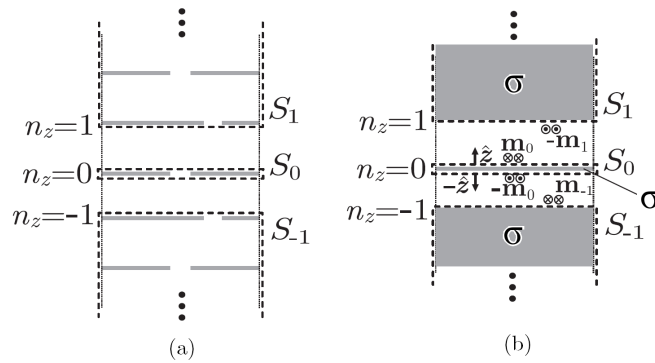


Figure 3.11: (a) original problem and (b) equivalent problem with unknown magnetic current distributions.

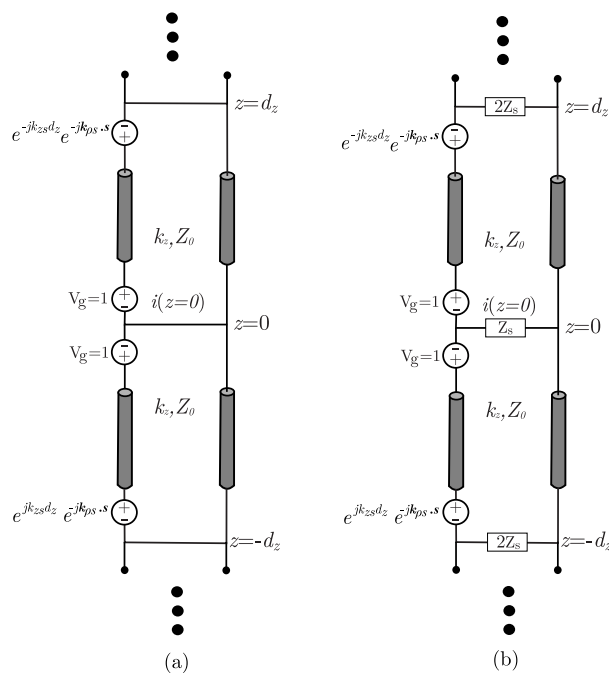


Figure 3.12: Equivalent representation of the ADLs' unit cell: (a) the lossless case, (b) the lossy case.

the magnetic field at $z = 0$ can be written as

$$\int_{-\infty-\infty}^{\infty} \int_{-\infty}^{\infty} 2\mathbf{m}_0(\boldsymbol{\rho}') \mathbf{g}_{\text{ppw}}(\boldsymbol{\rho} - \boldsymbol{\rho}', n_z d_z, z=0) d\boldsymbol{\rho}' = \int_{-\infty-\infty}^{\infty} \int_{-\infty}^{\infty} 2\mathbf{m}_0(\boldsymbol{\rho}' - \mathbf{s}) e^{-jk_{ps} \cdot \mathbf{s}} \mathbf{g}_{\text{ppw}}(\boldsymbol{\rho} - \boldsymbol{\rho}', n_z d_z, z=0) d\boldsymbol{\rho}' \quad (3.17)$$

where $\boldsymbol{\rho} = x\hat{\mathbf{x}} + y\hat{\mathbf{y}}$ and $\boldsymbol{\rho}' = x'\hat{\mathbf{x}} + y'\hat{\mathbf{y}}$ are the observation and the source points, respectively. The function \mathbf{g}_{ppw} represents the Green's function which relates the magnetic field to a magnetic source radiating within a lossy parallel plate waveguide. Due to the finite conductivity that the metal possesses, the image theorem can not be employed. However, this representation still allows solving the integral equation in the same way as the lossless case, only changing the Green's function.

3.3.1 Green's Function Representation for the Problem

The Green's function in equation (3.17) can be expressed in the spectral domain by solving for the current at layer $z = 0$ of equivalent TE and TM unit cell transmission lines representing the stratified

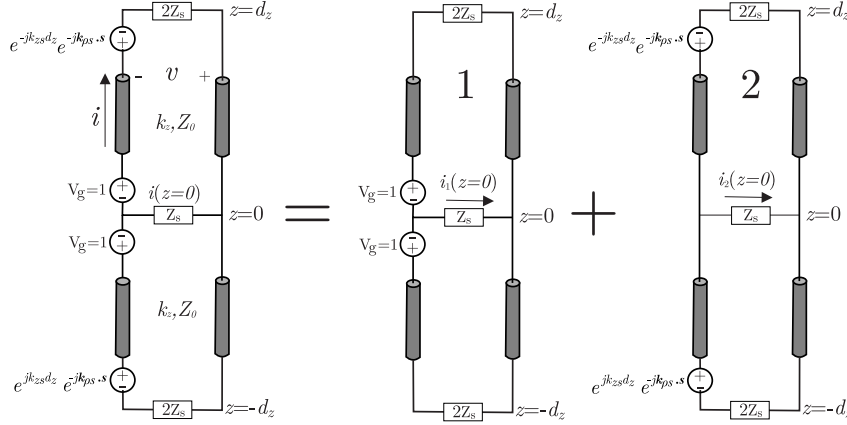


Figure 3.13: Equivalent transmission line to the unit cell and depiction of the superposition circuit theorem

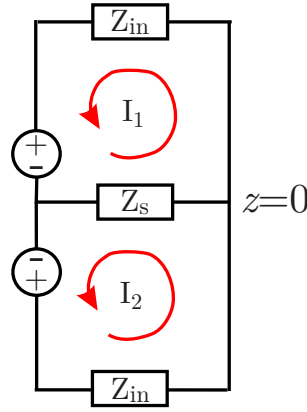


Figure 3.14: Equivalent circuit for transmission line marked as 1 in figure 3.13.

medium. The unit cell, shown in Fig. 3.12, represents the admittance matrix $\overline{\overline{\mathbf{Y}}}_{\text{TETM}}$ which consists of the contribution of the propagation of the plane wave and the equivalent admittance of the ADL. The magnetic current densities are represented as voltage generators. In the layer $z = 0$, the voltage generator is equal to 1V. The generators placed in $z = d_z$ and $z = -d_z$ are assumed to be equal in amplitude and differ only in phase with generator at $z = 0$. The phase difference comes from a spatial displacement $e^{-jk_{ps} \cdot s}$ and a phase term $e^{\mp jk_{zs} d_z}$. The vector $\mathbf{s} = s_x \hat{\mathbf{x}} + s_y \hat{\mathbf{y}}$ is indicating the shift and $\mathbf{k}_{ps} = k_{xs} \hat{\mathbf{x}} + k_{ys} \hat{\mathbf{y}}$ is an unknown wave vector describing the transverse propagation between adjacent layers.

For the lossless case (Fig. 3.12(a)), the layer is represented by a short circuit. Thus, the problem unravels to magnetic currents radiating within PEC parallel plate waveguide, which would give the same results as when image theorem is applied and the currents and their images are radiating in free space.

In the other hand, for the lossy case (Fig. 3.12(b)), each layers has surface impedance Z_s that is depicting the finite conductivity of the layer. It is to be noted that at $z = d_z$ and $z = -d_z$, the impedance is defined as twice of the layer's impedance, $2Z_s$. This is due to the fact that at the edge of the unit cell, only half of the current is considered and half of the current translates to twice of the impedance. Thus later when this unit cell is cascaded, the total current is equal to the current in the layer.

To solve the transmission lines, superposition theorem is used. Due to the superposition theorem in circuit, it is possible to separate transmission line depicted in Fig. 3.13 into two transmission lines (marked with '1' and '2') where each of them has two voltage generators. Furthermore, the transmission line marked as 1 in Fig. 3.13 can be represented as Fig. 3.14 where Z_{in} is the input impedance seen from

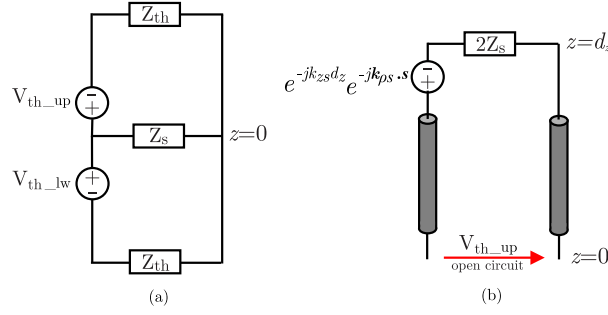


Figure 3.15: (a) The equivalent Thévenin's circuit equal to transmission line marked as 2 in figure 3.13. (b) Definition of the Thévenin's equivalent circuit voltage generator for the problem.

$z = 0$. Solving the circuit depicted in Fig. 3.14 (detailed in Appendix C) gives

$$i_1(z=0) = \frac{2}{2Z_s + Z_{in}} \quad (3.18)$$

where

$$Z_{in} = Z_0 \frac{2Z_s + jZ_0 \tan(k_z d_z)}{Z_0 + j2Z_s \tan(k_z d_z)}. \quad (3.19)$$

Transmission line marked as 2 in Fig. 3.13 can be solved by applying Thévenin's theorem. It is illustrated in Fig. 3.15(a) that the transmission line is represented as a circuit similar to Fig. 3.14 but with Thévenin's equivalent circuit impedance and voltage generator. Fig. 3.15(b) shows the relation of the original circuit and its Thévenin's equivalent circuit voltage generator.

Solving the aforementioned circuit to find the current at $z = 0$ (detailed in Appendix C) will result in:

$$i_2(z=0) = -\frac{2}{2Z_s + Z_{in}} \frac{-jZ_0 \csc(k_z d_z)}{-jZ_0 \cot(k_z d_z) + 2Z_s} e^{-jk_{ps} \cdot s}. \quad (3.20)$$

The total current that flows at $z = 0$ at the original problem (figure 3.13) can be seen as an addition of currents that are given by equation (3.18) and (3.20) which is

$$i(z=0) = \frac{2}{2Z_s + Z_{in}} - \frac{2}{2Z_s + Z_{in}} \frac{-jZ_0 \csc(k_z d_z)}{-jZ_0 \cot(k_z d_z) + 2Z_s} e^{-jk_{ps} \cdot s}. \quad (3.21)$$

It can be proved (detailed in Appendix C) that equation (3.21) simplifies to:

$$i(z=0) = \frac{2S}{Z_0 + 2Z_s S}, \quad (3.22)$$

where S is the inter-layer reactive coupling identical to the lossless ADL case (equation (3.13)).

This current given in equation (3.22) is the current that is needed to be plugged into the Green's Function to find the field by the current density.

3.4 Solution and the Equivalent Reactance of ADLs with Finite Conductivity

Once the Green's function is defined, the rest of the steps to solve the unknowns are identical to the lossless case. Different terms of reactance and impedance for the ADL layers are derived to take into account the conductivity of the metal patches. Similar to the single layer case, the equivalent reactance of the layer, for each mode, is given by:

$$\begin{aligned} Z_{\infty\text{layer,TE}} &= Z_{\infty,TE} + Z_s, & Z_{\infty\text{layer,TM}} &= Z_{\infty,TM} + Z_s \\ Z_{\text{semi-}\infty\text{layer,TE}} &= Z_{\text{semi-}\infty,TE} + Z_s, & Z_{\text{semi-}\infty\text{layer,TM}} &= Z_{\text{semi-}\infty,TM} + Z_s \end{aligned} \quad (3.23)$$

where

$$\begin{aligned} Z_{\infty,TE} &= \frac{1}{Y_{\infty,TE}}, & Z_{\infty,TM} &= \frac{1}{Y_{\infty,TM}} \\ Z_{\text{semi-}\infty,TE} &= \frac{1}{Y_{\text{semi-}\infty,TE}}, & Z_{\text{semi-}\infty,TM} &= \frac{1}{Y_{\text{semi-}\infty,TM}} \end{aligned} \quad (3.24)$$

with the admittances of the layer separated into infinite and semi-infinite terms to account for the middle layers and the layers at the edges. Accounting for the truncation improves the accuracy of the analytical solutions. The layer admittance terms are also defined for both the TE and TM modes. Analogous to the lossy single layer, the admittance of the layer is not a pure susceptance term.

The admittance of a layer embedded in a periodic multi-layer environment can be written as

$$\begin{aligned} Y_{\infty,TE} &\approx -2j \sum_{m_y \neq 0} \left| \text{sinc}\left(k_{ym} \frac{w_y}{2}\right) \right|^2 \\ &\quad \left(\frac{k_{x0}^2}{2k_{\rho m}^2} \left(\zeta_0 \frac{k_0}{k_{zm}} + 2Z_s S_{\infty} \right)^{-1} + \frac{k_{ym}^2}{k_{\rho m}^2} \left(\zeta_0 \frac{k_{zm}}{k_0} + 2Z_s S_{\infty} \right)^{-1} \right) S_{\infty} \\ Y_{\infty,TM} &\approx -2j \sum_{m_x \neq 0} \left| \text{sinc}\left(k_{xm} \frac{w_x}{2}\right) \right|^2 \\ &\quad \left(\frac{k_{y0}^2}{k_{\rho m}^2} \left(\zeta_0 \frac{k_0}{k_{zm}} + 2Z_s S_{\infty} \right)^{-1} + \frac{k_{xm}^2}{k_{\rho m}^2} \left(\zeta_0 \frac{k_{zm}}{k_0} + 2Z_s S_{\infty} \right)^{-1} \right) S_{\infty} \end{aligned} \quad (3.25)$$

and the admittance for the layer placed at the edge (last and first layer) is

$$\begin{aligned} Y_{\text{semi-}\infty,TE} &\approx -2j \sum_{m_y \neq 0} \left| \text{sinc}\left(k_{ym} \frac{w_y}{2}\right) \right|^2 \\ &\quad \left(\frac{k_{x0}^2}{2k_{\rho m}^2} \left(\zeta_0 \frac{k_0}{k_{zm}} + 2Z_s S_{\text{semi-}\infty} \right)^{-1} + \frac{k_{ym}^2}{k_{\rho m}^2} \left(\zeta_0 \frac{k_{zm}}{k_0} + 2Z_s S_{\text{semi-}\infty} \right)^{-1} \right) S_{\text{semi-}\infty} \\ Y_{\text{semi-}\infty,TM} &\approx -2j \sum_{m_x \neq 0} \left| \text{sinc}\left(k_{xm} \frac{w_x}{2}\right) \right|^2 \\ &\quad \left(\frac{k_{y0}^2}{k_{\rho m}^2} \left(\zeta_0 \frac{k_0}{k_{zm}} + 2Z_s S_{\text{semi-}\infty} \right)^{-1} + \frac{k_{xm}^2}{k_{\rho m}^2} \left(\zeta_0 \frac{k_{zm}}{k_0} + 2Z_s S_{\text{semi-}\infty} \right)^{-1} \right) S_{\text{semi-}\infty} \end{aligned} \quad (3.26)$$

where m_x and m_y are the indexes of the Floquet modes, $k_{xm} = k_{x0} - 2\pi m_x/d_x$ and $k_{ym} = k_{y0} - 2\pi m_y/d_y$ are the Floquet wavenumbers which determine $k_{zm} = \sqrt{k_0^2 - k_{xm}^2 - k_{ym}^2}$ and $k_{\rho m} = \sqrt{k_{xm}^2 + k_{ym}^2}$. The propagation constants along x , y , and z are $k_{x0} = k_0 \sin\theta \cos\phi$, $k_{y0} = k_0 \sin\theta \sin\phi$, and $k_{z0} = k_0 \cos\theta$, where k_0 is the free-space wavenumber. The terms S_{∞} and $S_{\text{semi-}\infty}$ are the terms defined in (3.13) and (3.14).

Figure 3.16 shows the equivalent circuit representation of the impedance, including the Z_s contribution. Similar to the case in single layer of periodic patches, the finite conductivity introduces an impedance term (Z_s) that is in series with the layer impedance. This representation also described the lossless case, for which the impedance Z_s is zero and equal to a short circuit. Moreover, the resistance of the layer is not only represented by the series load Z_s , but an additional resistive contribution also occurs in the terms Z_{∞} and $Z_{\text{semi-}\infty}$, which are complex.

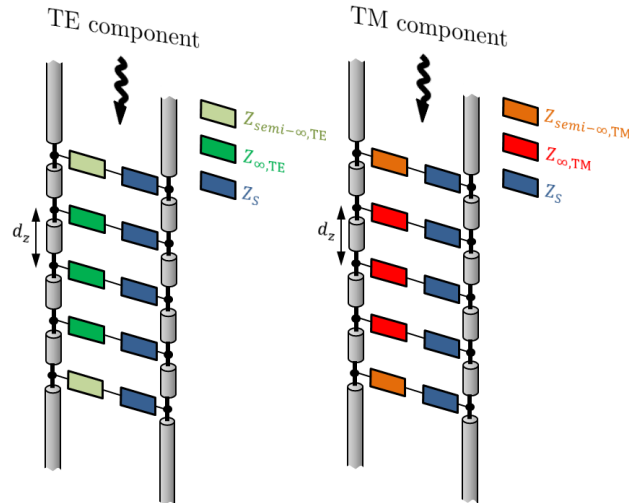


Figure 3.16: Equivalent circuit representation of the ADL composed of 5 layers with finite conductivity for TE and TM component.

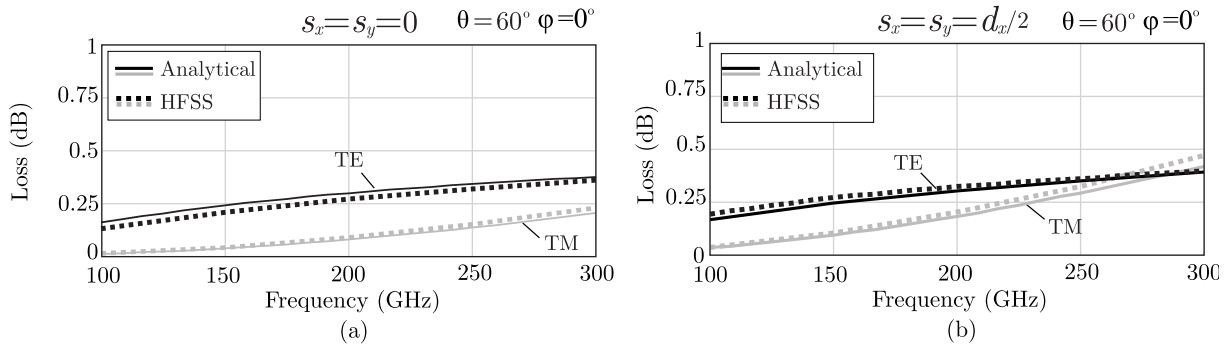


Figure 3.17: Comparing loss (in dB) calculated based on analytical solution and HFSS simulation. The plane wave incident on an ADL with finite conductivity ($\sigma = 1000$ S/m) with angle of incidence $\theta = 60^\circ$, $\phi = 0^\circ$. The geometrical parameters of layer of patches are $d_x = d_y = 0.095\lambda_0$, $w_x = w_y = 0.01\lambda_0$, $d_z = 0.02\lambda_0$, and shift (a) $s_x = s_y = 0$ (aligned); (b) $s_x = s_y = d_x/2$, with λ_0 being the wavelength at 300 GHz.

Full-wave HFSS [39] simulations are made to validate the analytical solution. An extreme case with $\sigma = 1000$ S/m is taken due to the low losses that the structure exhibits. The single layer of patches geometrical parameters are $d_x = d_y = 0.095\lambda_0$, $w_x = w_y = 0.01\lambda_0$, and $d_z = 0.02\lambda_0$, with λ_0 being the wavelength at 300 GHz. The incident plane wave is coming from oblique angle ($\theta = 60^\circ \phi = 0^\circ$). An aligned and shifted case are considered.

In Fig. 3.17 and Fig. 3.18, the comparison between analytical solution and simulation result are shown. A good agreement of the scattering parameters can be seen for the cases investigated. Moreover, the shift does not introduce significant increase of losses. It is worth to mention that the loss for TE incidence shown in Fig. 3.17 appear not to increase with the frequency as the TM case. This observation can be explained with the fact that the transmission coefficient for the TE case decreases significantly as the frequency grows, as shown in Fig. 3.18. The low transmission signifies that most of the incident wave is reflected at the interface between the air and the ADL, thus interacts less with the lossy metal patches. Figure 3.19 shows the example of case where the ADL is designed so the total height of the slab becomes near resonant at certain frequency. This is done in order to showcase that the transmission coefficient has an effect on the losses. It can be seen from Fig. 3.19(a) that at 220 GHz, the reflection

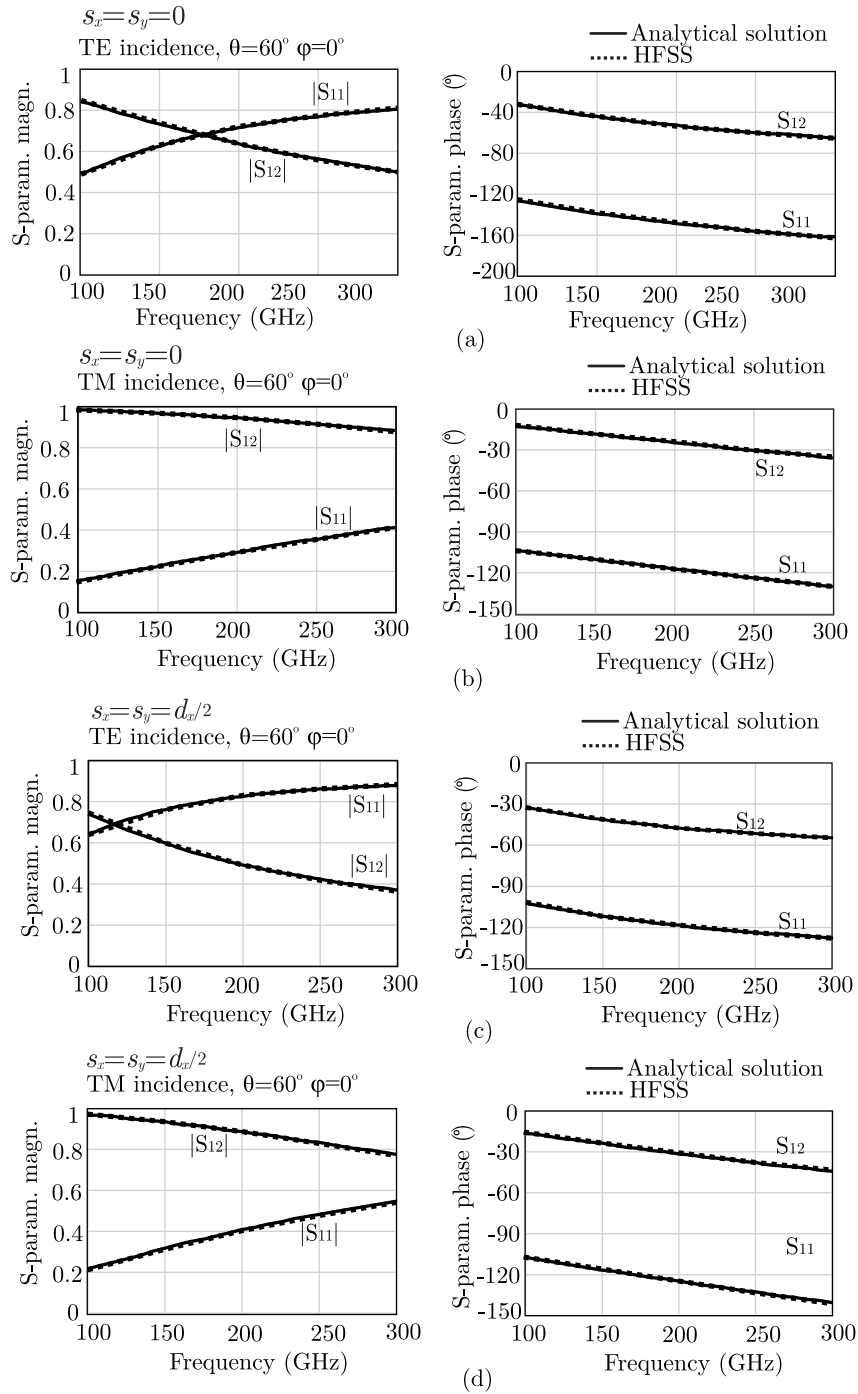


Figure 3.18: Comparison between analytical solution and HFSS simulation of amplitude and phase of the reflection and transmission coefficients of a plane wave incident on a single layer of patches with finite conductivity ($\sigma = 1000S/m$), with angle of incidence $\theta = 60^\circ$, $\phi = 0^\circ$ (a) TE incidence $s_x = s_y = 0$ (aligned) (b) TM incidence $s_x = s_y = 0$ (aligned), (c) TE incidence $s_x = s_y = d_x/2$ (d) TM incidence $s_x = s_y = d_x/2$. The geometrical parameters are $d_x = d_y = 0.095\lambda_0$, $w_x = w_y = 0.01\lambda_0$, and $d_z = 0.02\lambda_0$, with λ_0 being the wavelength at 300 GHz.

coefficient is near zero, thus the transmission coefficient is close to 1. At the same point, the losses, depicted in Fig. 3.19(b), is at the highest.

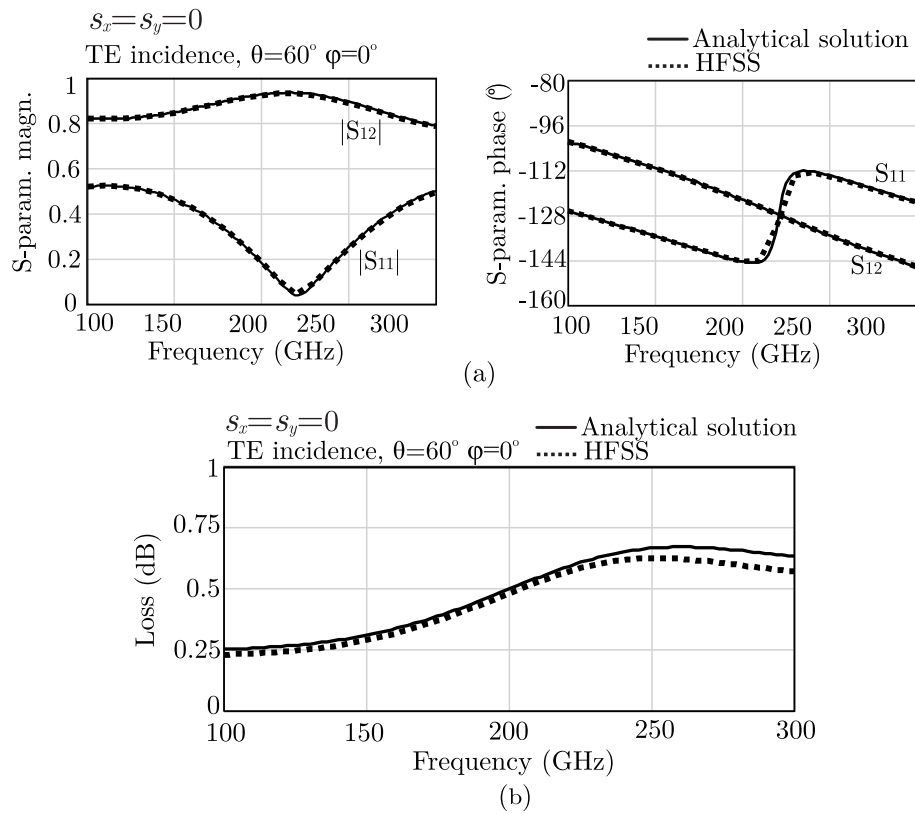


Figure 3.19: (a) Scattering parameters magnitude and phase, and (b) losses in dB for a TE incidence impinging on a 5 layers aligned-ADL with finite conductivity ($\sigma = 10^6$ S/m) with angle of incidence $\theta = 60^\circ$, $\phi = 0^\circ$. The geometrical parameters of layer of patches are $d_x = d_y = 0.095\lambda_0$, $w_x = w_y = 0.01\lambda_0$, $d_z = 0.15\lambda_0$, with λ_0 being the wavelength at 300 GHz.

Chapter 4

Effective Parameters and Tolerance Study of ADL

4.1 Attaining Effective Permittivity and Permeability

Artificial dielectric layer (ADL) synthesizes an equivalent material that can be represented with its effective parameters, i.e. permittivity and permeability. The retrieval of the effective permittivity and permeability is often denoted as homogenization process. Homogenization techniques using the scattering parameters of an incident plane wave from the material are the most commonly used methods and have been reported in several articles [36, 40–45]. This allows to model the ADLs as an equivalent homogenous, anisotropic slab with a finite height.

The AD composed of stacked layers of periodic patches (ADL) is anisotropic because the refractive index is a function of the propagation direction and polarization of the wave. Therefore its effective permittivity and permeability are described by second rank tensors: $\bar{\bar{\epsilon}}$ and $\bar{\bar{\mu}}$

$$\bar{\bar{\epsilon}} = \epsilon_0 \begin{pmatrix} \epsilon_x & 0 & 0 \\ 0 & \epsilon_y & 0 \\ 0 & 0 & \epsilon_z \end{pmatrix}, \quad \bar{\bar{\mu}} = \mu_0 \begin{pmatrix} \mu_x & 0 & 0 \\ 0 & \mu_y & 0 \\ 0 & 0 & \mu_z \end{pmatrix}$$

where ϵ_0 and μ_0 are the permeability and permeability of the vacuum, respectively. The unknowns ϵ_x , ϵ_y , ϵ_z , μ_x , μ_y , and μ_z are quantities without dimensions that represent the effective relative permittivity and permeability tensors. The matrices are in general non-diagonal and symmetric, i.e. $\bar{\bar{\epsilon}} = (\bar{\bar{\epsilon}})^T$ and $\bar{\bar{\mu}} = (\bar{\bar{\mu}})^T$ as a consequence of the Maxwell equations. However, a coordinate system exists for which diagonal tensors can be defined. For the geometry under analysis, the Cartesian coordinate system constitutes the principal axes for the elements of the diagonal tensor. For a linear isotropic material, all the diagonal elements have the same value, which implies that such medium is uniform in all directions.

Using the equivalent circuit that is derived for ADL in chapter 3, the scattering parameters under plane wave illumination can be calculated. As elaborated in [46], for any slab with thickness d , (illustrated in Fig. 4.1) the effective parameters can be calculated based on its scattering parameters. This method calls for the scattering parameters that are derived from normal and oblique incidence, for each TE and TM polarization. Applying the method in [46] to the structure that is presented in this thesis, the $\bar{\bar{\epsilon}}$ and $\bar{\bar{\mu}}$ can be formulated as

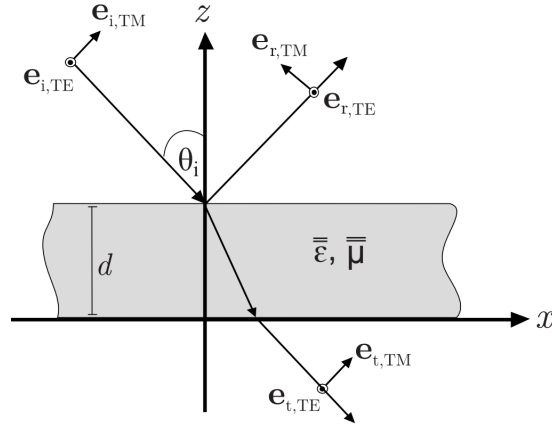


Figure 4.1: Illustration of an anisotropic slab (characterized by $\bar{\epsilon}$ and $\bar{\mu}$) illuminated by electromagnetic field coming from oblique incident angle θ_i .

$$\begin{aligned}\epsilon_x &= \frac{n_{\theta_i=0}^{TM}}{\eta_{\theta_i=0}^{TM}}, & \mu_x &= n_{\theta_i=0}^{TE} \eta_{\theta_i=0}^{TE} \\ \epsilon_y &= \frac{n_{\theta_i=0}^{TE}}{\eta_{\theta_i=0}^{TE}}, & \mu_y &= n_{\theta_i=0}^{TM} \eta_{\theta_i=0}^{TM}\end{aligned}\quad (4.1)$$

$$\epsilon_z = \frac{\epsilon_x \sin^2 \theta_i}{\sin^2 \theta_i - (n^{TM})^2 + (n_{\theta_i=0}^{TM})^2}, \quad \mu_z = \frac{\mu_x \sin^2 \theta_i}{\sin^2 \theta_i - (n^{TE})^2 + (n_{\theta_i=0}^{TE})^2}$$

where the wave impedances η and refraction indices n are evaluated from

$$\begin{aligned}\eta^{TE} &= \pm \sqrt{\frac{(1 + S_{11}^{TE})^2 - (S_{21}^{TE})^2}{(1 - S_{11}^{TE})^2 - (S_{21}^{TE})^2}} \sec \theta_i, & \eta^{TM} &= \pm \sqrt{\frac{(1 + S_{11}^{TM})^2 - (S_{21}^{TM})^2}{(1 - S_{11}^{TM})^2 - (S_{21}^{TM})^2}} \cos \theta_i \\ \zeta_{TE} &= \frac{S_{21}^{TE}}{1 - S_{11}^{TE} (\eta^{TE} \cos \theta_i - 1) / (\eta^{TE} \cos \theta_i + 1)}, & \zeta_{TM} &= \frac{S_{21}^{TM}}{1 - S_{11}^{TM} (\eta^{TM} \cos \theta_i - 1) / (\eta^{TM} \cos \theta_i + 1)} \\ n^{TE} &= \sqrt{\left(\frac{\ln(|\zeta_{TE}|) + j(\angle(\zeta_{TE}))}{-jk_0 d} \right)^2 + \sin^2 \theta_i}, & n^{TM} &= \sqrt{\left(\frac{\ln(|\zeta_{TM}|) + j(\angle(\zeta_{TM}))}{-jk_0 d} \right)^2 + \sin^2 \theta_i}.\end{aligned}\quad (4.2)$$

To validate the method, a CST [22] simulation is established to simulate a non-aligned ADL as shown in Fig. 4.2(a). The ADL is composed of 5 layers of perfectly conducting square patches with $d_x = d_y = 0.0785\lambda_0$, $d_z = 0.012\lambda_0$, $w_x = w_y = 0.01\lambda_0$, $s_x = s_y = 0.5d_x$, with λ_0 being the wavelength at the calculation frequency f_0 . The scattering parameters (normal and oblique incidence) from the simulated geometry are used to calculate its effective parameters, $\bar{\epsilon}$ and $\bar{\mu}$. Another simulation is made to simulate a slab, Fig. 4.2 (b) that is defined as an equivalent anisotropic material with the estimated effective $\bar{\epsilon}$ and $\bar{\mu}$.

The scattering parameters from the slab are then compared to the scattering parameters from the ADL. Note that both structures are illuminated under a plane wave incidence with $\theta = 60^\circ$ and $\phi = 0^\circ$.

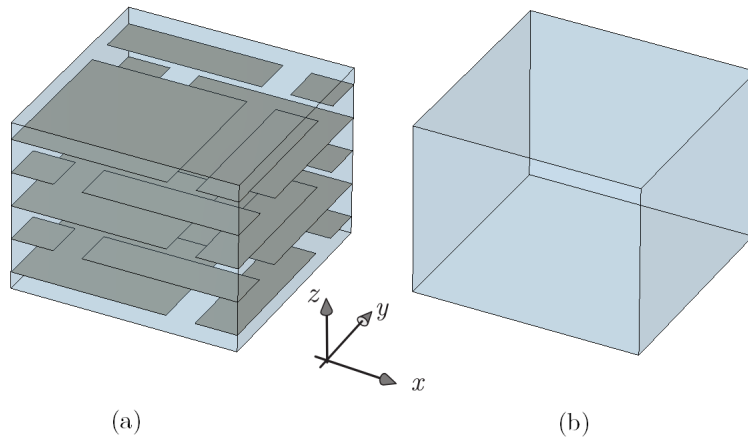


Figure 4.2: (a) Unit cell of an ADL composed of 5 non-aligned layers. The ADL is consisted of layers of perfectly conducting square patches with $d_x = d_y = 0.0785\lambda_0$, $d_z = 0.012\lambda_0$, $w_x = w_y = 0.01\lambda_0$, $s_x = s_y = 0.5d_x$, with λ_0 being the wavelength at the calculation frequency. The patches are embedded in material with $\epsilon_{host} = 1$. (b) An anisotropic slab with the same height and effective parameter as aforementioned ADL.

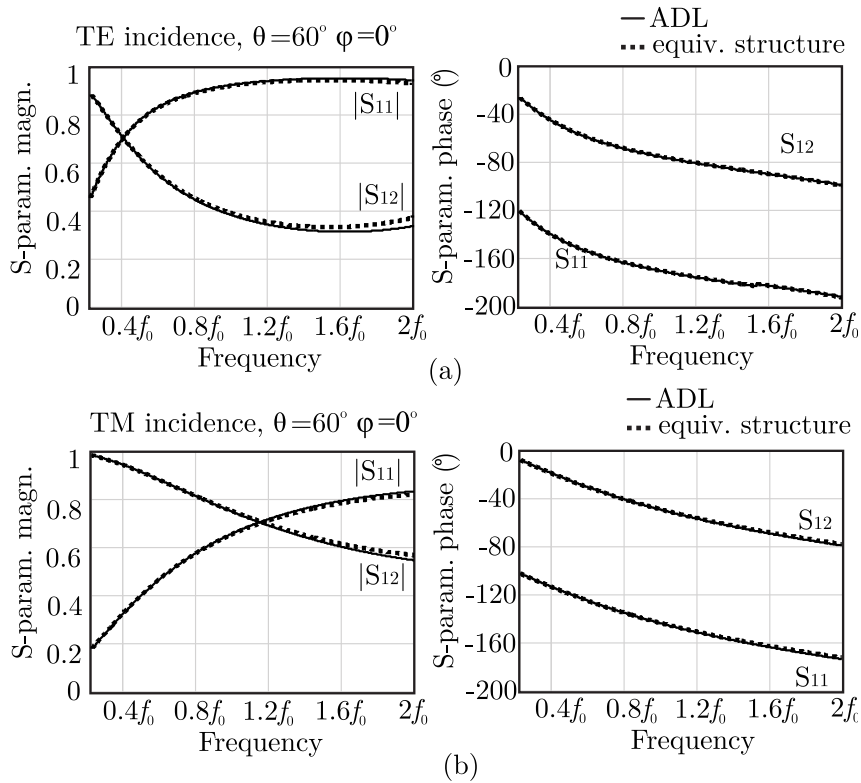


Figure 4.3: Scattering parameters comparison between ADL and its equivalent slab. (a) TE and (b) TM polarization of incidence plane wave arriving from oblique angle $\theta = 60^\circ$ and $\phi = 0^\circ$.

The comparisons are shown in figure 4.3 for both TE and TM polarization. A good matching can be implied from this result, signaling that the method of homogenization is valid for structure studied in this thesis.

4.2 Dependence of the Effective Parameters on the Geometry of the Structure

The described analytical method of homogenization means that the process of calculating the effective parameters can be done faster than a full-wave simulation without penalty in accuracy. Sweeping of parameters is also an hassle-free process. Furthermore, the analytical method can be used to give insight towards the dependence of the ADL structure on its effective parameters, such as the periods, the inter-layer distance, the slot width, or the shift between the layers.

The variation of the ϵ_x and μ_z as a function of the shift is reported in Fig. 4.4. The curves are shown for different values of the slot width ($w_x = w_y = w$), different periodicity of the patches ($d_x = d_y = d$), and different values of the inter-layer distance (d_z). It can be noted that the permittivity components ϵ_x and ϵ_y increase with the shift, because of the raised mutual capacitance between layers. An opposite behavior is observed for the permeability component μ_z , which decreases as a function of the shift.

For square ADL ($d_x = d_y = d, w_x = w_y = w$) with equal shift in x and y ($s_x = s_y$) that is studied in this thesis, the condition $\epsilon_x = \epsilon_y$ is satisfied, confirming that the structure holds uniaxial property. It is also evident that the value of ϵ_z is the same as the host permittivity of the ADL, ϵ_{host} , because the z -component of the electric field does not interact with the horizontal patches hosted in the medium. It can be noted that the permittivity components ϵ_x and ϵ_y increase with the shift, because of the raised mutual capacitance between layers. A larger size of the patches also brings higher permittivity components. Moreover, smaller values of inter-layer distance d_z lead to larger variation of permittivity as a function of the shift. Thus, for small inter-layer distances, very wide ranges of permittivity values can be synthesized by only varying the shift.

An opposite behavior is observed for the permeability component μ_z , which decreases as a function of the shift. The value of μ_z in ADL with finite height along the z axis is consistently < 1 , which is lower than relative permeability of vacuum. This implies that strong diamagnetic effects are occurring in the case of TE incidence, for which the incident magnetic field has a non-zero z -component. A structure with diamagnetic property creates an induced magnetic field in a direction that is opposite to the incidence magnetic field. Indeed, in TE incidence case, the patches support loop currents that produce a magnetic field (magnetization) opposite to the incident one (illustrated in Fig. ??). Therefore, the total magnetic field inside the ADL is reduced compared to the external one (i.e., $\mu_z < 1$). The other components of the permeability tensors are $\mu_x = \mu_y = 1$.

4.3 Refractive Index of ADLs

The index of refraction, n , as a function of the angle of incidence is important to describe the property of the ADL. As mentioned in chapter 1, the ideal material to tackle the surface-wave problem with current planar antennas is a material whose refractive index goes lower as the angle of incidence grows to the grazing angle. To obtain the refractive index as a function of angle for both TE and TM incidence, the following expressions are used [46]:

$$\begin{aligned} n^{TE} &= \sqrt{\epsilon_y \mu_x + (1 - \mu_x / \mu_z) \sin^2 \theta_1} \\ n^{TM} &= \sqrt{\epsilon_x \mu_y + (1 - \epsilon_x / \epsilon_z) \sin^2 \theta_1}. \end{aligned} \quad (4.3)$$

Figure 4.6 shows the square of the refractive index n^2 , over the angle of propagation of a plane wave inside the ADL. It is visible that the n^2 goes lower as the angle grows, and for broadside incidence, TE

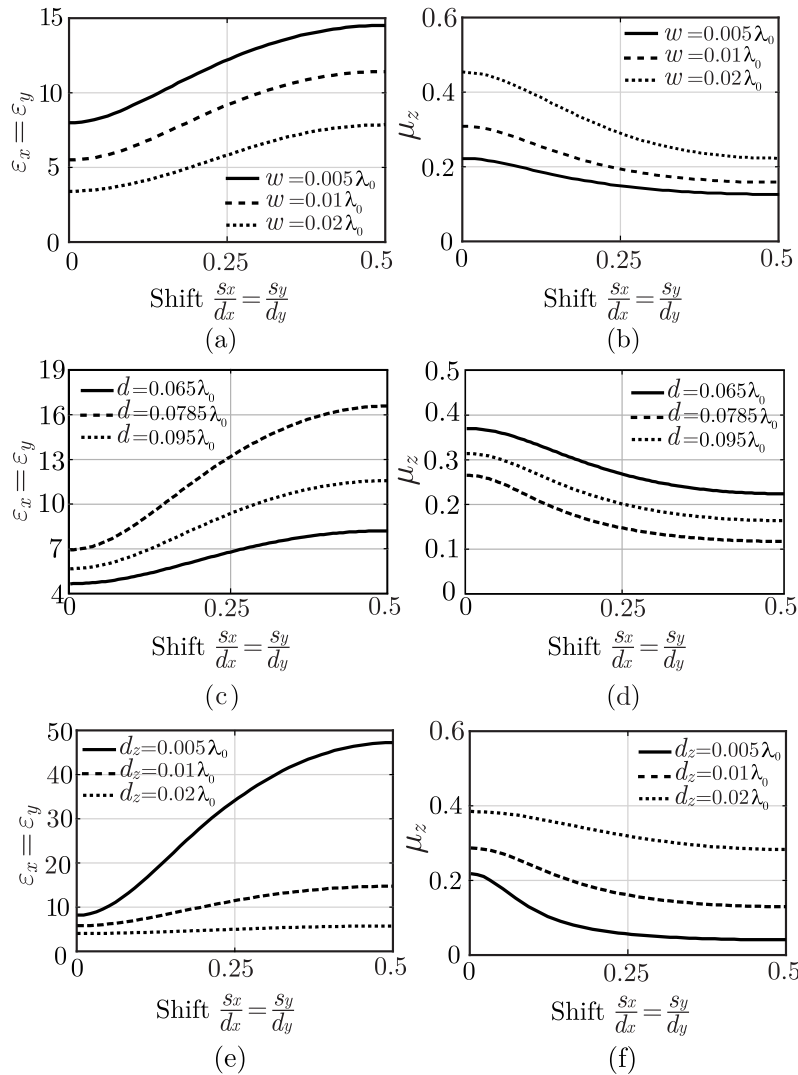


Figure 4.4: Equivalent x - and y - components of the relative permittivity tensor and equivalent z -component of the relative permeability tensor, as a function of the shift. The ADL is composed of 5 perfectly conducting layers of patches embedded in a medium with $\epsilon_{r,\text{host}} = 1$, where: (a)-(b) $d_x = d_y = 0.0785\lambda_0$, $d_z = 0.012\lambda_0$, and different slot widths, (c)-(d) $w_x = w_y = 0.01\lambda_0$, $d_z = 0.012\lambda_0$, and different periodicity, (e)-(f) $d_x = d_y = 0.0785\lambda_0$, $w_x = w_y = 0.01\lambda_0$, and different inter-layer distance, with λ_0 being the wavelength at the calculation frequency.

and TM incidence have the same refractive index. For TM incidence, the number reduces to the n^2 of the host for grazing angles, since the electric field becomes orthogonal to the patches and only feels the hosting medium. The TE case instead yields a refractive index enhancement also for grazing angles, for which the field is still parallel to the patches. In Fig. 4.6, the term ‘angle in ADL’ is mentioned. This is done to distinguish the angle of incidence in the free space and the resulting angle of propagation in the ADL due to refraction that happens at the interface. The angle in ADL can be simply calculated using Snell’s law of refraction. Figure 4.7 shows an example on how the incident wave refracts and the resulting angle of the wave propagating in the ADL. Since the refractive index is dependent on the modes, the angle in ADL is different for the two modes.

Figure 4.8 highlights the broadband property of the ADL, taking ADLs with different inter-layer distances and plotting its broadside n^2 over frequency. The refractive index of the ADL shows that, under the assumption of sub-wavelength patches, the equivalent parameters are essentially constant with the

TE incidence

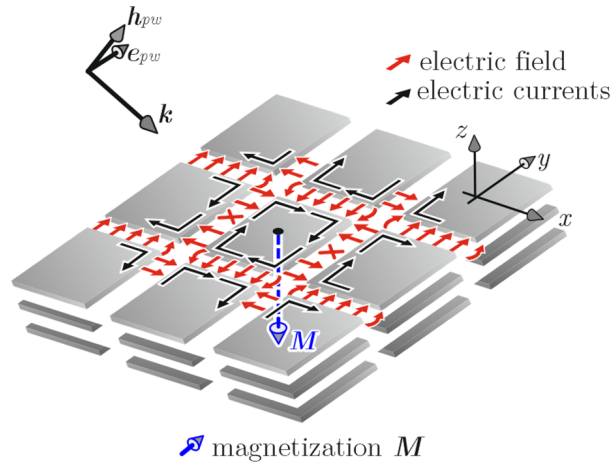


Figure 4.5: Illustration upon the diamagnetism of ADLs. For TE incidence, the induced electric field distribution in the layer creates electric current loops on the metal patches. The loops are inducing magnetic field with the opposite sign of the incident magnetic field, h_i .

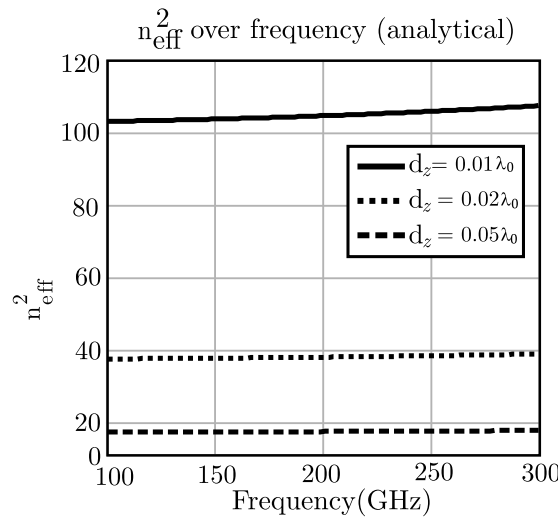


Figure 4.6: Square of refractive index, evaluated from equation (4.3), over angle of incidence in ADL. The ADL is composed of 5 layers of PEC patches with $d_x = d_y = 0.0785\lambda_0$, $w_x = w_y = 0.01\lambda_0$, $d_z = 0.012\lambda_0$, and $s_x = s_y = 0.5d_x$ where λ_0 is the wavelength at the calculation frequency. The ADL is hosted in a material with $\epsilon_{r,\text{host}} = 1$.

frequency. Dispersive behavior will occur at higher frequencies, when the patches become comparable to the wavelength. However, the formulas derived in this thesis are valid only under the assumption of sub-wavelength patches, which is always the case in practical ADL designs.

The refractive index of ADLs are related to the permittivity and permeability, thus naturally it is linked to the structure geometry. Figure 4.9 shows the range of resulting n^2 with tolerance applied in the geometrical parameters over the angle of incidence in the ADLs. This information is relevant to identify the most critical parameters in a manufacturing process and the tolerances associated with the practical fabrication of ADLs.

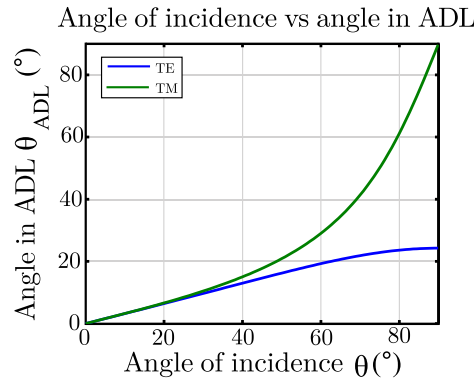


Figure 4.7: Angle in ADL over the angle of incidence. The ADL is hosted in free-space and is composed of 5 layers with $d_x = d_y = 0.0785\lambda_0$, $w_x = w_y = 0.01\lambda_0$, $d_z = 0.012\lambda_0$, and $s_x/d_x = s_y/d_y = 0.5$, where λ_0 is the wavelength at the calculation frequency at 300 GHz.

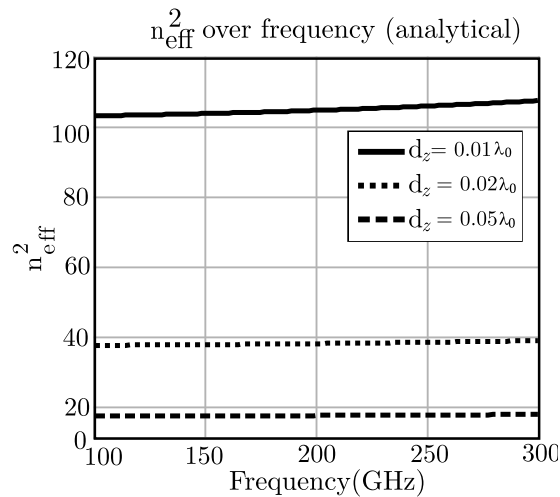


Figure 4.8: Square of refractive index over frequency. The ADL is composed of 5 layers of patches with $d_x = d_y = 0.2\lambda_0$, $w_x = w_y = 0.01\lambda_0$, and $s_x = s_y = 0.5d_x$ where λ_0 is the wavelength at the calculation frequency. The ADL is hosted in a material with $\epsilon = 1$.

4.4 Representation of Losses in Effective Parameters

The permittivity and permeability parameters are generally complex numbers. The imaginary part of the permittivity accounts for losses in the medium due to the damping of the vibrating dipole moments [47]. Dielectrics are usually characterized by the real part of the permittivity, and the loss tangent, $\tan \delta$, at a certain frequency. The relation of the loss tangent and the complex permittivity is given by

$$\epsilon = \epsilon' - j\epsilon'' = \epsilon'(1 - j \tan \delta) \quad (4.4)$$

with ϵ' and ϵ'' are the real and imaginary parts of the permittivity.

The imaginary part of the permeability is also related to the loss due to the damping process [47, 48]. Thus, the magnetic loss tangent can be introduced as

$$\mu = \mu' - j\mu'' = \mu'(1 - j \tan \delta_m) \quad (4.5)$$

where μ' and μ'' are the real and imaginary parts of the permeability. The loss tangents are frequency dependent. The presence of magnetic loss tangent is related to the fact that ADLs studied in this thesis

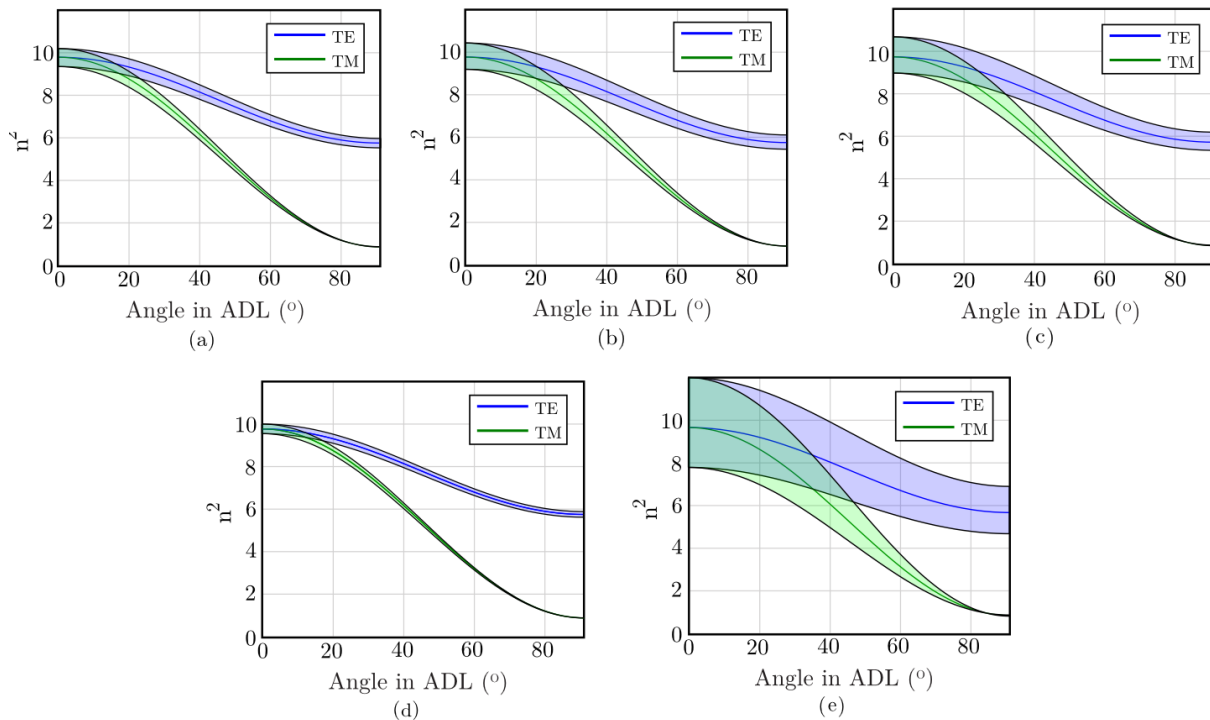


Figure 4.9: Square of index refraction (n^2) as function of angle incidence in ADL for TE and TM incidence. The plot has certain range that shows 5% tolerance in the (a) shift (b) inter-layer distance (c) periodicity (d) slot width (e) all geometrical parameters aforementioned. The ADL composed of 5 layers with $d_x = d_y = 0.0785\lambda_0$, $w_x = w_y = 0.01\lambda_0$, $d_z = 0.012\lambda_0$, and $s_x/d_x = s_y/d_y = 0.5$, where λ_0 is the wavelength at the calculation frequency at 300 GHz. The patches is hosted in the free-space.

is a diamagnetic material. There are losses introduced by the magnetization when the patches are not perfectly conducting.

The previous section considered ADLs made of perfectly conducting patches, thus the permittivity and permeability only have the real values. Introducing the finite conductivity of the metal cause the permittivity and permeability to have complex values. These complex quantities can be analytically calculated from the scattering parameters using the same method as explained in the previous section. To evaluate that the method is valid, a simulation is made via CST [22] to simulate an anisotropic slab with complex permittivity and permeability that are analogous to an ADL composed of 5 layers of lossy patches ($\sigma = 1000$ S/m) with geometrical parameters $d_x = d_y = 0.095\lambda_0$, $w_x = w_y = 0.01\lambda_0$, and $d_z = 0.02\lambda_0$, where λ_0 being the wavelength at calculation frequency. The scattering parameter of the anisotropic slab is compared to the analytically calculated scattering parameters of the corresponding ADL, shown in Fig. 4.10. The comparison shows an excellent agreement, indicating the analytical solution is rigorous.

In Fig. 4.11, the analytical complex permittivity and permeability are shown. An unrealistic case with $\sigma = 1000$ S/m is taken due to the low losses of the realistic ADLs. The complex values are carried by ϵ_x , ϵ_y , and μ_z . The ϵ_z for structure studied in this thesis is related to the propagation in the host material (without the patches), thus having only real values when the dielectric is assumed to be lossless. The tangent deltas are shown in Fig. 4.12 as function of frequency, showing that these quantities are frequency dependent. It is also evident that smaller size of the patches results in lower tangent deltas, a phenomenon that is reasonable: the size of the patches relates to the loss that is supported by them.

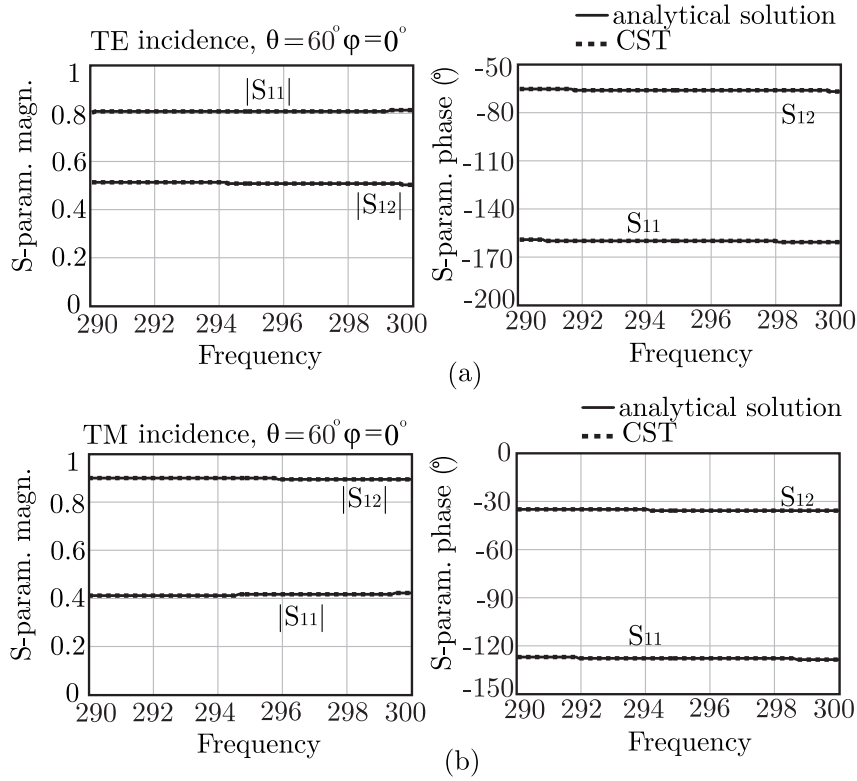


Figure 4.10: Comparison between CST simulations of the real and equivalent ADL slabs, in terms of the amplitude and phase of the reflection and transmission coefficients of a plane wave incident on 5-layers-ADL with finite conductivity ($\sigma = 1000\text{S/m}$), with angle of incidence $\theta = 60^\circ$, $\phi = 0^\circ$ (a) TE incidence (b) TM incidence. The geometrical parameters are $d_x = d_y = 0.095\lambda_0$, $w_x = w_y = 0.01\lambda_0$, and $d_z = 0.02\lambda_0$, with λ_0 being the wavelength at 300 GHz.

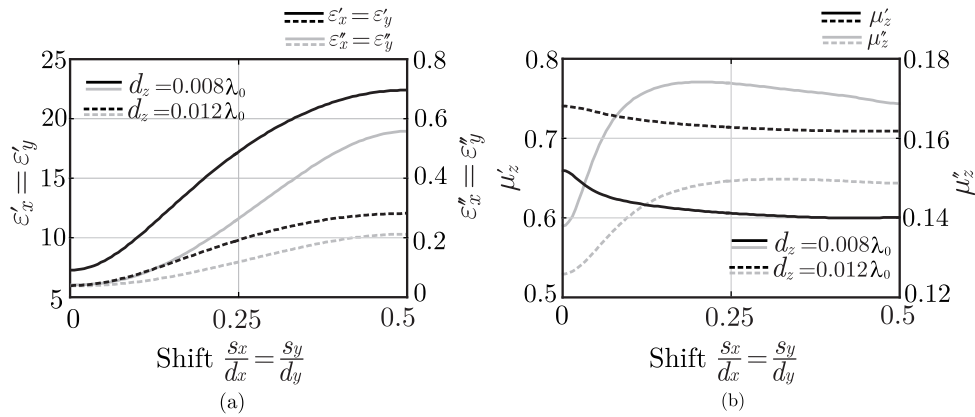


Figure 4.11: (a) Equivalent x - and y - components of the complex relative permittivity tensor and (b) equivalent z -component of the complex relative permeability tensor, as a function of the shift. The ADL is composed of 5 layers embedded in a medium with $\epsilon_{r,\text{host}} = 1$, with $d_x = d_y = 0.0785\lambda_0$, $w_x = w_y = 0.01\lambda_0$, with λ_0 being the wavelength at the calculation frequency. Two different inter-layer distances are investigated. The patches have finite conductivity $\sigma = 1000\text{ S/m}$.

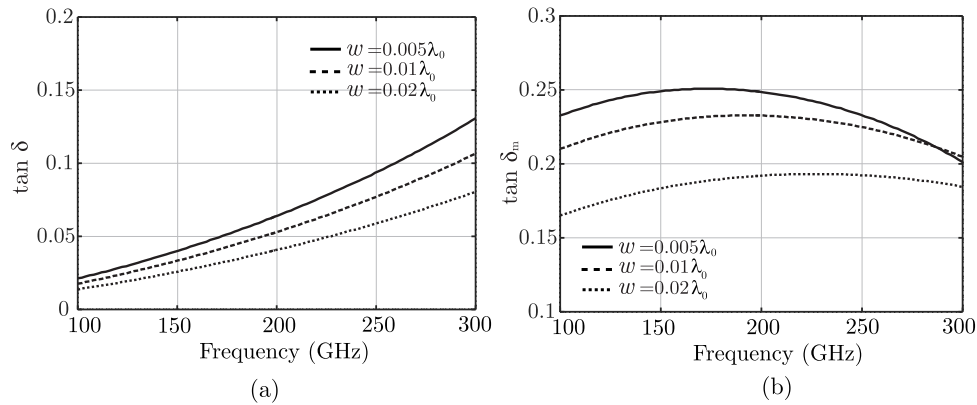


Figure 4.12: (a) Tangent delta and (b) magnetic tangent delta over frequency. The ADL is composed of 5 layers embedded in a medium with $\epsilon_{r,host} = 1$, with $d_x = d_y = 0.0785\lambda_0$, $w_x = w_y = w = 0.01\lambda_0$, $s_x = s_y = 0.5d_x$ with λ_0 being the wavelength at the calculation frequency. Three different sizes of patches with finite conductivity $\sigma = 1000$ S/m are investigated.

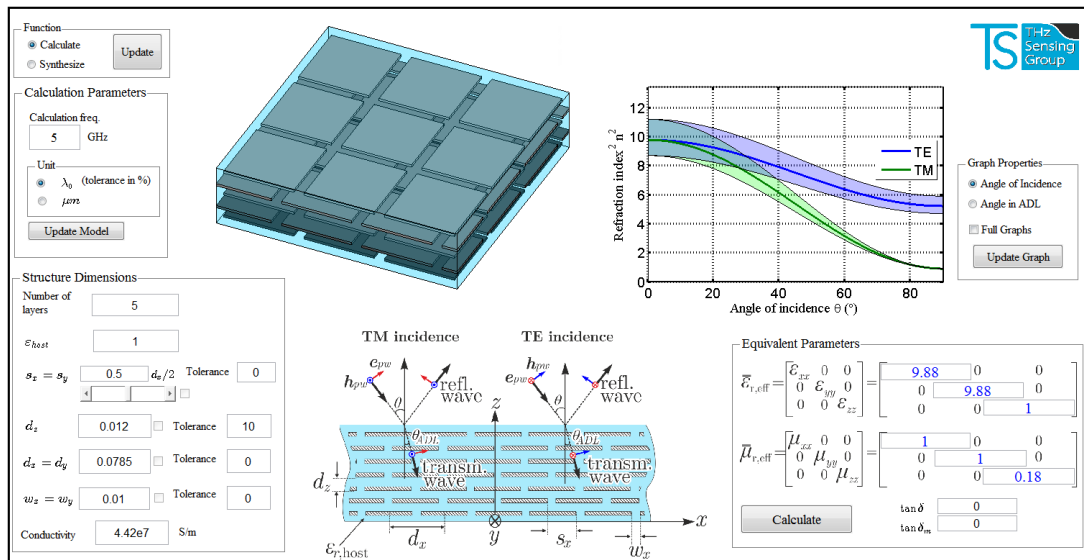


Figure 4.13: Snippet of the GUI developed to characterize ADLs.

4.5 GUI based on Analytical Solutions for ADL Design

ADLs are versatile structure that are exploitable for enhancing the performance of integrated antennas, thus in foreseeable future more designs will be made. A graphical user interface (GUI) that performs the analytical solutions for the ADLs can be an aid in the design process. GUI based on analytical solutions performs faster than a full-wave commercial simulator. Analytical solutions of the square ADLs that are reported in this thesis have been shown to be accurate when compared to the commercial simulator. Therefore, in this thesis, a GUI that implements all the analytical solutions previously presented is developed, with the aim of rendering the analysis and the design as user friendly as possible.

The beta version of the GUI that is developed is shown in Fig. 4.13. The GUI takes the structure geometries as input and gives the effective parameters as output. It provides the permittivity and permeability as tensors and the square of refractive index plot over the angle (incidence angle or angle in ADL). The tangent deltas are also shown. The user also has a choice of giving information about tolerances of the geometrical input.

Besides the analysis, the tool also implements the synthesis, by retrieving a possible set of geometrical parameters, given certain effective parameters. This synthesis function is a relevant feature that will allow ease in design process, another plus that is not achievable by using commercial solver. The user can also give to certain parameters a fixed value, and the code will optimize for the remaining parameters that are free. This feature is deemed to be necessary due to the possibility of specific limitation on the manufacturing process. The GUI also shows three dimensional model of the ADL's unit cell which can be an aid in visualizing the structure. With this GUI, knowing an ADL's effective parameters or designing one given the target electrical properties is achievable within seconds.

Chapter 5

Conclusions and Future Work

5.1 Summary and Conclusions

This thesis discussed Artificial Dielectric Layers (ADLs), expanding the work that was done in the literature to accommodate the alternate shift between layers (shifted ADLs) and the effect of finite conductivity of the patches composing the ADLs. Those two attributes are deemed to be relevant for the design of ADLs: the shift introduces another significant degree of freedom and the finite conductivity relates to the losses that occur in the structure. Closed-form solutions were given along with the analytical model of the ADL. Those solutions were shown to be accurate when compared with full wave simulations. The effective parameters of the ADLs were also extracted and studied to complete the understanding of the ADL as a type of metamaterial.

The analysis of the single layer of periodic square patches was done in chapter 2, aiming at providing the description of the interaction between the structure and a generic plane wave, both for the lossless case and the lossy case. Magnetic field integral equations were defined for these problems, containing magnetic currents as unknowns. The solution is found by expanding the magnetic currents into four basis functions defined over the entire unit cell. The terms of the admittance matrix are calculated in the spectral domain, with the spectral domain Green's function that is appropriate for each of the cases. The analysis leads to an equivalent circuit that is rigorous to describe the scattering property of the structure. The decoupling property of the TE and TM modes is observed, along with the azimuthal independence property of the structure.

In chapter 3, the stacked layers of periodic square patches, creating the ADL, was studied. The analysis of the single layer is extended to the three-dimensional multi-layer case. The reactive coupling due to the small inter-layer distance is considered. The finiteness effects of the ADL height are also taken into account with the by employing with the semi-infinite cascade solutions for the edge layers. The inclusion of the shift is analyzed, modifying the integral equations to account the shift between adjacent layer. The closed-form solutions are formulated by solving the integral equations, accounting for the inter-layer reactive coupling. Furthermore, the finite conductivity is also introduced in the analysis of the ADLs, extending the solutions to include the surface impedance. The equivalent circuit representation of the ADL is given and the results are compared with commercial solvers to shows the validity of the formulas.

The representation of an ADL by its effective parameters was done in chapter 4. The ADLs can be represented by the tensors of permittivity and permeability. The effective permittivity and permeability is attained from the scattering parameters which can be gained from the solutions presented in chapter 3. The effective parameters reveal that the ADLs are indeed equal to anisotropic materials and present diamagnetic properties. ADLs that are made of square patches also show uniaxial characteristic. The

broadband properties of the ADLs is also discussed, alongside the effect of the structure geometry and the tolerances on the effective parameters. Furthermore, the representation of the losses is also included in the effective parameters. A graphical user interface was implemented based on this thesis to render all the formulas given of immediate use for design.

5.2 Future Work

This thesis extends the analysis of the ADLs to a certain degree. Considering the prospect of the ADL in the future to enable high frequency applications, a continuous research of the structure should be conducted. Possible future analysis that can provide more development of the concept are enlisted:

1. The losses studied in this thesis are limited to one incoming plane-wave that illuminates the structure. Thus, losses can be further investigated by considering a near source radiating in the presence of the ADL, which is a typical configuration for ADL applications. The field radiated by the source can be expanded in a spectrum of plane-waves, so the total losses can be found by integrating the contribution of each plane wave over such spectrum.
2. ADLs are made of metal patches hosted in a host medium. The analysis of losses introduced by the patches has been included in this thesis. However, the losses introduced by the dielectric where these patches hosted can be also included as an useful information to assist the design process.
3. Another interesting generalization could be the case when the shift itself is not periodic but it changes for each layer. This would lead to a local variation of the equivalent impedance of the layers (inhomogeneous dielectric) that can further improve the design flexibility, for example for artificial lens designs.
4. The GUI is still under development. A project called AD-HOC is ongoing within the Terahertz Sensing group, which aims at optimizing the fabrication of ADLs in the Else Kooi Lab. This project will provide some technological limitations on the ADLs that can be manufactured, and such information will be included in the GUI. Extensive testing of the software should also be performed to ensure that all codes are debugged and also to set the validity bounds of the assumed approximations.

5.3 Publications

The work performed in this thesis has lead to the following publications:

Journal paper:

1. D. Cavallo and C. Felita "Analytical formulas for artificial dielectrics with non-aligned layers" *IEEE Transactions on Antennas and Propagation*, to appear in Vol. 65, No. 10, 2017.

Conference papers:

1. D. Cavallo and C. Felita "Analytical models for artificial dielectrics with non-aligned layers," *IEEE Antennas and Propagation Society International Symposium*, San Diego, California, USA, July 9-14, 2017.
-

2. D. Cavallo and C. Felita "Analysis of artificial dielectrics composed of non-aligned layers," 11th *European Conference on Antennas and Propagation*, Paris, France, March 19-24, 2017 (received the Best Paper Award in Electromagnetics and Antenna Theory).
-

Bibliography

- [1] D. M. Pozar, “Recent developments in the analysis and design of microstrip arrays,” in *1992 Symposium on Antenna Technology and Applied Electromagnetics*, Aug 1992, pp. 509–516.
- [2] B. Fleming, “Sensors? A forecast [automotive electronics],” *IEEE Vehicular Technology Magazine*, vol. 8, no. 3, pp. 4–12, Sept 2013.
- [3] H. J. Song and T. Nagatsuma, “Present and future of terahertz communications,” *IEEE Transactions on Terahertz Science and Technology*, vol. 1, no. 1, pp. 256–263, Sept 2011.
- [4] T. Kleine-Ostmann and T. Nagatsuma, “A review on terahertz communications research,” *Journal of Infrared, Millimeter, and Terahertz Waves*, vol. 32, no. 2, pp. 143–171, 2011.
- [5] K. Sengupta and A. Hajimiri, “A 0.28 THz power-generation and beam-steering array in CMOS based on distributed active radiators,” *IEEE Journal of Solid-State Circuits*, vol. 47, no. 12, pp. 3013–3031, Dec 2012.
- [6] J. M. Edwards and G. M. Rebeiz, “High-efficiency elliptical slot antennas with quartz superstrates for silicon RFICs,” *IEEE Transactions on Antennas and Propagation*, vol. 60, no. 11, pp. 5010–5020, Nov 2012.
- [7] F. Mesa, C. di Nallo, and D. R. Jackson, “The theory of surface-wave and space-wave leaky-mode excitation on microstrip lines,” *IEEE Transactions on Microwave Theory and Techniques*, vol. 47, no. 2, pp. 207–215, Feb 1999.
- [8] W. E. Kock, “Metallic delay lenses,” *The Bell System Technical Journal*, vol. 27, no. 1, pp. 58–82, Jan 1948.
- [9] S. S. D. Jones and J. Brown, “Metallic delay lenses,” *Nature*, vol. 163, no. 4139, pp. 324–325, Feb 1949.
- [10] R. E. Collin, *Field Theory of Guided Waves, 2nd Edition*. Wiley-IEEE Press, 1990.
- [11] W. H. Syed and A. Neto, “Front-to-back ratio enhancement of planar printed antennas by means of artificial dielectric layers,” *IEEE Transactions on Antennas and Propagation*, vol. 61, no. 11, pp. 5408–5416, Nov 2013.
- [12] W. H. Syed, G. Fiorentino, D. Cavallo, M. Spirito, P. M. Sarro, and A. Neto, “Design, fabrication, and measurements of a 0.3 THz on-chip double slot antenna enhanced by artificial dielectrics,” *IEEE Transactions on Terahertz Science and Technology*, vol. 5, no. 2, pp. 288–298, March 2015.
- [13] W. H. Syed, D. Cavallo, H. T. Shivamurthy, and A. Neto, “Wideband, wide-scan planar array of connected slots loaded with artificial dielectric superstrates,” *IEEE Transactions on Antennas and Propagation*, vol. 64, no. 2, pp. 543–553, Feb 2016.

-
- [14] D. Cavallo, W. H. Syed, and A. Neto, "Closed-form analysis of artificial dielectric layers; Part I: Properties of a single layer under plane-wave incidence," *IEEE Transactions on Antennas and Propagation*, vol. 62, no. 12, pp. 6256–6264, Dec 2014.
- [15] —, "Closed-form analysis of artificial dielectric layers; Part II: Extension to multiple layers and arbitrary illumination," *IEEE Transactions on Antennas and Propagation*, vol. 62, no. 12, pp. 6265–6273, Dec 2014.
- [16] N. Marcuvitz, *Waveguide handbook*. Iet, 1951, no. 21.
- [17] J. R. Wait, "Theories of scattering from wire-grid and mesh structures," in *Electromagnetic scattering*, P. L. E. Uslenghi, Ed. Elsevier, 1978, pp. 12–34.
- [18] L. B. Whitbourn and R. C. Compton, "Equivalent-circuit formulas for metal grid reflectors at a dielectric boundary," *Applied Optics*, vol. 24, no. 2, pp. 217–220, 1985.
- [19] R. C. Compton and D. B. Rutledge, "Approximation techniques for planar periodic structures," *IEEE Transactions on Microwave Theory and Techniques*, vol. 33, no. 10, pp. 1083–1088, Oct 1985.
- [20] O. Luukkonen, C. Simovski, G. Granet, G. Goussetis, D. Lioubtchenko, A. V. Raisanen, and S. A. Tretyakov, "Simple and accurate analytical model of planar grids and high-impedance surfaces comprising metal strips or patches," *IEEE Transactions on Antennas and Propagation*, vol. 56, no. 6, pp. 1624–1632, June 2008.
- [21] S. Tretyakov, *Analytical modeling in applied electromagnetics*. Artech House, 2003.
- [22] CST Microwave Studio. [Online]. Available: <http://www.cst.com/>
- [23] S. A. Schelkunoff, "Some equivalence theorems of electromagnetics and their application to radiation problems," *The Bell System Technical Journal*, vol. 15, no. 1, pp. 92–112, Jan 1936.
- [24] W. H. Syed, G. Fiorentino, D. Cavallo, M. Spirito, P. M. Sarro, and A. Neto, "Design, fabrication, and measurements of a 0.3 THz on-chip double slot antenna enhanced by artificial dielectrics," *IEEE Transactions on Terahertz Science and Technology*, vol. 5, no. 2, pp. 288–298, March 2015.
- [25] B. X. Wang and G. Z. Wang, "Quad-band terahertz absorber based on a simple design of metamaterial resonator," *IEEE Photonics Journal*, vol. 8, no. 6, pp. 1–8, Dec 2016.
- [26] M. Albani, A. Mazzinghi, and A. Freni, "Rigorous MoM analysis of finite conductivity effects in RLSA antennas," *Antennas and Propagation, IEEE Transactions on*, vol. 59, no. 11, pp. 4023–4032, Nov 2011.
- [27] M. A. Leontovich, *Approximate boundary conditions for electromagnetic field on the surface of conducting bodies*. Moscow, Russia: Academy of Sciences, 1948.
- [28] K. M. Mitzner, "An integral equation approach to scattering from a body of finite conductivity," *Radio Science*, vol. 2, no. 12, pp. 1459–1470, Dec 1967.
- [29] M. A. d. Pino, H. T. Shivamurthy, D. Cavallo, L. Galatro, and M. Spirito, "BiCMOS integrated waveguide with artificial dielectric at submillimeter wave frequencies," in *2016 IEEE MTT-S International Microwave Symposium (IMS)*, May 2016, pp. 1–4.
-

-
- [30] D. Cavallo, W. H. Syed, and A. Neto, "A 5:1 connected slot array loaded with artificial dielectric layers," in *2016 IEEE International Symposium on Phased Array Systems and Technology (PAST)*, Oct 2016, pp. 1–4.
- [31] R. A. Shore and A. D. Yaghjian, "Traveling waves on three-dimensional periodic arrays of two different alternating magnetodielectric spheres," *IEEE Transactions on Antennas and Propagation*, vol. 57, no. 10, pp. 3077–3091, Oct 2009.
- [32] C. S. Kaipa, A. B. Yakovlev, F. Medina, F. Mesa, C. A. Butler, and A. P. Hibbins, "Circuit modeling of the transmissivity of stacked two-dimensional metallic meshes," *Optics express*, vol. 18, no. 13, pp. 13 309–13 320, 2010.
- [33] S. B. Cohn, "Electrolytic-tank measurements for microwave metallic delay-lens media," *Journal of Applied Physics*, vol. 21, no. 7, pp. 674–680, 1950.
- [34] J. Brown, "The design of metallic delay dielectrics," *Proceedings of the IEE - Part III: Radio and Communication Engineering*, vol. 97, no. 45, pp. 45–48, January 1950.
- [35] W. H. Syed and A. Neto, "Front-to-back ratio enhancement of planar printed antennas by means of artificial dielectric layers," *IEEE Transactions on Antennas and Propagation*, vol. 61, no. 11, pp. 5408–5416, Nov 2013.
- [36] E. Martini, G. M. Sardi, and S. Maci, "Homogenization processes and retrieval of equivalent constitutive parameters for multisurface-metamaterials," *IEEE Transactions on Antennas and Propagation*, vol. 62, no. 4, pp. 2081–2092, April 2014.
- [37] S. Monni, G. Gerini, A. Neto, and A. G. Tijhuis, "Multimode equivalent networks for the design and analysis of frequency selective surfaces," *IEEE Transactions on Antennas and Propagation*, vol. 55, no. 10, pp. 2824–2835, Oct 2007.
- [38] W.H.Syed, "On the control of surface waves in integrated antennas: Analysis and design exploiting artificial dielectric layers," Ph.D. dissertation, 2015.
- [39] ANSYS HFSS. [Online]. Available: <http://www.ansys.com/products/electronics/ansys-hfss>
- [40] D. Smith, S. Schultz, P. Markoš, and C. Soukoulis, "Determination of effective permittivity and permeability of metamaterials from reflection and transmission coefficients," *Physical Review B*, vol. 65, no. 19, p. 195104, 2002.
- [41] U. C. Hasar, A. Muratoglu, M. Bute, J. J. Barroso, and M. Ertugrul, "Effective constitutive parameters retrieval method for bianisotropic metamaterials using waveguide measurements," *IEEE Transactions on Microwave Theory and Techniques*, vol. 65, no. 5, pp. 1488–1497, May 2017.
- [42] Y. Shi, Z. Y. Li, K. Li, L. Li, and C. H. Liang, "A retrieval method of effective electromagnetic parameters for inhomogeneous metamaterials," *IEEE Transactions on Microwave Theory and Techniques*, vol. 65, no. 4, pp. 1160–1178, April 2017.
- [43] X. Chen, T. M. Grzegorzcyk, B.-I. Wu, J. Pacheco Jr, and J. A. Kong, "Robust method to retrieve the constitutive effective parameters of metamaterials," *Physical Review E*, vol. 70, no. 1, p. 016608, 2004.
- [44] C. Menzel, C. Rockstuhl, T. Paul, F. Lederer, and T. Pertsch, "Retrieving effective parameters for metamaterials at oblique incidence," *Physical Review B*, vol. 77, no. 19, p. 195328, 2008.
-

- [45] Z. Li, K. Aydin, and E. Ozbay, "Determination of the effective constitutive parameters of bianisotropic metamaterials from reflection and transmission coefficients," *Physical review E*, vol. 79, no. 2, p. 026610, 2009.
 - [46] D. Cohen and R. Shavit, "Bi-anisotropic metamaterials effective constitutive parameters extraction using oblique incidence S-Parameters method," *IEEE Transactions on Antennas and Propagation*, vol. 63, no. 5, pp. 2071–2078, May 2015.
 - [47] D. Pozar, *Microwave Engineering, 4th Edition*. Wiley Global Education, 2011.
 - [48] A. Kabiri, L. Yousefi, and O. M. Ramahi, "On the fundamental limitations of artificial magnetic materials," *IEEE Transactions on Antennas and Propagation*, vol. 58, no. 7, pp. 2345–2353, July 2010.
-

Appendix A

Solutions of the Admittance Matrix

A.1 Spectral Domain Expression of the Admittances

In this appendix, the self and mutual admittances are defined in the spectral domain, to allow for closed-form solution of the integral equation (2.3). The Fourier transforms of basis functions in (2.8) are given by

$$\begin{aligned}
 \mathbf{F}_1(k_{xm}, k_{ym}) &= d_x \delta(m_x) \text{sinc}(k_{ym} w_y / 2) \hat{\mathbf{x}} \\
 \mathbf{F}_2(k_{xm}, k_{ym}) &= d_y \delta(m_y) \text{sinc}(k_{xm} w_x / 2) \hat{\mathbf{y}} \\
 \mathbf{F}_3(k_{xm}, k_{ym}) &= B_{d,x}(k_{xm}) \text{sinc}(k_{ym} w_y / 2) \hat{\mathbf{x}} \\
 \mathbf{F}_4(k_{xm}, k_{ym}) &= B_{d,y}(k_{ym}) \text{sinc}(k_{xm} w_x / 2) \hat{\mathbf{y}}.
 \end{aligned} \tag{A.1}$$

where $k_{xm} = k_{x0} - 2\pi m_x / d_x$ and $k_{ym} = k_{y0} - 2\pi m_y / d_y$ are the Floquet wavenumbers, B_d is the Fourier transform of the doublet function and it is given by eq. (39) in [14], and δ is a Kronecker delta-function.

The terms of the admittance matrix are computed in the spectral domain as

$$Y_{qp} = -\frac{1}{d_x d_y} \sum_{m_x} \sum_{m_y} \mathbf{F}_q^*(-k_{xm}, -k_{ym}) \mathbf{G}(k_{xm}, k_{ym}) \cdot \mathbf{F}_p(k_{xm}, k_{ym}) S(k_{xm}, k_{ym}) \tag{A.2}$$

while the forcing terms are given by

$$i_q = \frac{1}{\sqrt{d_x d_y}} 2h_i \hat{\mathbf{h}} \cdot \mathbf{F}_q^*(-k_{x0}, -k_{y0}) = 0 \tag{A.3}$$

where ‘ p ’ and ‘ q ’ are the indexes of the basis and the test functions, respectively, and h_i and $\hat{\mathbf{h}}$ are the amplitude and the unit vector orientation of the incident magnetic field, respectively. Assuming that the ADLs are hosted in a homogeneous medium, in (A.2) we used the following property of the spectral dyadic Green’s function \mathbf{G} :

$$\mathbf{G}(k_{xm}, k_{ym}, n_z d_z) = \mathbf{G}(k_{xm}, k_{ym}) e^{-jk_{zm} |n_z| d_z} \tag{A.4}$$

and all the sums on the n_z indexes are included in the following term:

$$S(k_{xm}, k_{ym}) = \sum_{n_z \text{ even}} e^{-jk_{zm} |n_z| d_z} - e^{j(k_{xm} - k_{xs}) s_x} e^{j(k_{ym} - k_{ys}) s_y} \sum_{n_z \text{ odd}} e^{-jk_{zm} |n_z| d_z}. \tag{A.5}$$

From (B.10) and (B.11) in Appendix B, we can also express $S(k_{xm}, k_{ym})$ in closed form as

$$S(k_{xm}, k_{ym}) = -j \cot(k_{zm} d_z) + j \csc(k_{zm} d_z) e^{j(k_{xm} - k_{xs}) s_x} e^{j(k_{ym} - k_{ys}) s_y}. \tag{A.6}$$

A.2 Reduction of the Number of Unknowns

The system of equations $\bar{\bar{\mathbf{Y}}}\bar{\mathbf{a}} = \bar{\mathbf{i}}$ starts as:

$$\begin{aligned} a_1 Y_{11} + a_2 Y_{12} + a_3 Y_{13} + a_4 Y_{14} &= 0 \\ a_1 Y_{21} + a_2 Y_{22} + a_3 Y_{23} + a_4 Y_{24} &= 0 \\ a_1 Y_{31} + a_2 Y_{32} + a_3 Y_{33} + a_4 Y_{34} &= 0 \\ a_1 Y_{41} + a_2 Y_{42} + a_3 Y_{43} + a_4 Y_{44} &= 0. \end{aligned} \quad (\text{A.7})$$

This equations (A.7) can be simplified by assuming, as in [14], that $B_{d,x}(k_{x0})$ and $B_{d,y}(k_{y0})$ are approximately 0. Such a condition applies because the projection of a progressive phase distribution (plane wave) onto an anti-symmetric function is negligible for electrically small periods. This assumption allows to neglect some terms of the admittance matrix $Y_{13} \approx Y_{31} \approx Y_{24} \approx Y_{42} \approx 0$.

$$\begin{aligned} a_1 Y_{11} + a_2 Y_{12} + a_4 Y_{14} &\approx 0 \\ a_1 Y_{21} + a_2 Y_{22} + a_3 Y_{23} &\approx 0 \\ a_2 Y_{32} + a_3 Y_{33} + a_4 Y_{34} &\approx 0 \\ a_1 Y_{41} + a_3 Y_{43} + a_4 Y_{44} &\approx 0. \end{aligned} \quad (\text{A.8})$$

Solving (A.8) for a_3 and a_4 gives:

$$\begin{aligned} a_3 &= -a_2 \frac{Y_{32} Y_{44}}{Y_{33} Y_{44} - Y_{34} Y_{43}} + a_1 \frac{Y_{41} Y_{34}}{Y_{33} Y_{44} - Y_{34} Y_{43}} \\ a_4 &= -a_1 \frac{Y_{41} Y_{33}}{Y_{33} Y_{44} - Y_{34} Y_{43}} + a_2 \frac{Y_{32} Y_{43}}{Y_{33} Y_{44} - Y_{34} Y_{43}} \end{aligned} \quad (\text{A.9})$$

which can be substituted back to (A.8), resulting in two linear equations instead of original four.

$$\begin{aligned} a_1 \left(Y_{11} - \frac{Y_{41} Y_{33} Y_{14}}{Y_{33} Y_{44} - Y_{34} Y_{43}} \right) + a_2 \left(Y_{12} + \frac{Y_{32} Y_{43} Y_{14}}{Y_{33} Y_{44} - Y_{34} Y_{43}} \right) &\approx 0 \\ a_1 \left(Y_{21} + \frac{Y_{41} Y_{34} Y_{23}}{Y_{33} Y_{44} - Y_{34} Y_{43}} \right) + a_2 \left(Y_{22} - \frac{Y_{32} Y_{44} Y_{23}}{Y_{33} Y_{44} - Y_{34} Y_{43}} \right) &\approx 0 \end{aligned} \quad (\text{A.10})$$

resulting in a reduced admittance matrix as

$$\bar{\bar{\mathbf{Y}}}_r = \begin{pmatrix} Y_{11} - \frac{Y_{41} Y_{14} Y_{33}}{Y_{33} Y_{44} - Y_{34} Y_{43}} & Y_{12} - \frac{Y_{32} Y_{43} Y_{14}}{Y_{33} Y_{44} - Y_{34} Y_{43}} \\ Y_{21} - \frac{Y_{41} Y_{23} Y_{34}}{Y_{33} Y_{44} - Y_{34} Y_{43}} & Y_{22} - \frac{Y_{32} Y_{23} Y_{33}}{Y_{33} Y_{44} - Y_{34} Y_{43}} \end{pmatrix} \quad (\text{A.11})$$

which satisfies the relation

$$\bar{\bar{\mathbf{Y}}}_r \begin{pmatrix} a_1 \\ a_2 \end{pmatrix} = \begin{pmatrix} 0 \\ 0 \end{pmatrix}. \quad (\text{A.12})$$

A.3 Simplified Admittance Matrix

The reduced admittance matrix can be further processed as shown in ???. To investigate the ADL structure under TE and TM plane-wave incidence, it is convenient to project the equations on the TE and TM vectors. This can be done by introducing the rotation matrix

$$\mathbf{R} = \begin{pmatrix} \cos(\phi) & \sin(\phi) \\ -\sin(\phi) & \cos(\phi) \end{pmatrix}. \quad (\text{A.13})$$

Pre-multiplying both the left and right hand sides of (A.12) by \mathbf{R} and noting that $\mathbf{R}^T \mathbf{R}$ is equal to the identity matrix \mathbf{I} , we can write

$$\mathbf{R} \bar{\bar{\mathbf{Y}}}_r \mathbf{R}^T \mathbf{R} \begin{pmatrix} a_1 \\ a_2 \end{pmatrix} = 0 \quad (\text{A.14})$$

or

$$\bar{\bar{\mathbf{Y}}}_{\text{TETM}} \begin{pmatrix} a_{\text{TE}} \\ a_{\text{TM}} \end{pmatrix} = \begin{pmatrix} 0 \\ 0 \end{pmatrix} \quad (\text{A.15})$$

where we define $\bar{\bar{\mathbf{Y}}}_{\text{TETM}} = \mathbf{R} \bar{\bar{\mathbf{Y}}}_r \mathbf{R}^T$. In the case of different shifts $s_x \neq s_y$, all the elements of the matrix are different from 0, thus the TE and TM component of the plane wave are coupled. Based on the result in ??, the admittance matrix can be written as the sum of two contributions

$$\bar{\bar{\mathbf{Y}}}_{\text{TETM}} = \bar{\bar{\mathbf{Y}}}_{\text{TL}} + \bar{\bar{\mathbf{Y}}}_{\text{ADL}}. \quad (\text{A.16})$$

The first term is diagonal and represents the transmission lines describing the propagation of the plane wave through the ADL structure:

$$\bar{\bar{\mathbf{Y}}}_{\text{TL}} = \begin{bmatrix} \frac{2j \tan(k_{z0} \frac{dz}{2})}{Z_{\text{0TE}}} & 0 \\ 0 & \frac{2j \tan(k_{z0} \frac{dz}{2})}{Z_{\text{0TM}}} \end{bmatrix} \quad (\text{A.17})$$

where $Z_{\text{0TE}} = \zeta_0 k_0 / k_{z0}$, $Z_{\text{0TM}} = \zeta_0 k_{z0} / k_0$ are the characteristic impedances of the TE and TM transmission lines representing the plane-wave propagation; moreover, $k_{z0} = k_0 \cos(\theta)$, and k_0 , ζ_0 are the free-space wavenumber and impedance, respectively. For an infinite cascade of ADLs, $\bar{\bar{\mathbf{Y}}}_{\text{TL}}$ represents two pairs of open stubs of length equal to half of the inter-layer spacing, as shown in Fig. A.1. The second matrix is the equivalent admittance of the layer and account for the coupling between TE and TM modes.

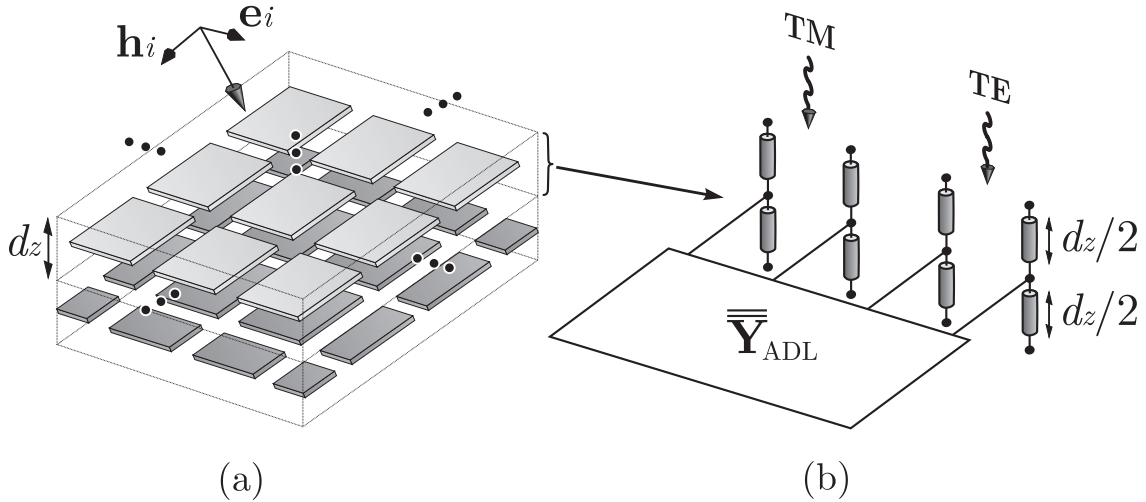


Figure A.1: Equivalent admittance of one layer of the ADLs embedded in an infinite cascade: (a) unit cell and (b) equivalent representation of the admittance matrix.

However, for $s_x = s_y$, it is shown in ?? that the non-diagonal terms of $\bar{\bar{\mathbf{Y}}}_{\text{ADL}}$ are approximately 0 and the matrix can be simplified as follows

$$\bar{\bar{\mathbf{Y}}}_{\text{ADL}} \approx \begin{bmatrix} jB_\infty (1 - \frac{\sin^2(\theta)}{2}) & 0 \\ 0 & jB_\infty \end{bmatrix} \quad (\text{A.18})$$

where we define the slot susceptance as

$$B_\infty \approx \frac{jk_0 d_y}{\zeta_0 \pi} \sum_{m \neq 0} \frac{|\text{sinc}(\pi m \frac{w_y}{d_y})|^2}{|m|} \cdot \left(-\cot(-j2\pi |m| \frac{d_z}{d_y}) + e^{j2\pi m \frac{s_y}{d_y}} \csc(-j2\pi |m| \frac{d_z}{d_y}) \right). \quad (\text{A.19})$$

Appendix B

Closed Form Solutions for Infinite and Semi-Infinite Sums

This appendix contains the closed form expression for the infinite and semi-infinite cascade of ADL. Those sums are included in function $S(k_{xm}, k_{ym})$, that is defined in eq.(.). This function is part of the spectral domain integral equations and it contains sums over even and odd indexes. The expression of the sum can be written as

$$\begin{aligned} \sum_{n_z} e^{-jk_{zm}|n_z|d_z} &= \dots + e^{-jk_{zm}0d_z} + e^{-jk_{zm}1d_z} + e^{-jk_{zm}2d_z} + \dots \\ &= \sum_{n_z, \text{even}} e^{-jk_{zm}|n_z|d_z} + \sum_{n_z, \text{odd}} e^{-jk_{zm}|n_z|d_z}. \end{aligned} \quad (\text{B.1})$$

The semi-infinite sums over even indexes (from 0 to $+\infty$) and odd indexes (from 1 to $+\infty$) are given by

$$\sum_{n_z(\text{even})=0}^{\infty} e^{-jk_{zm}|n_z|d_z} = 1 + e^{-jk_{zm}2d_z} + e^{-jk_{zm}4d_z} + \dots \quad (\text{B.2})$$

$$\sum_{n_z(\text{odd})=1}^{\infty} e^{-jk_{zm}|n_z|d_z} = e^{-jk_{zm}d_z} + e^{-jk_{zm}3d_z} + \dots \quad (\text{B.3})$$

With the change of variable $n'_z = n_z/2$, (B.2) can be expressed as

$$\sum_{n_z(\text{even})=0}^{\infty} e^{-jk_{zm}|n_z|d_z} = 1 + \sum_{n'_z=1}^{\infty} e^{-jk_{zm}2|n'_z|d_z}. \quad (\text{B.4})$$

From [10], these following identities can be used

$$\sum_{n=1}^{\infty} e^{jnx} = -\frac{1}{2} + \frac{j}{2} \cot \frac{x}{2}, \quad \sum_{x(\text{odd})=1}^{\infty} e^{jnx} = \frac{j}{2} \csc x \quad (\text{B.5})$$

so that (B.4) and (B.3) can be evaluated as

$$\sum_{n_z(\text{even})=0}^{\infty} e^{-jk_{zm}|n_z|d_z} = \frac{1}{2} - \frac{j}{2} \cot(k_{zm}d_z) \quad (\text{B.6})$$

$$\sum_{n_z(\text{odd})=1}^{\infty} e^{-jk_{zm}|n_z|d_z} = -\frac{j}{2} \csc(k_{zm}d_z). \quad (\text{B.7})$$

The solution for the infinite sums can be derived from the semi-infinite ones by noting that an infinite sum basically consists of two of a semi-infinite sum.

$$\sum_{n_z, \text{even}} e^{-jk_{zm}|n_z|d_z} = 2 \sum_{n_z(\text{even})=0}^{\infty} e^{-jk_{zm}|n_z|d_z} - 1 \quad (\text{B.8})$$

$$\sum_{n_z, \text{odd}} e^{-jk_{zm}|n_z|d_z} = 2 \sum_{n_z(\text{odd})=1}^{\infty} e^{-jk_{zm}|n_z|d_z} . \quad (\text{B.9})$$

This leads to the solution for the infinite sums. They can be written as

$$\sum_{n_z, \text{even}} e^{-jk_{zm}|n_z|d_z} = -j \cot(k_{zm}d_z) \quad (\text{B.10})$$

$$\sum_{n_z, \text{odd}} e^{-jk_{zm}|n_z|d_z} = -j \csc(k_{zm}d_z) . \quad (\text{B.11})$$

Appendix C

Solutions for Current in ADL with Layer Composed of Lossy Patches

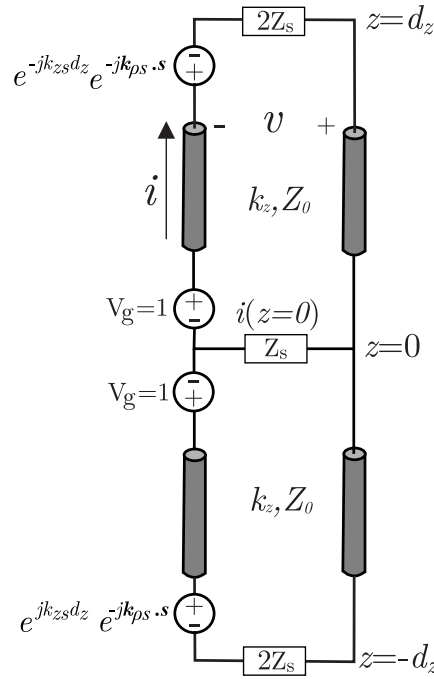


Figure C.1: Equivalent transmission line to the unit cell.

This appendix contains the solutions for the ADL composed by metal with finite conductivity described in chapter 3. The goal here is to find the definition the current on the layer $z = 0$ from the unit cell's transmission line depicted in C.1 in order to be able to reconstruct the Green's Function for the problem. The magnetic current densities are represented as voltage generators. In the layer $z = 0$, the voltage generator is equal to 1V. The generators placed in $z = d_z$ and $z = -d_z$ are assumed to be equal in amplitude and differ only in phase with generator at $z = 0$. The phase difference comes from a spatial displacement $e^{-jk_{ps} \cdot s}$ and a phase term $e^{\mp jk_z d_z}$. The vector $\mathbf{s} = s_x \hat{\mathbf{x}} + s_y \hat{\mathbf{y}}$ is indicating the shift and $\mathbf{k}_{ps} = k_{xs} \hat{\mathbf{x}} + k_{ys} \hat{\mathbf{y}}$ is an unknown wave vector describing the transverse propagation between adjacent layers.

To solve the transmission lines, superposition theorem is used. Due to the superposition theorem in circuit, it is possible to separate transmission line depicted in Fig. C.1 into two transmission lines (Fig. C.2) where each of them has two voltage generators. Furthermore, the transmission line marked as 1 in Fig. C.1 can be represented as Fig. C.3 where Z_{in} is the input impedance seen from $z = 0$. The input

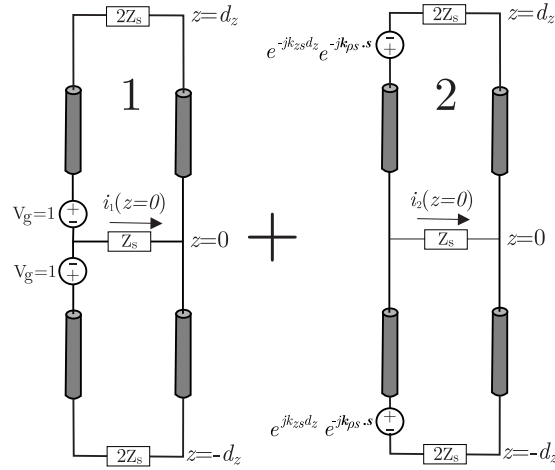


Figure C.2: Two transmission lines that are derived from 3.13.

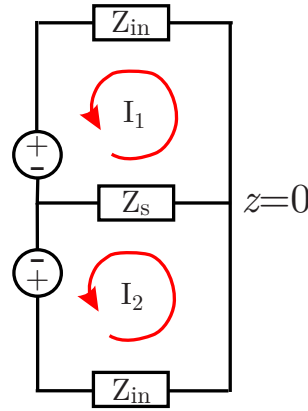


Figure C.3: Equivalent circuit for transmission line marked as 1 in figure 3.13.

impedance from the upper and lower region of this transmission line are the same because the structure is symmetric. The Z_{in} is given by:

$$Z_{in} = Z_0 \frac{2Z_s + jZ_0 \tan(k_z d_z)}{Z_0 + j2Z_s \tan(k_z d_z)} \quad (\text{C.1})$$

where Z_0 is the characteristic impedance of the transmission line, and k_z is propagation wavenumber describing propagation along z .

In order to find the current in the $z = 0$, the Kirchoff's loop rule is used

$$\begin{aligned} -1 + (I_1 - I_2)Z_s + I_1 Z_{in} &= 0 \\ 1 + (I_2 - I_1)Z_s + I_2 Z_{in} &= 0, \end{aligned} \quad (\text{C.2})$$

with knowledge that at $z = 0$: $I_{z=0} = I_1 - I_2$, equation (C.2) can be solved so that the current at $z = 0$ for the transmission line marked as 1 in Fig. C.1 can be written as

$$i_1(z = 0) = \frac{2}{2Z_s + Z_{in}}. \quad (\text{C.3})$$

Transmission line marked as 2 in Fig. C.1 can be solved by applying Thévenin's theorem. It is illustrated in Fig. C.4(a) that the transmission line is represented as a circuit similar to Fig. C.3 but with Thévenin's equivalent circuit impedance and voltage generator. Fig. C.4(b) shows the relation of the original circuit and its Thévenin's equivalent circuit voltage generator. In the other hand, the Thévenin's equivalent circuit impedance is no other than Z_{in} .

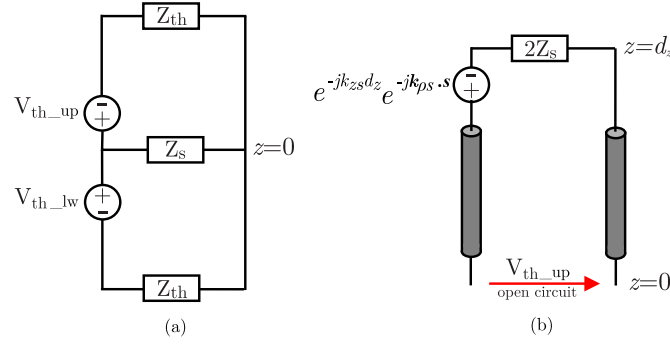


Figure C.4: (a) The equivalent Thévenin's circuit equal to transmission line marked as 2 in figure 3.13. (b) Definition of the Thévenin's equivalent circuit voltage generator for the problem.

Therefore, similar to the previous transmission line, the current that flows into the impedance Z_s at $z = 0$ depicted in Fig. C.4(a) is

$$i(z = 0) = \frac{V_{th_up} + V_{th_lw}}{2Z_s + Z_{in}}, \quad (C.4)$$

and the Thévenin's equivalent circuit voltage generator can be calculated from the total voltage and current waves on the line.

$$V(z) = V_0^+ e^{-jk_z z} + V_0^- e^{jk_z z} \quad \text{and} \quad I(z) = \frac{V_0^+}{Z_0} e^{-jk_z z} - \frac{V_0^-}{Z_0} e^{jk_z z} \quad (C.5)$$

where $V_0^+ e^{-jk_z z}$ is the wave generated from source at $z = 0$ propagating towards z^+ , and the vice versa for $V_0^- e^{jk_z z}$.

At $z = 0$, or the open circuit point, the voltage and current can be written as:

$$I(z = 0) = \frac{V_0^+}{Z_0} - \frac{V_0^-}{Z_0} = 0 \quad (\text{open circuit}) \quad \rightarrow V_0^+ = V_0^- \quad (C.6)$$

$$V(z = 0) = V_{th} = V_0^+ + V_0^- = 2V_0^+$$

which relates V_{th_up} to V_0^+ . The unknown V_0^+ is can be related to the the voltage at $z = 0$, seen by the generator at $z = d_z$, which is given by

$$V_{z=0} = V_0^+ e^{jk_z d_z} + V_0^- e^{-jk_z d_z} = V_0^+ (e^{jk_z d_z} + e^{-jk_z d_z}) = 2V_0^+ \cos(k_z d_z) \quad (C.7)$$

and the voltage divider can be applied to know the voltage drop at $z = 0$:

$$V_{z=0} = \frac{Z_{oc}}{Z_{oc} + 2Z_s} e^{-jk_{zs}d_z} e^{-jk_{ps} \cdot s} \quad (C.8)$$

where $Z_{oc} = -jZ_0 \cot(k_z d_z)$ is the impedance of the open circuit. Therefore, solving equation (C.7) to obtain V_0^+ and substitutes it to equation (C.6) will give:

$$V_{th_up} = -\frac{-jZ_0 \cot(k_z d_z)}{-jZ_0 \cot(k_z d_z) + 2Z_s} e^{-jk_{zs}d_z} e^{-jk_{ps} \cdot s} \sec(k_z d_z). \quad (C.9)$$

The V_{th_up} and V_{th_lw} in Fig. C.4(a) is equal in amplitude, but differs in the phase term. The phase terms represent the transverse propagation which is opposite to each other; i.e. $e^{-jk_z d_z}$ for the upper region, and $e^{jk_z d_z}$ for the lower region of the circuit. The phase term indicating the shift is the same, $e^{-jk_{ps} \cdot s}$, for

both. Thus, the transverse propagation terms vanishes, due to when the distance d_z is electrically small $e^{\pm jk_z d_z} \approx 1 \pm jk_z d_z$.

Substituting V_{th_up} and V_{th_lw} into equation (C.4) to find the current at $z = 0$ will result in:

$$i_2(z = 0) = -\frac{2}{2Z_s + Z_{in}} \frac{-jZ_0 \csc(k_z d_z)}{-jZ_0 \cot(k_z d_z) + 2Z_s} e^{-jk_{ps} \cdot s}. \quad (C.10)$$

Total current that flows at $z = 0$ at the original problem (figure C.1) can be seen as an addition of currents that are given by equation (C.3) and (C.10) which is

$$i_{tot}(z = 0) = \frac{2}{2Z_s + Z_{in}} - \frac{2}{2Z_s + Z_{in}} \frac{-jZ_0 \csc(k_z d_z)}{-jZ_0 \cot(k_z d_z) + 2Z_s} e^{-jk_{ps} \cdot s}. \quad (C.11)$$

It can be proved that equation (C.11) simplifies to:

$$i_{tot}(z = 0) = \frac{2S}{Z_0 + 2Z_s S}, \text{ where } S = -j \cot(k_z d_z) + j \csc(k_z d_z) e^{-jk_{ps} \cdot s}. \quad (C.12)$$

Proof of equation (3.22)

Starting from equation (3.21):

$$\begin{aligned} i_{tot}(z = 0) &= \frac{2}{2Z_s + Z_{in}} - \frac{2}{2Z_s + Z_{in}} \frac{-jZ_0 \csc(k_z d_z)}{-jZ_0 \cot(k_z d_z) + 2Z_s} e^{-jk_{ps} \cdot s} \\ &= \frac{2}{2Z_s + Z_{in}} \left(1 - \frac{-jZ_0 \csc(k_z d_z)}{-jZ_0 \cot(k_z d_z) + 2Z_s} e^{-jk_{ps} \cdot s} \right) \\ &= \frac{2}{2Z_s + Z_{in}} \left(\frac{-jZ_0 \cot(k_z d_z) + 2Z_s + jZ_0 \csc(k_z d_z) e^{-jk_{ps} \cdot s}}{-jZ_0 \cot(k_z d_z) + 2Z_s} \right) \\ &= \frac{2}{2Z_s + Z_{in}} \left(\frac{Z_0 (-j \cot(k_z d_z) + j \csc(k_z d_z) e^{-jk_{ps} \cdot s}) + 2Z_s}{-jZ_0 \cot(k_z d_z) + 2Z_s} \right) \end{aligned} \quad (C.13)$$

Defining S as $S = -j \cot(k_z d_z) + j \csc(k_z d_z) e^{-jk_{ps} \cdot s}$ and substituting expression of Z_{in} (equation (C.1)) into equation (C.13) give:

$$\begin{aligned} i_{tot}(z = 0) &= \frac{2}{2Z_s + Z_0 \frac{2Z_s + jZ_0 \tan(k_z d_z)}{Z_0 + j2Z_s \tan(k_z d_z)}} \left(\frac{Z_0 S + 2Z_s}{-jZ_0 \cot(k_z d_z) + 2Z_s} \right) \\ &= \frac{2(Z_0 S + 2Z_s)}{2Z_s (-jZ_0 \cot(k_z d_z) + 2Z_s) + Z_0 (-jZ_0 \cot(k_z d_z) + 2Z_s) \frac{2Z_s + jZ_0 \tan(k_z d_z)}{Z_0 + j2Z_s \tan(k_z d_z)}} \\ &= \frac{2(Z_0 S + 2Z_s)}{2Z_s (-jZ_0 \cot(k_z d_z) + 2Z_s) + Z_0 (-jZ_0 \cot(k_z d_z) + 2Z_s) \frac{2Z_s + jZ_0 \tan(k_z d_z)}{Z_0 + j2Z_s \tan(k_z d_z)}} \end{aligned} \quad (C.14)$$

where the denominator can be simplified as:

$$\begin{aligned}
 den &= 2Z_s(-jZ_0 \cot(k_z d_z) + 2Z_s) + Z_0(-jZ_0 \cot(k_z d_z) + 2Z_s) \frac{2Z_s + jZ_0 \tan(k_z d_z)}{Z_0 + j2Z_s \tan(k_z d_z)} \\
 &= 2Z_s(-jZ_0 \cot(k_z d_z) + 2Z_s) + Z_0 \frac{j \tan(k_z d_z)}{j \tan(k_z d_z)} (-jZ_0 \cot(k_z d_z) + 2Z_s) \frac{2Z_s + jZ_0 \tan(k_z d_z)}{Z_0 + j2Z_s \tan(k_z d_z)} \\
 &= 2Z_s(-jZ_0 \cot(k_z d_z) + 2Z_s) + Z_0 \frac{1}{j \tan(k_z d_z)} \cancel{(Z_0 + 2jZ_s \tan(k_z d_z))} \frac{2Z_s + jZ_0 \tan(k_z d_z)}{\cancel{Z_0 + j2Z_s \tan(k_z d_z)}} \\
 &= 2Z_s(-jZ_0 \cot(k_z d_z) + 2Z_s) + Z_0 \frac{2Z_s + jZ_0 \tan(k_z d_z)}{j \tan(k_z d_z)} \\
 &= 2Z_s(2Z_s - jZ_0 \cot(k_z d_z)) + Z_0(Z_0 - 2jZ_s \cot(k_z d_z)) \\
 &= 4Z_s^2 + Z_0^2 - 4j(Z_0 Z_s \cot(k_z d_z)) \\
 &= 4Z_s^2 + Z_0^2 + 2Z_0 Z_s (-2j \cot(k_z d_z)) \\
 &= 4Z_s^2 + Z_0^2 + 2Z_0 Z_s (-j \cot(k_z d_z) - j \cot(k_z d_z) + j \csc(k_z d_z) - j \csc(k_z d_z)) \\
 &\text{with } S = -j \cot(k_z d_z) + j \csc(k_z d_z) \text{ and } \frac{1}{S} = -j \cot(k_z d_z) - j \csc(k_z d_z), \\
 den &= 4Z_s^2 + Z_0^2 + 2Z_0 Z_s (S + \frac{1}{S}).
 \end{aligned} \tag{C.15}$$

to give:

$$\begin{aligned}
 i_{tot}(z=0) &= \frac{2(Z_0 S + 2Z_s)}{4Z_s^2 + Z_0^2 + 2Z_0 Z_s (S + \frac{1}{S})} \\
 &= \frac{2(Z_0 S + 2Z_s)}{\cancel{(2Z_s + Z_0 S)} (2Z_s + \frac{Z_0}{S})} \\
 i_{tot}(z=0) &= \frac{2S}{(Z_0 + 2Z_s S)}.
 \end{aligned} \tag{C.16}$$

List of Figures

1.1	Illustration of a car equipped with long-range and high-resolution radars in action. With the help of the radars, the car is able to distinguish cyclists on its way and perform braking when it is needed [2].	2
1.2	Projection of speed over year both for the fixed and mobile communications. Several points mark the standards and the corresponding operating frequency [4].	2
1.3	(a) A slot antenna in free space, (b) a dipole antenna in free space, and (c) the antennas in the presence of a metal ground plane.	3
1.4	A slot antenna on chip.	3
1.5	A slot antenna on chip in the presence of (a) high permittivity homogeneous superstrate and (b) ideal anisotropic superstrate.	3
1.6	Artificial dielectrics made of (a) metallic spheres, (b) cylinders, (c) strips.	4
1.7	Artificial dielectric composed of cascades of metal patches layers embedded in host medium.	5
1.8	Effective refractive index of ADL as a function of the angle of incidence and the polarization.	5
1.9	A slot antenna on chip (a) with presence of an ideal substrate on the top, (b) with ADL that mimics the ideal substrate on the top.	5
1.10	Side and top view of an ADL with (a) aligned layers (b) non-aligned (shifted) layers. . .	6
1.11	Enhancement factor, defined as the ratio between the square of effective refractive indexes with and without shift, versus shift. The ADL consists of 5 layer with $d_x = d_y = 0.0785\lambda_0$, $w_x = w_y = 0.01\lambda_0$, with λ_0 is wavelength at calculation frequency.	7
1.12	Electric field distribution for a plane wave propagating through the ADL slab for (a) aligned and (b) non-aligned layers. In the first case, the electric field is mainly concentrated in the gaps between coplanar patches. In the second case the field is also strong in the vertical gaps between contiguous layers, resulting in a higher capacitive loading. . . .	7
2.1	Single layer of infinitely periodic patches along xy plane with its geometrical parameters.	12
2.2	(a) Original problem which consists of a single layer of periodic square patches illuminated with generic plane wave illumination. (b) Applying equivalence theorem onto the gaps. (c) Filling the enclosed surface with perfect electrical conductor (PEC).	12
2.3	(a) Illustration of the uniform transverse distribution with anti-symmetric longitudinally, \mathbf{f}_3 (\mathbf{f}_4 is along y). (b) Illustration of the distribution at junction.	14
2.4	Equivalent circuit representation of the layer reactance of a single layer of patches. . . .	16

2.5	Amplitude and phase of the reflection and transmission coefficients of a plane wave incident on a single layer of square patches, comparing analytical solution presented in this part with CST simulation: (a) TE and TM, broadside incidence; (b) TE incidence $\theta = 60^\circ$, $\phi = 60^\circ$; (b) TM incidence $\theta = 60^\circ$, $\phi = 60^\circ$. The geometrical parameters are $d_x = d_y = 0.0785\lambda_0$, $w_x = w_y = 0.01\lambda_0$, with λ_0 being the wavelength at 5 GHz.	17
2.6	(a) Original problem which consists of a single layer of periodic square patches illuminated with generic plane wave illumination. (b) Applying equivalence theorem onto the gaps. (c) Filling the enclosed surface with the same material as the patches.	18
2.7	Equivalent z -transmission lines for the problem showing (a)TE and (b) TM modes for a magnetic source.	20
2.8	Equivalent circuit representation of the single layer of patches with finite conductivity.	21
2.9	Comparison between analytical solution and HFSS simulation of amplitude and phase of the reflection and transmission coefficients of a plane wave incident on a single layer of patches with finite conductivity ($\sigma = 1000S/m$): (a) TE, $\theta = 40^\circ$, $\phi = 0^\circ$; (b) TM, $\theta = 40^\circ$, $\phi = 0^\circ$; (c) TE, $\theta = 60^\circ$, $\phi = 0^\circ$; (d) TM, $\theta = 60^\circ$, $\phi = 0^\circ$. The geometrical parameters are $d_x = d_y = 0.095\lambda_0$, $w_x = w_y = 0.01\lambda_0$, with λ_0 being the wavelength at 300 GHz.	22
2.10	Comparing loss (in dB) calculated based on analytical solution and HFSS simulation. The plane wave incident on a single layer of patches with finite conductivity ($\sigma = 1000 S/m$) with angle of incidence: (a) $\theta = 40^\circ$, $\phi = 0^\circ$; (b) $\theta = 60^\circ$, $\phi = 0^\circ$. The geometrical parameters of layer of patches are $d_x = d_y = 0.095\lambda_0$, $w_x = w_y = 0.01\lambda_0$, with λ_0 being the wavelength at 300 GHz.	23
2.11	Illustration on single layer of periodic patches illuminated by (a) TE incidence (b) TM incidence. It is evident that the electric fields that are propagating in the slot generate electric current loops in the patches in TE incidence, while in TM incidence the patches does not support such current loop.	23
3.1	Definition of the geometrical parameters characteristic of the shifted ADLs: (a) cross section and (b) top view.	26
3.2	Aperture fields on three layers of an infinite cascade of ADLs.	26
3.3	(a) original problem and (b) equivalent problem with unknown magnetic current distributions.	27
3.4	Application of image theorem for (a) Region 1 and (b) Region 2, defined in Fig. 3.4.	27
3.5	Description of the CST models used to simulate a semi-infinite cascade of layers. A lossy ADL with the same geometrical parameters is implemented so that the transmitted wave experiences low reflection.	28
3.6	Normalized magnetic current distribution on the two orthogonal slot axes (red dashed line in the inset), comparing CST with our approximation in (3.4): TE incidence along (a) x -axis and (b) y -axis slots, and TM incidence along (c) x -axis slot and (d) y -axis slot. The dimensions of the ADLs are $d_x = d_y = 0.0785\lambda_0$, $w_x = w_y = 0.01\lambda_0$, $d_z = 0.012\lambda_0$, $s_x = s_y = 0.5d_x$, with λ_0 being the wavelength at the calculation frequency. All figures refer to plane-wave incidence at $\theta = 60^\circ$ and $\phi = 60^\circ$	29
3.7	Vector magnetic current density and electric field magnitude in correspondence of the junction, obtained with CST. The electric-field magnitude (proportional to the magnetic current) drops in the junction due to the widening of the magnetic current.	30
3.8	(a) Plane wave impinging on a cascade of four ADLs with alternate shifts and (b) equivalent circuits for TE and TM components.	32

3.9	Amplitude and phase of the reflection and transmission coefficients of a plane wave incident on a cascade of 5 layers: (a) TE, $\theta = 60^\circ$, $s_{x,y} = 0.25d_{x,y}$; (b) TM, $\theta = 60^\circ$, $s_{x,y} = 0.25d_{x,y}$; (c) TE, $\theta = 60^\circ$, $s_{x,y} = 0.5d_{x,y}$; (d) TM, $\theta = 60^\circ$, $s_{x,y} = 0.5d_{x,y}$. The geometrical parameters are $d_x = d_y = 0.0785\lambda_0$, $w_x = w_y = 0.01\lambda_0$, $d_z = 0.012\lambda_0$, with λ_0 being the wavelength at 5 GHz.	33
3.10	Convergence characteristics, defined as in (3.16), of the susceptance B_∞ as a function of the number of Floquet modes: (a) $d_z = 0.01\lambda_0$ and three values of $w_x = w_y$ are considered; (b) $w_x, w_y = 0.01\lambda_0$ and three values of d_z are considered. The other parameters are $d_x = d_y = 0.2\lambda_0$ and $s_x = s_y = 0.45d_x$	34
3.11	(a) original problem and (b) equivalent problem with unknown magnetic current distributions.	35
3.12	Equivalent representation of the ADLs' unit cell: (a) the lossless case, (b) the lossy case.	35
3.13	Equivalent transmission line to the unit cell and depiction of the superposition circuit theorem	36
3.14	Equivalent circuit for transmission line marked as 1 in figure 3.13.	36
3.15	(a) The equivalent Thévenin's circuit equal to transmission line marked as 2 in figure 3.13. (b) Definition of the Thévenin's equivalent circuit voltage generator for the problem.	37
3.16	Equivalent circuit representation of the ADL composed of 5 layers with finite conductivity for TE and TM component.	39
3.17	Comparing loss (in dB) calculated based on analytical solution and HFSS simulation. The plane wave incident on an ADL with finite conductivity ($\sigma = 1000$ S/m) with angle of incidence $\theta = 60^\circ$, $\phi = 0^\circ$. The geometrical parameters of layer of patches are $d_x = d_y = 0.095\lambda_0$, $w_x = w_y = 0.01\lambda_0$, $d_z = 0.02\lambda_0$, and shift (a) $s_x = s_y = 0$ (aligned); (b) $s_x = s_y = d_x/2$, with λ_0 being the wavelength at 300 GHz.	39
3.18	Comparison between analytical solution and HFSS simulation of amplitude and phase of the reflection and transmission coefficients of a plane wave incident on a single layer of patches with finite conductivity ($\sigma = 1000$ S/m), with angle of incidence $\theta = 60^\circ$, $\phi = 0^\circ$ (a) TE incidence $s_x = s_y = 0$ (aligned) (b) TM incidence $s_x = s_y = 0$ (aligned), (c) TE incidence $s_x = s_y = d_x/2$ (d) TM incidence $s_x = s_y = d_x/2$. The geometrical parameters are $d_x = d_y = 0.095\lambda_0$, $w_x = w_y = 0.01\lambda_0$, and $d_z = 0.02\lambda_0$, with λ_0 being the wavelength at 300 GHz.	40
3.19	(a) Scattering parameters magnitude and phase, and (b) losses in dB for a TE incidence impinging on a 5 layers aligned-ADL with finite conductivity ($\sigma = 10^6$ S/m) with angle of incidence $\theta = 60^\circ$, $\phi = 0^\circ$. The geometrical parameters of layer of patches are $d_x = d_y = 0.095\lambda_0$, $w_x = w_y = 0.01\lambda_0$, $d_z = 0.15\lambda_0$, with λ_0 being the wavelength at 300 GHz.	41
4.1	Illustration of an anisotropic slab (characterized by $\bar{\epsilon}$ and $\bar{\mu}$) illuminated by electromagnetic field coming from oblique incident angle θ_i	44
4.2	(a) Unit cell of an ADL composed of 5 non-aligned layers. The ADL is consisted of layers of perfectly conducting square patches with $d_x = d_y = 0.0785\lambda_0$, $d_z = 0.012\lambda_0$, $w_x = w_y = 0.01\lambda_0$, $s_x = s_y = 0.5d_x$, with λ_0 being the wavelength at the calculation frequency. The patches are embedded in material with $\epsilon_{host} = 1$. (b) An anisotropic slab with the same height and effective parameter as aforementioned ADL.	45
4.3	Scattering parameters comparison between ADL and its equivalent slab. (a) TE and (b) TM polarization of incidence plane wave arriving from oblique angle $\theta = 60^\circ$ and $\phi = 0^\circ$	45

4.4	Equivalent x - and y - components of the relative permittivity tensor and equivalent z -component of the relative permeability tensor, as a function of the shift. The ADL is composed of 5 perfectly conducting layers of patches embedded in a medium with $\epsilon_{r,\text{host}} = 1$, where: (a)-(b) $d_x = d_y = 0.0785\lambda_0$, $d_z = 0.012\lambda_0$, and different slot widths, (c)-(d) $w_x = w_y = 0.01\lambda_0$, $d_z = 0.012\lambda_0$, and different periodicity, (e)-(f) $d_x = d_y = 0.0785\lambda_0$, $w_x = w_y = 0.01\lambda_0$, and different inter-layer distance, with λ_0 being the wavelength at the calculation frequency.	47
4.5	Illustration upon the diamagnetism of ADLs. For TE incidence, the induced electric field distribution in the layer creates electric current loops on the metal patches. The loops are inducing magnetic field with the opposite sign of the incident magnetic field, h_i	48
4.6	Square of refraction index, evaluated from equation (4.3), over angle of incidence in ADL. The ADL is composed of 5 layers of PEC patches with $d_x = d_y = 0.0785\lambda_0$, $w_x = w_y = 0.01\lambda_0$, $d_z = 0.012\lambda_0$, and $s_x = s_y = 0.5d_x$ where λ_0 is the wavelength at the calculation frequency. The ADL is hosted in a material with $\epsilon_{r,\text{host}} = 1$	48
4.7	Angle in ADL over the angle of incidence. The ADL is hosted in free-space and is composed of 5 layers with $d_x = d_y = 0.0785\lambda_0$, $w_x = w_y = 0.01\lambda_0$, $d_z = 0.012\lambda_0$, and $s_x/d_x = s_y/d_y = 0.5$, where λ_0 is the wavelength at the calculation frequency at 300 GHz.	49
4.8	Square of refraction index over frequency. The ADL is composed of 5 layers of patches with $d_x = d_y = 0.2\lambda_0$, $w_x = w_y = 0.01\lambda_0$, and $s_x = s_y = 0.5d_x$ where λ_0 is the wavelength at the calculation frequency. The ADL is hosted in a material with $\epsilon = 1$	49
4.9	Square of index refraction (n^2) as function of angle incidence in ADL for TE and TM incidence. The plot has certain range that shows 5% tolerance in the (a) shift (b) inter-layer distance (c) periodicity (d) slot width (e) all geometrical parameters aforementioned. The ADL composed of 5 layers with $d_x = d_y = 0.0785\lambda_0$, $w_x = w_y = 0.01\lambda_0$, $d_z = 0.012\lambda_0$, and $s_x/d_x = s_y/d_y = 0.5$, where λ_0 is the wavelength at the calculation frequency at 300 GHz. The patches is hosted in the free-space.	50
4.10	Comparison between CST simulations of the real and equivalent ADL slabs, in terms of the amplitude and phase of the reflection and transmission coefficients of a plane wave incident on 5-layers-ADL with finite conductivity ($\sigma = 1000\text{S/m}$), with angle of incidence $\theta = 60^\circ$, $\phi = 0^\circ$ (a) TE incidence (b) TM incidence. The geometrical parameters are $d_x = d_y = 0.095\lambda_0$, $w_x = w_y = 0.01\lambda_0$, and $d_z = 0.02\lambda_0$, with λ_0 being the wavelength at 300 GHz.	51
4.11	(a) Equivalent x - and y - components of the complex relative permittivity tensor and (b) equivalent z -component of the complex relative permeability tensor, as a function of the shift. The ADL is composed of 5 layers embedded in a medium with $\epsilon_{r,\text{host}} = 1$, with $d_x = d_y = 0.0785\lambda_0$, $w_x = w_y = 0.01\lambda_0$, with λ_0 being the wavelength at the calculation frequency. Two different inter-layer distances are investigated. The patches have finite conductivity $\sigma = 1000\text{ S/m}$	51
4.12	(a) Tangent delta and (b) magnetic tangent delta over frequency. The ADL is composed of 5 layers embedded in a medium with $\epsilon_{r,\text{host}} = 1$, with $d_x = d_y = 0.0785\lambda_0$, $w_x = w_y = w = 0.01\lambda_0$, $s_x = s_y = 0.5d_x$ with λ_0 being the wavelength at the calculation frequency. Three different sizes of patches with finite conductivity $\sigma = 1000\text{ S/m}$ are investigated.	52
4.13	Snippet of the GUI developed to characterize ADLs.	52
A.1	Equivalent admittance of one layer of the ADLs embedded in an infinite cascade: (a) unit cell and (b) equivalent representation of the admittance matrix.	65

C.1	Equivalent transmission line to the unit cell.	69
C.2	Two transmission lines that are derived from 3.13.	70
C.3	Equivalent circuit for transmission line marked as 1 in figure 3.13.	70
C.4	(a) The equivalent Thévenin's circuit equal to transmission line marked as 2 in figure 3.13. (b) Definition of the Thévenin's equivalent circuit voltage generator for the problem.	71
